

PROBING THE
SUPERHYDROGENATION OF
CORONENE ON GRAPHITE

PHD THESIS

ANDERS WITTE SKOV
ALS07@PHYS.AU.DK

SUPERVISOR: LIV HORNEKÆR

SEPTEMBER 2016

DEPARTMENT OF PHYSICS AND ASTRONOMY
AARHUS UNIVERSITY

This thesis has been submitted to the Graduate School of Science and Technology at Aarhus University in order to fulfil the requirements for obtaining a PhD degree. The work presented has been performed under supervision of Associate Professor Liv Hornekær in the Surface Dynamics Laboratory group at The Department of Physics and Astronomy, Aarhus University.

Acknowledgements

A PhD study is not something you do on your own. A lot of people have helped me get through the last three years and without them I would not have been able to complete my studies.

First of all I would like to thank my supervisor Liv Hornekær for giving me the opportunity to do a PhD project in the Surface Dynamics Laboratory group and for her guidance, motivation and feedback during my time in the group.

I am thankful to all the people I have worked with in the group, both present and former. Thank you for good company and great discussion. A special thank should go to Andrew Cassidy for always taking the time to answering questions, discuss ideas and proofreading whatever I asked him to. Thank you to John David Thrower for introducing me to experimental physics, TPD and the Big Chamber. Thank you to Jakob Holm Jørgensen and Richard Balog for teaching me STM and for their company when working on the Createc chamber; and to Pernille Ahlmann Jensen and Frederik Doktor Simonsen for their company when working on the Big Chamber.

I am grateful for the good collaboration with Bjørk Hammer and his PhD student Mie Andersen.

A special thank should also be given to Andrew Cassidy, Pernille Ahlmann Jensen, Frederik Doktor Simonsen and Louise Lind Skov for meticulously proofreading this thesis.

Finally a big thank you to my family and friends for all their support during the last three years; especially to my wife Anne for her love and support and for her patience during stressful periods.

Anders Witte Skov, September 2016

Contents

List of Publications	iii
Abbreviations	v
1 Introduction	1
1.1 Motivation	2
1.2 Outline	4
2 Methods	5
2.1 Temperature programmed desorption	6
2.1.1 Adsorption and desorption	6
2.1.2 The Polanyi-Wigner equation	8
2.1.3 Data analysis	12
2.1.4 Experimental setup	14
2.2 Scanning tunnelling microscopy	16
2.2.1 Experimental setup	17
2.3 Density functional theory	18
3 Literature overview	21
3.1 Polycyclic aromatic hydrocarbons	22
3.1.1 PAHs on surfaces	24
3.2 Interaction between PAHs and atomic hydrogen	28
3.2.1 Neutrals	29
3.2.2 Ions	36
3.2.3 Summary	38
3.3 The interstellar medium	39
3.3.1 PAHs in the ISM	42
3.3.2 Molecular hydrogen formation	45

4	Thermal desorption measurements	49
4.1	Thermal desorption of coronene	50
4.2	Deuteration of coronene	54
4.3	Kinetic simulations of the deuteration of coronene	61
4.4	The coronene-graphite interaction during deuteration	67
4.5	Coronene deuteration through interaction with deuterated graphite	72
4.6	Conclusion	75
5	Scanning tunneling microscopy measurements	79
5.1	Pristine coronene on graphite	80
5.2	Hydrogenated coronene on graphite	88
5.3	Conclusion	93
6	Summary and Outlook	95
6.1	Summary	96
6.2	Outlook	98
7	Dansk resumé	101
7.1	Polyaromatiske kulbrinter	102
7.2	Eksperimentelle teknikker	103
7.3	Resultater	104
	Bibliography	107

List of Publications

- J. D. Thrower, E. E. Friis, **A. L. Skov**, L. Nilsson, M. Andersen, L. Ferrighi, B. Jørgensen, S. Baouche, R. Balog, B. Hammer and L. Hornekær. Interaction between Coronene and Graphite from Temperature Programmed Desorption and DFT-vdW Calculations: Importance of Entropic Effects and Insights into Graphite Interlayer Binding. *Journal of Physical Chemistry C*, 117:13520-13529, 2013.
- J. D. Thrower, E. E. Friis, **A. L. Skov**, B. Jørgensen and L. Hornekær. Hydrogenation of PAH molecules through interaction with hydrogenated carbonaceous grains. *Physical Chemistry Chemical Physics*, 16:3381-3387, 2014.
- **A. L. Skov**, J. D. Thrower and L. Hornekær. Polycyclic aromatic hydrocarbons - catalysts for molecular hydrogen formation. *Faraday Discussions*, 168:223-234, 2014.
- **A. W. Skov**, M. Andersen, J. D. Thrower, B. Jørgensen, B. Hammer and L. Hornekær. The Influence of Coronene Super-Hydrogenation on Coronene-Graphite Interaction. *Submitted to Journal of Chemical Physics*

Abbreviations

AFM - Atomic force microscope/microscopy
AIR - Aromatic infrared bands
B3LYP - Becke, three-parameter, Lee-Yang-Parr
DFT - Density functional theory
DHA - 9,10-dihydroanthracene
DOS - Density of states
ESQC - Elastic scattering quantum chemistry
GGA - General gradient approximation
GMC - Giant molecular cloud
HABS - Hydrogen atom beam source
HBC - Hexa-peri-hexabenzocoronene
HK - Habenschaden-Küppers
HOMO - Highest occupied molecular orbital
HOPG - Highly ordered pyrolytic graphite
IR - Infrared
ISM - Interstellar medium
LEED - Low energy electron diffraction
LDA - Local density approximation
LDOS - Local density of states
LHe - Liquid helium
LN2 - Liquid nitrogen
LUMO - Lowest unoccupied molecular orbital
ML - Monolayer
PAH - Polycyclic aromatic hydrocarbon
PBE - Perdew, Burke, Ernzerhof
PDR - Photondominated/Photodissociation region
PID - Proportional-integral-derivative
QMS - Quadropole mass spectrometer
RT - Room temperature

SDL - Surface Dynamics Laboratory

SDW - Static distortion waves

STM - Scanning tunneling microscope/microscopy

TDS - Thermal desorption spectroscopy

TPD - Temperature programmed desorption

UHV - Ultrahigh vacuum

UIR - Unidentified infrared bands

UV - Ultraviolet

Chapter 1

Introduction

The following chapter provides a short motivation for the work presented in this thesis, as well as an outline for the following chapters. A more thorough literature review is presented in chapter 3

1.1 Motivation

Hydrogen is the most abundant element in the universe and molecular hydrogen is by far the most abundant molecule in the interstellar medium (ISM), the region of a galaxy situated between stars [1]. Molecular hydrogen is of great importance in several chemical and physical processes [2]. It is essential in the cooling of molecular clouds, which eventually collapse to form stars. Molecular hydrogen is also essential in the formation of complex molecules, since it acts as a catalyst or reactant in several chemical reactions. Despite the efficient destruction of molecular hydrogen by UV photons in some parts of the ISM it is still observed in significant quantities [2]. The observed abundance of molecular hydrogen is not fully understood, since the known formation routes can not fully explain these abundances, given known rates of destruction. At temperatures below 20 K and above several hundreds K efficient formation routes have been identified through adsorption of atomic hydrogen on interstellar dust grains [3] [4]. However, at intermediate temperatures efficient formation routes have yet to be identified. In this temperature regime polycyclic aromatic hydrocarbons (PAHs) have been suggested as possible catalysts, since a correlation has been observed between molecular hydrogen formation rates and PAH emission in certain parts of the ISM [5].

Carbon is the fourth most abundant element in the universe and in the ISM 5 - 20 % of all carbon is thought to be locked up in PAHs [6] [7]. PAHs are a group of molecules consisting of three or more fused aromatic rings. On earth PAHs can be found in oil, coal, soot, etc.; and are also a by-product of incomplete combustion [8]. PAHs are also present in barbecued and smoked food [9] and are essential for some of the good taste. PAHs are known to have negative health effects and are in many cases found to be carcinogenic [10]. Research therefore continue on PAH combustion and destruction.

In the ISM PAHs can be detected through their infrared (IR) emission features and close inspection of these reveal that they typically have a size ranging from 50 - 150 carbon atoms [2]; exist as both neutrals, cations and anions [2]; and in certain regions of the ISM, they are thought to have additional hydrogen atoms attached, i.e. they are superhydrogenated [11] [12]. The PAHs are thought to be important in the heating of molecular clouds, for the ionization balance of clouds and in several chemical reactions, including the formation of molecular hydrogen, as previously mentioned.

The aim of my PhD project is to investigate the reactions between atomic

hydrogen and neutral PAHs using modern surface science techniques. This has been conducted in order to investigate the catalytic activity of PAHs in the formation of molecular hydrogen. The experiments carried out in this thesis have involved the PAH coronene ($C_{24}H_{12}$) deposited on a graphite surface. The coronene films have been exposed to atomic hydrogen or deuterium. The effects of hydrogenation/deuteration of the coronene films have been studied using temperature programmed desorption (TPD) and scanning tunnelling microscopy (STM), and have in several cases been compared to density functional theory (DFT) calculations.

1.2 Outline

This section will provide an overview of the structure of this thesis and a short introduction to each chapter. The structure is as follows:

- Chapter 2 gives a theoretical introduction to the two primary experimental techniques used in this thesis; TPD (section 2.1) and STM (section 2.2). The chapter includes a short section about analysis of TPD spectra. The chapter also includes a short introduction to DFT calculations (section 2.3) which have been used as comparison for several of the experiments presented.
- Chapter 3 introduces PAHs and will give a context to the work presented in chapters 4 and 5, by discussing previous work relevant to the subject. This includes PAHs in general (section 3.1), PAHs and their interaction with atomic hydrogen (section 3.2) and a short introduction to the ISM (section 3.3).
- Chapter 4 is the main results chapter of this thesis and will present some of the results obtained using TPD during my PhD. The chapter begins by discussing experiments on the desorption of pristine coronene from graphite and the desorption kinetics involved (section 4.1). The subsequent sections are dedicated to the deuteration of coronene on graphite and the effects on the molecular mass distribution (section 4.2), the reaction addition and abstraction cross-sections (section 4.3), and the change in desorption kinetics during deuteration (section 4.4). The last section will discuss experiments on the deuteration of coronene through interaction with deuterated graphite (section 4.4).
- Chapter 5 will present some of the results obtained using STM during my PhD. This includes STM measurements on pristine coronene on graphite and STM measurements of hydrogenated coronene on graphite.
- Chapter 6 gives a summary of all the results presented in the thesis and discusses future experiments. This chapter also works as an abstract for the whole thesis.

Chapter 2

Methods

This chapter will give a short introduction to temperature programmed desorption (TPD) and scanning tunneling microscopy (STM), the two primary experimental techniques used for the work presented in this thesis. All experiments were carried out under ultrahigh vacuum (UHV) conditions. The chapter also includes a very short introduction to density functional theory (DFT) calculations, although I have not been directly involved in executing these calculations.

2.1 Temperature programmed desorption

TPD, also known as thermal desorption spectroscopy (TDS), describes the process where a sample is heated, while the molecules/atoms desorbing from the sample are probed. By controlling the increase in temperature this can give information about the adsorption/desorption kinetics and thermodynamics. In the experiments carried out in this work the desorbing molecules have been detected using a quadrupole mass spectrometer (QMS), providing information about the molecular species desorbing from the surface. TPD is the primary technique used in my research, therefore a more thorough description of TPD is presented.

2.1.1 Adsorption and desorption

In order to understand TPD it is vital to understand the adsorption and desorption processes. Adsorption generally describes a process whereby a molecule forms a bond with the surface of another material. Adsorption is generally divided into two categories depending on bond type, physisorption and chemisorption.

In physisorption the bond between the adsorbate and the surface is due to the van der Waals interaction, where by a dipole in the adsorbate interacts with the solid. This means that the physisorption state is a barrier-less adsorption state, as illustrated in the energy diagram in figure 2.1(a). Consequently all atoms and molecules will be able to physisorb. The binding energy or adsorption energy, E_{ad} , of the physisorption state is, however, generally weak (50 - 500 meV/atom [13]) and therefore physisorption often only occurs at low temperature. In some cases the physisorption state is just a precursor state to the chemisorption state.

In the chemisorption state the adsorbate forms a chemical bond with the surface i.e. a covalent, ionic or metallic bond. Hence there is an overlap between the electronic orbital of the adsorbate and the surface. This generally leads to a lot larger adsorption energies (1 - 10 eV/atom [13]) than for physisorption. Sometimes it is favourable for the adsorbate to dissociate upon adsorption and adsorb the fragments. This is known as dissociative adsorption. In many cases there will be an activation barrier or heat of adsorption, H_{ad} , for the adsorbate to adsorb on the surface, as illustrated in the example in figure 2.1(b).

Desorption, on the other hand, describes the process where the adsorbate

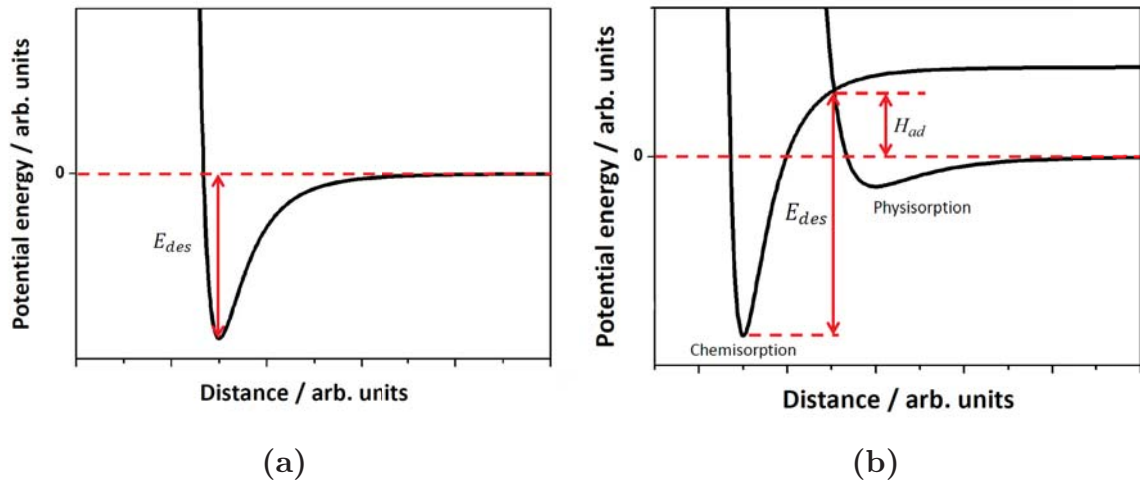


Figure 2.1: Illustrations of energy diagrams of the adsorption potentials for (a) physisorption and (b) chemisorption. The desorption energy (E_{des}) and the heat of adsorption (H_{ad}) are labelled in the illustrations. Modified from [14]

leaves the surface. This is an activated process, that requires the adsorbate to gain energy. This energy is known as the desorption energy, E_{des} , and can be visualized as the energy needed to get out of the adsorption well, or:

$$E_{des} = E_{ad} + H_{ad} \quad (2.1)$$

The desorption process can be activated by increasing the temperature of the sample or stimulated by electrons or light. In some cases the adsorbate will react to form larger molecules during the desorption process. This is known as associative desorption.

An important parameter when looking at adsorption film growth is the coverage of adsorbates. The absolute coverage of a surface is the number of adsorbates on the surface. This is often very difficult to determine, so instead the relative coverage, θ , of the surface is often used. θ is defined as the ratio between the number of occupied sites on the surface to the total number of available sites on the surface, hence for a complete monolayer $\theta = 1$. For adsorbate coverages close to a complete monolayer (ML), as well as for possible multilayers, interaction between adsorbates starts to affect the growth of the layer. The formation of mono- and multilayers depend on the adsorbate-adsorbate interaction, as well as the adsorbate-surface interaction. The strength of these interactions provides three different models for the growth mode of the adsorbates:

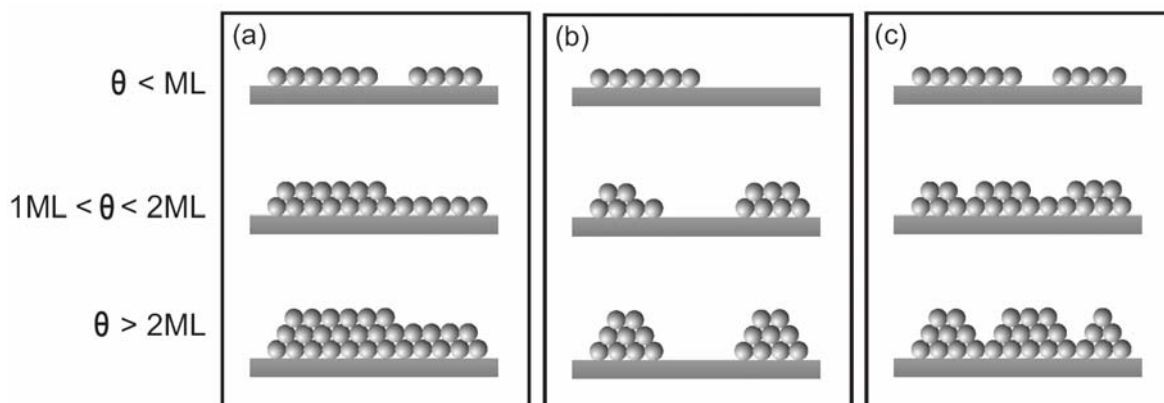


Figure 2.2: Illustration of the three growth modes for adsorption: (a) Frank-van der Merve growth; (b) Vollmer-Weber growth; and (c) Stranski-Krastarnov growth [16].

- (a) Frank-van der Merve growth occurs when the adsorbate-surface interactions is stronger than the interaction between the adsorbates. This results in the formation of a full layer before the above layer starts to form. Frank-van der Merve growth is also called layer-by-layer growth. Frank-van der Merve growth is illustrated in figure 2.2(a).
- (b) Vollmer-Weber growth occurs when the interaction between the adsorbates is stronger than the adsorbate-surface interaction. This results in island formation, therefore, Volmer-Weber growth is also called island growth. Volmer-Weber growth is illustrated in figure 2.2(b).
- (c) Stranski-Krastarnov growth is the intermediate case. After the formation of one or several complete monolayers, island formation starts to occur. The growth is not only dependent on the interaction between the adsorbates and the adsorbate-surface interaction, but can also be affected by lattice mismatch between the adsorbates and the substrate or the orientations of the overlayers with respect to the substrate [15]. Stranski-Krastarnov growth is illustrated in figure 2.2(c) and it is also known as layer-plus-island growth.

2.1.2 The Polanyi-Wigner equation

A thermally induced desorption process, like during a TPD measurement, can be described with a rate equation known as the Polanyi-Wigner equation,

where the rate of desorption, r_{des} , is given as:

$$r_{des} = -\frac{d\theta}{dt} = \nu\theta^n \exp\left(\frac{-E_{des}}{k_B T}\right) \quad (2.2)$$

where ν is a pre-exponential factor, n is the desorption order, k_B is the Boltzmann constant and T is the temperature of the surface. In TPD experiments the temperature is usually increased linearly, meaning that the following substitution can be made:

$$\frac{d\theta}{dt} = \frac{d\theta}{dT} \cdot \frac{dT}{dt} = \frac{d\theta}{dT}\beta \quad (2.3)$$

where β is the linear temperature ramp rate. Inserting this into equations 2.2 yields:

$$r_{des} = -\frac{d\theta}{dT} = \frac{\nu}{\beta}\theta^n \exp\left(\frac{-E_{des}}{k_B T}\right) \quad (2.4)$$

Since linear ramp rates have been used in all TPD experiments presented in this thesis, it is this modified Polanyi-Wigner equation that will be used here. An important assumption when using the Polanyi-Wigner equation for data analysis, is that the monitored desorption signal is proportional to the rate of desorption. Hence the pumping speed of the UHV chamber has to be constant and sufficiently high to prevent significant re-adsorption of desorbed atoms/molecules onto the sample.

In typical TPD experiments the coverage for a specific TPD curve is determined by comparing the integrated area under the TPD curve, with the area under a curve with a known θ , for instance for a complete monolayer.

Generally n can be related to the number of steps involved in the desorption reaction. First-order desorption is normally associated with monolayer systems, where the adsorbed molecules/atoms can leave the surface individually. This means that the desorption rate is only dependent on the concentration of the adsorbate itself and not dependent on the concentration of other adsorbates. Second-order desorption is also associated with monolayers, but where the adsorbed molecules/atoms have to combine to desorb. Therefore the desorption rate is dependent on the concentration squared. For multilayers zero-order desorption is usually observed, since the influence from the surface is gradually screened out, until the bonding almost resembles that in a condensed solid of the pure adsorbate and the desorption rate is therefore completely independent of coverage. In some cases n can

be of fractional order, if the Polanyi-Wigner equation is used on a systems for which it is not defined. This is, for instance, true for desorption from island edges, which is usually associated with half order kinetics [17].

The desorption order has a large effect on the shape of the TPD curve. This can be seen by looking at the Polanyi-Wigner equation at the desorption peak maximum, T_p . Since this is a maximum:

$$\frac{d^2\theta}{dT^2} = 0 \quad (2.5)$$

So by differentiating equation 2.4 and setting the resulting expression equal to zero, one obtains:

$$\frac{E_{des}}{k_b T_p^2} = \frac{\nu}{\beta} n \theta^{n-1} \exp\left(\frac{-E_{des}}{k_B T_p}\right) \quad (2.6)$$

From this equation it is clear that T_p is independent of coverage for first-order kinetics, while T_p decreases with coverage for second-order kinetics. These and other characteristics can be observed in figure 2.3 (a) and (b) where several first and second order TPDs have been simulated. In figure 2.3 (c) a set of zero-order TPDs have been simulated. For zero-order all of the TPDs have a common onset independent of coverage and T_p increases with θ . This can also be seen from the Polanyi-Wigner equation, where r_{des} is independent of θ for zero-order desorption and r_{des} increases exponentially with temperature until all multilayers have been desorbed.

The pre-exponential factor is generally assumed to be of the same order of magnitude as the molecular vibrational frequency, and is often taken to be 10^{13} s^{-1} . This assumption, however, only applies to small molecules. For bigger molecules ν is typically larger than 10^{13} s^{-1} [18]. By applying transition state theory to the Polanyi-Wigner equation it can be shown that ν is related to the change in entropy during the desorption process, ΔS^\ddagger , as [19]:

$$\nu = \frac{k_B T}{h} \frac{Q^\ddagger}{Q} = \frac{k_B T}{h} \exp\left(\frac{\Delta S^\ddagger}{R}\right) \quad (2.7)$$

where R is the gas constant. Q and Q^\ddagger are the partition functions for the adsorbed and transition state respectively. This means that through different estimates of the entropy of the adsorbed state, ν can be calculated. ν can vary both with temperature and coverage, but is often assumed to be constant relative to both.

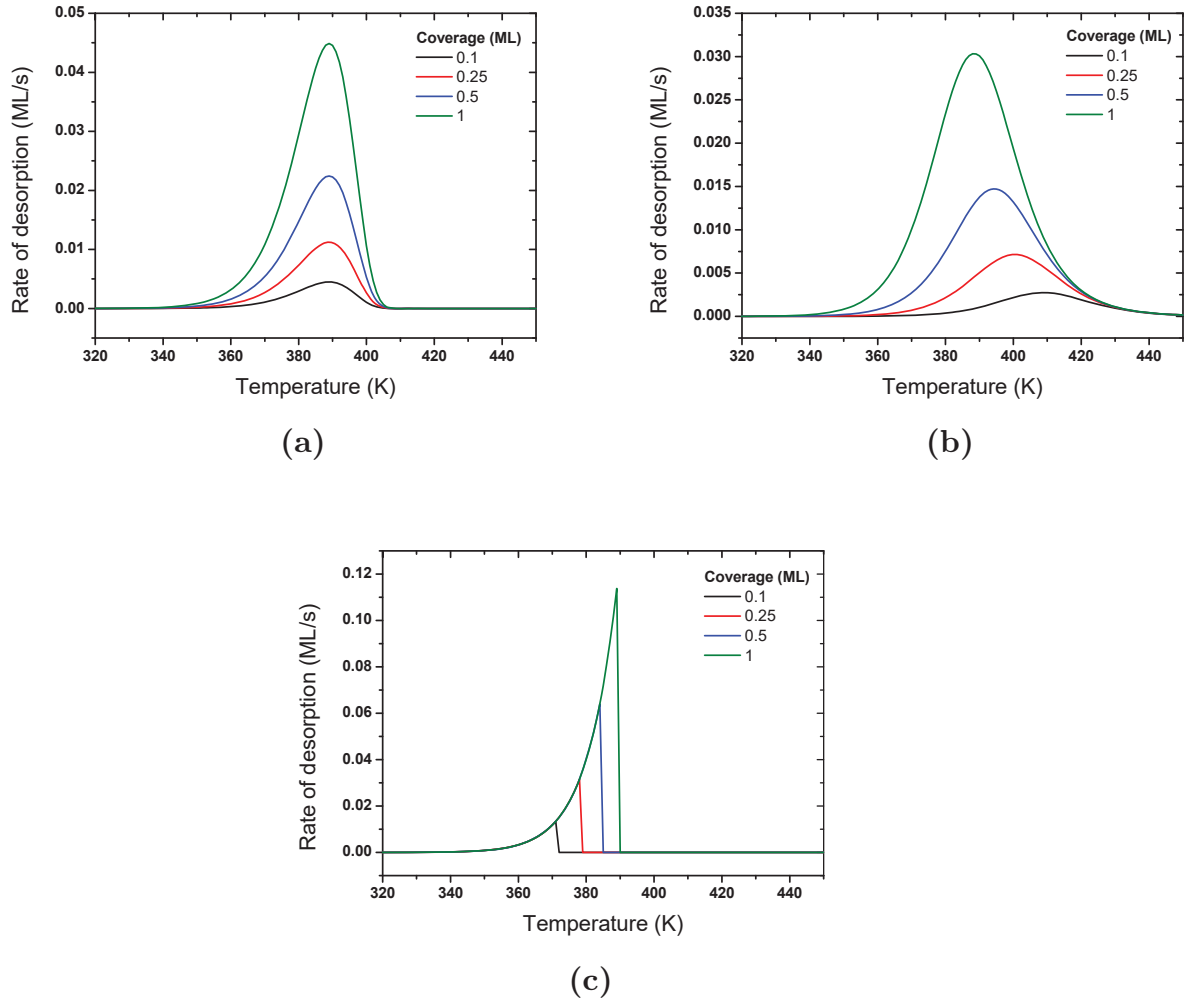


Figure 2.3: TPD simulations: (a) First-order desorption. (b) Second-order desorption. (c) Zero-order desorption. For all of the simulations the following parameters were used: $E_{des} = 1.48$ eV; $\nu = 1.7 \cdot 10^{18}$ s $^{-1}$ and $\beta = 1$ K s $^{-1}$

2.1.3 Data analysis

A vast range of methods exist for analysing TPD spectra and extracting kinetic information on the desorption from these. Several reviews have been published on this subject [20] [21] [22]. A few analysis methods will be discussed in this section. Most of the analysis methods rely on a set of TPD spectra measured for different coverages in order to determine E_{des} and ν . However if the desorption follows first-order kinetics and ν is known E_{des} can be determined directly from T_p , since this is independent of θ . This can be achieved using the Redhead equation [23], given as:

$$E_{des} = k_b T_p \ln \left[\left(\frac{\nu T_p}{\beta} \right) - 3.46 \right] \quad (2.8)$$

A more comprehensive analysis method is the Falconer-Madix analysis [24]. The Falconer-Madix analysis method uses a series of TPD spectra with different initial coverages. For each spectrum the coverage is determined as a function of temperature using this method:

$$\theta(T) = 1 - \int_0^T r_{des}(T) dT \quad (2.9)$$

$\theta(T)$ and $r_{des}(T)$ can now be rearranged into isothermal data sets for a specific temperature, T . Equation 2.4 is rewritten as:

$$\ln(r_{des}) = \ln \left(\frac{\nu}{\beta} \right) + n \cdot \ln(\theta) - \frac{E_{des}}{k_B T} \quad (2.10)$$

By plotting $\ln(r_{des})$ as a function of θ , for each isothermal data set, equation 2.10 shows that a linear fit will yield n as the slope, while the intercept will be

$$intercept = \ln \left(\frac{\nu}{\beta} \right) - \frac{E_{des}}{k_B T} \quad (2.11)$$

The intercept can now be plotted for each isothermal data set, as a function of $1/T$ and a linear fit will give $-E_{des}/k_B$ as the slope and $\ln(\nu/\beta)$ as the intercept. Hence this method can be used to determine both n , E_{des} and ν .

The Falconer-Madix analysis assumes that both ν and E_{des} are independent of θ . If this is not the case equation 2.10 is no longer valid and should be replaced with [25]:

$$\frac{d \ln(r_{des}/\theta^n)}{d(1/T)} = \frac{-E_{des}(\theta)}{k_b} + \frac{d\theta}{d(1/T)} \times \left[\frac{\partial \ln(\nu(\theta)/\beta)}{\partial \theta} - \frac{1}{k_b T} \left(\frac{\partial E_{des}(\theta)}{\partial \theta} \right) \right]_T \quad (2.12)$$

It is not possible to evaluate the second order terms of this equation, hence this is only useful when the second order terms can be ignored and equation 2.12 reduces to 2.10. This is possible in three cases. If E_{des} and ν are independent of θ the second order terms disappear and the Falconer-Madix analysis can be used. If $d\theta/d(1/T)$ is zero or vanishingly small the equation reduces to that used in the Habenschaden-Küppers (HK) analysis method and the complete analysis method which are described later. The second order terms also disappear if $1/k_B T [\partial E_{des}(\theta)/\partial \theta] = \partial \ln \nu(\theta)/\partial \theta$. This can, however, not be predicted.

In the HK or leading edge analysis method [26] only a small temperature interval at the low T, high θ part of the desorption peak is analysed, i.e. the leading edge. If the interval is small enough this will reduce to $d\theta/d(1/T) \sim 0$. The right side of equation 2.10 can now be plotted against $1/T$. This can be fitted with a linear fit, with $-E_{des}(\theta)/k_B$ as the slope and $\ln(\nu(\theta)/\beta)$ as the intercept. The HK analysis can be used on different temperature intervals on the leading edge, and conveys information on the coverage dependence of E_{des} and ν .

The complete analysis method [25] uses a family of TPD curves. For each spectrum a fixed coverage θ_i is found and $r_{des}(\theta_i)$ and $T(\theta_i)$ are identified. These values are rearranged into coverage constant data sets. For each data set the coverage is constant, so $d\theta/d(1/T) = 0$, reducing equation 2.12 to:

$$\ln \left(\frac{r_{des}}{\theta_i^n} \right) = \ln \left(\frac{\nu(\theta_i)}{\beta} \right) - \frac{E_{des}(\theta_i)}{k_b T} \quad (2.13)$$

If the desorption order is known, the right side of equation 2.13 can be plotted relative to $1/T$. Fitting this with a linear function will yield $-E_{des}(\theta_i)/k_B$ as the slope and $\nu(\theta_i)$ as the intercept. This can be repeated over the whole range of coverages, yielding $E_{des}(\theta)$ and $\nu(\theta)$.

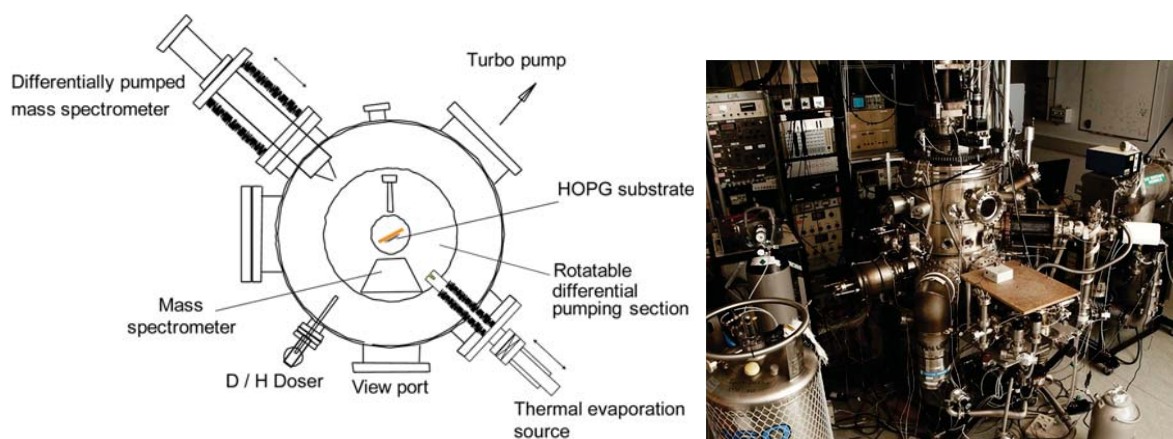


Figure 2.4: A schematic and a picture of the Big Chamber. This chamber has been used for all the TPD experiments presented in this thesis.

If any of these methods are used outside their range of validity or for poor quality data it can result in large errors, due to the so-called compensation effect. If the assumption that $d\theta/d(1/T) \sim 0$ is false the second order sum is forced to be zero. This means that $E_{des}(\theta)$ and $\nu(\theta)$ will vary in concert to keep $\nu \exp(-E_{des}/k_B T)$ constant, in other words compensating each other. The result is that a lot of different sets of E_{des} and ν can give a good fit to the data, which can result in incorrect values for E_{des} and ν .

2.1.4 Experimental setup

All the TPD experiments presented in this thesis were performed in an ultrahigh vacuum (UHV) chamber known as the Big Chamber. The chamber has a base pressure of $<10^{-10}$ mbar and is located in the Surface Dynamics Laboratory at the Department of Physics and Astronomy, at Aarhus University. An illustration and a picture of the chamber is shown in figure 2.4. Samples of interest can be placed in a Ta sample holder mounted in a watercooled copper block. The sample can be heated through electron bombardment of the backside of the sample holder. Electrons are emitted from a W filament and the sample holder is biased with a positive voltage of 500 - 1000 V relative to the filament in order to heat the sample as high as 1300 K. In order to measure the temperature of the sample, a C-type thermocouple is squeezed between the front side of the sample and the sample holder. The temperature of the sample is controlled with a model 340 LakeShore PID temperature controller, which allows for accurate control of the heat-



Figure 2.5: One of the quartz nozzles designed to cool the atomic H/D beam. The nozzle shown in this picture is estimated to cool the D beam to ~ 1000 K

ing rate. Deposition of molecular films can be achieved using a home-built Knudsen cell evaporation source. The sample can be exposed to an atomic hydrogen/deuterium, H/D, beam produced by dissociating H_2 (AGA, 6.0) or D_2 (Air Liquide, $>99.9\%$) with a hot capillary source similar to the one described by Tschersich *et al.* [27] [28] [29]. The source is operated at 2300 K giving 2300 K H/D atoms. In order to reduce the temperature of the H/D beam, bent quartz tubes can be attached to the front of the source cooling the H/D atoms through collisions. A picture of one of these tubes is shown in figure 2.5. By estimating the average amount of collisions and assuming elastic collisions between the D-atoms and SiO_2 , the beam temperature was estimated. For the nozzle shown in figure 2.5 the beam temperature was found to be ~ 1000 K. The flux of the hydrogen source can be calibrated through TPD measurements of D chemisorbed on Si(100) [30][31].

The chamber is equipped with two QMSs: a rotatable and differentially pumped Extrel CMS LLC with a cross ionization source and a mass range from 1 - 500 amu; and a differentially pumped Pfeiffer Vacuum Prisma with a mass range of 1 - 200 amu. The Pfeiffer QMS is mounted on an extendable arm fitted with a Feulener cap [32] which can be brought within 1 mm of the sample surface, giving high sensitivity.

The chamber is also equipped with a sputter ion gun, low energy electron diffraction (LEED) optics and auger electron spectroscopy optics, which were used for Si(100) sample preparation.

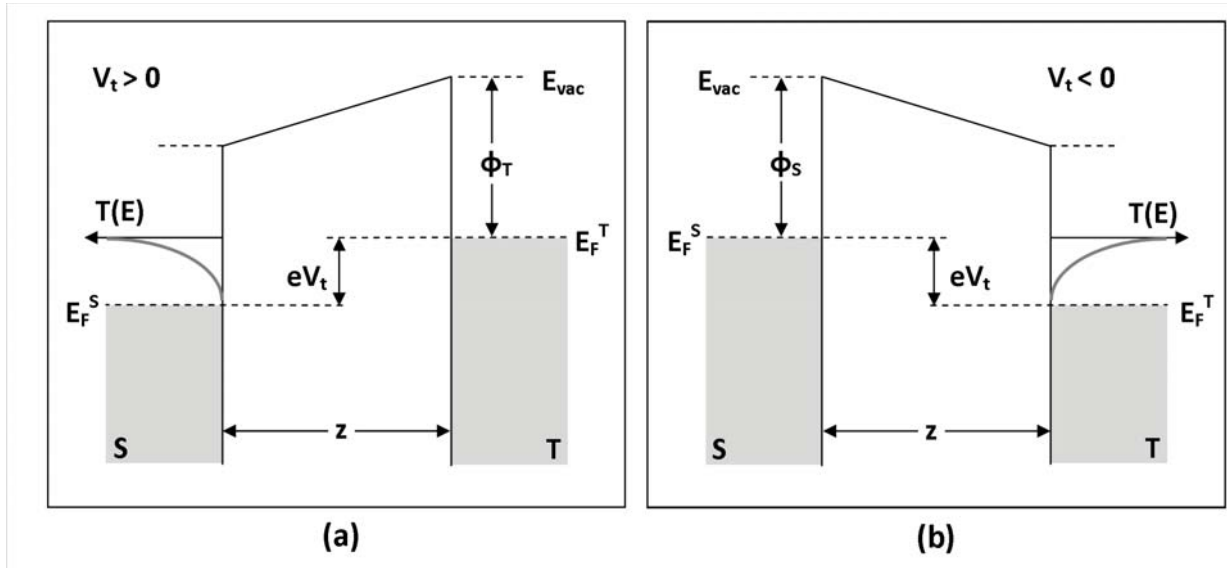


Figure 2.6: Band diagrams for (a) positive and (b) negative bias voltage. T corresponds to the tip and S to the surface.

2.2 Scanning tunnelling microscopy

The STM was developed in the start of the 1980s by Heinrich Rohrer and Gerhard Binnig [33] [34] [35] at IBM. An achievement that was rewarded with the Nobel prize in 1986. STM uses quantum mechanical tunnelling to provide three-dimensional images of surfaces at atomic scale resolution. When placing a metal tip at a distance, z , of a few Å from a conducting surface, the wave function of the tip will overlap with that of the surface. Electrons can then flow from the tip to the surface or vice versa and a rapid charge transfer takes place between them until equilibrium is achieved and the Fermi levels are aligned. By applying a voltage, V_t , between tip and sample the Fermi levels are shifted and electrons will flow from the filled states in the tip to the empty state of the sample or vice versa depending on the polarity of V_t . This results in a measurable tunnel current, I_t . An illustration of how the Fermi levels shift is shown in figure 2.6. In figure 2.6 T corresponds to the band diagram of the tip and S to that of the surface, E_F^T and E_F^S are then the respective Fermi energy levels, ϕ_T and ϕ_S are the respective work functions, and $T(E)$ is the transmission probability. The illustration shows how the energy levels are shifted eV_t compared to each other when a voltage is applied resulting in $|T(E)| > 0$.

The tunneling current can be approximated at low temperatures and low

voltages using the Wentzel-Kramers-Brillouin (WKB) approximation [36]:

$$I_t = \int_0^{eV_t} \rho_T(E) \rho_S(E - eV_t) T(E, eV_t) dE \quad (2.14)$$

where ρ_S and ρ_T are the local density of states (LDOS) at the energy E and $T(E, eV_t)$ is the tunneling transmission probability, given by:

$$T(E, eV_t) = \exp\left(-\frac{2z\sqrt{2m}}{\hbar}\right) \sqrt{\frac{\phi_T + \phi_S}{2} + \frac{eV_t}{2} - E} \quad (2.15)$$

where z is distance between tip and sample, m is the mass of the electron and ϕ_T and ϕ_S are the work functions of the tip and sample respectively. At low temperatures and low voltages this will yield:

$$I_t = \rho_T \rho_S V_t \exp\left(-2\sqrt{\frac{m(\phi_T + \phi_S)}{\hbar^2 z}}\right) \quad (2.16)$$

Or by substituting the attenuation constant, κ , we can write [37]:

$$I_t \propto \exp(-2\kappa/z) \quad \text{where : } \kappa = \frac{\sqrt{2m(\phi_T + \phi_S)}}{\hbar} \quad (2.17)$$

This illustrates the strong distance dependence for the tunnelling current which provides the high in-plane resolution of STM. κ is approximately 1 \AA^{-1} for typical work functions ($\phi_T + \phi_S \approx 4 \text{ eV}$).

It is important to keep in mind that the STM images reflect the LDOS of the surface at the tip position. On metal surfaces this generally coincides with the topography of the surface, but for semiconductors or surfaces with directional bonding, like graphite, the STM images in general reflect a convolution of the topography and the electronic states. If molecules are adsorbed on the surface, a convolution of the topography, the electronic states at the surface and the lowest unoccupied molecular orbitals (LUMO) or the highest occupied molecular orbitals (HOMO) is observed for positive or negative bias respectively.

2.2.1 Experimental setup

All the STM measurements presented in this thesis were carried out on a commercial Createc LT-STM setup located in the Interdisciplinary Nanoscience Center at Aarhus University. A picture of the chamber is shown in figure 2.7.

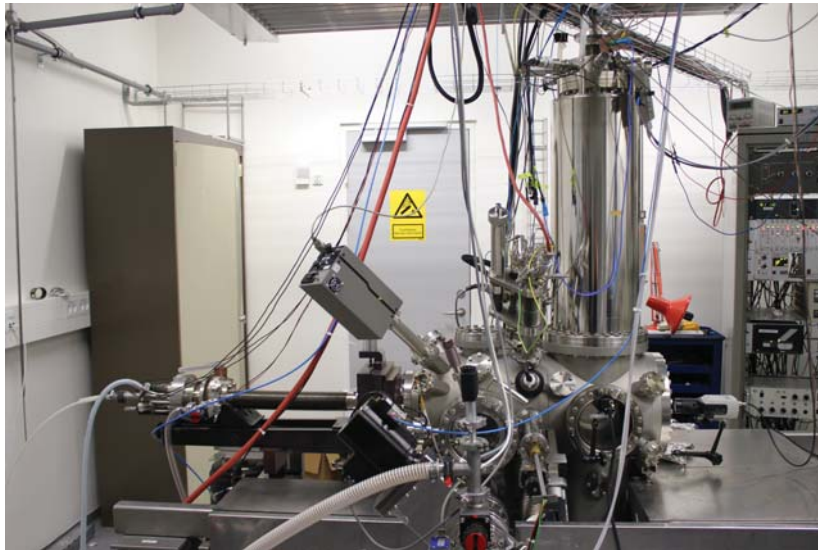


Figure 2.7: The Createc LT-STM chamber used for all STM measurements presented in this thesis

The chamber is divided into two separate compartments, an STM chamber with a base pressure of $<10^{-10}$ mbar and a preparation chamber with a base pressure of $<10^{-9}$ mbar. The STM chamber is equipped with a Besocke Beetle type STM [38] and atomic force microscope (AFM) scanner head, placed in a liquid bath cryostat. The STM can be cooled with either liquid nitrogen (LN2) to 77 K or with liquid helium (LHe) to ~ 5 K. The preparation chamber contains a hydrogen atom beam source (HABS) from MBE Komponenten [27] [28] [29], similar to the one used for the TPD measurements on the Big Chamber. Quartz tubes can also be attached to the HABS to cool the H-atoms. The chamber is also equipped with a Knudsen cell evaporation source, sputter ion gun, LEED optics and a QMS for rest gas analysis.

2.3 Density functional theory

Density functional theory (DFT) is a computational quantum mechanical method for solving the N-body Schrödinger equation. DFT is based on the Hohenberg-Kohn theorems [39]. The basis behind DFT is to substitute the many-electron wave function, which contains $3N$ variables, with the functional of electron density, $n(\mathbf{r})$, which contains only 3 variables. This implies that the energy of the system can be described as:

$$E[n(\mathbf{r}), v_{ext}(\mathbf{r})] = T[n(\mathbf{r})] + V_{ee}[n(\mathbf{r})] + \int v_{ext}(\mathbf{r})n(\mathbf{r})d\mathbf{r} \quad (2.18)$$

where $T[n(\mathbf{r})]$ is the kinetic energy, $V_{ee}[n(\mathbf{r})]$ is the electron-electron interaction and the integral is the energy associated with the external potential, $v_{ext}(\mathbf{r})$. This is known as the Hohenberg-Kohn energy functional. Solving this equation, however, is not straight forward. In the Kohn-Sham approach [40] the electrons in general are viewed as non-interacting in an effective potential, so the energy of the system can be described by:

$$E[n(\mathbf{r}), v_{ext}(\mathbf{r})] = T_0[n] + V_H[n] + \int v_{ext}(\mathbf{r})n(\mathbf{r})d\mathbf{r} + E_{xc}[n] \quad (2.19)$$

where $T_0[n]$ is the kinetic energy of the system with non-interacting electrons, the effective potential is given by the integral and $V_H[n]$ describing the part of the electron-electron interaction given by classical Coulomb interaction and $E_{xc}[n]$ is the exchange-correlation functional defined by:

$$E_{xc}[n] = T[n] - T_0[n] + V_{ee}[n] - V_H[n] \quad (2.20)$$

The remaining problem then is to find a suitable functional for the exchange-correlation. Several approximations to the exchange-correlation have been provided, with the local density approximation (LDA) [41] being one of the simplest. In LDA the exchange-correlation is assumed to be dependent on the electron density at the point where it is being evaluated. An improvement to the LDA functional can be made using one of the general gradient approximation (GGA) functionals. Here the functional also takes the gradient of the electron density into account. The most common GGA functionals are the Becke, three-parameter, Lee-Yang-Parr (B3LYP) functional [42] and the Perdew, Burke, Ernzerhof (PBE) functional [43]. On top of the GGA improvement to LDA a non-local term of the exchange-correlation has also been implemented in the DFT-calculations presented in this thesis. This is done in order to better describe the van der Waals interaction. The specific functional used for the calculations presented in this thesis is the optB88-vdW functional [44], based on the Becke 88 GGA functional, which is part of B3LYP.

Chapter 3

Literature overview

This chapter will give a context to the work presented in this thesis and discuss previous work relevant to the subject. The first section will discuss PAHs in general with focus on their interaction with surfaces. The second section will introduce the interaction between atomic H and PAHs, including both neutral and ionized PAHs. The third section will give a short introduction to the interstellar medium (ISM), with focus on PAHs and H₂-formation in the ISM.

3.1 Polycyclic aromatic hydrocarbons

The primary constituents of PAHs are carbon atoms. Carbon is the chemical element with the atomic number 6. It occurs naturally in three different isotopes: ^{12}C accounts for 98.9%, ^{13}C accounts for 1.1%, while the radioactive ^{14}C isotope only exists in trace amounts. Carbon has six electrons, two in the $1s$ -orbital, two in the $2s$ -orbital and two in the $2p$ -orbital. The electrons in the $2s$ - and $2p$ -orbitals are in the valence shell, meaning that they are able to form chemical bonds. When bonding, the spherical s -orbital and the three dumbbell-shaped p -orbitals will hybridize. The most common hybridisation is the sp^3 -hybridisation where the s -orbital and the three p -orbitals hybridize into four equivalent sp^3 -orbitals, allowing carbon to form up to four bonds. When bonding these orbitals will form a tetrahedral structure with an angle of 109.5° between each orbital. The sp^3 -orbitals and their geometry are illustrated in the third row of figure 3.1 and are, for instance, observed in diamond. Carbon can also form three sp^2 -hybridized orbitals, meaning that one p -orbital remains unhybridized. The resulting orbital pattern is illustrated in the second row of figure 3.1 and leads to a planer structure with 120° between each of the sp^2 -orbitals, with the p -orbital perpendicular to the bond axis. The sp^2 -orbitals are, for instance, observed in graphene/graphite. Carbon can also form two sp -orbitals leaving two p -orbitals unhybridized. This orbital structure is illustrated in the first row of figure 3.1 and leads to a linear bond structure, where the two unhybridized p -orbitals are perpendicular to the bond axis and each other. The bonds formed on the bond axis are called σ -bonds, while the bonds formed above and below the bond axis are called π -bonds.

Aromatic hydrocarbons are planar molecules and have to be cyclic, per definition. Furthermore they have to follow the Hückel's rule stating that it has to have $4n + 2$ delocalized π -electrons, where n is zero or any positive integer. The π -electrons are delocalized above and below the planar skeleton. The more extensive this π -electron delocalization is, the more stable the molecule is [1]. The most common aromatic compound is benzene (C_6H_6) containing only one six-membered aromatic ring. PAHs are the group of molecules containing three or more fused aromatic rings, however, when discussing PAHs people often include naphthalene (C_{10}H_8) due to similar physical and chemical properties. Some PAHs are illustrated in figure 3.2. The PAHs can be divided into two different families, the pericondensed (left column of figure 3.2) and the catacondensed (right column of figure

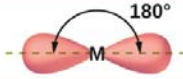
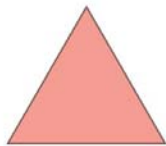
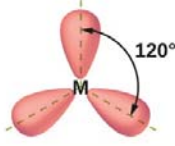
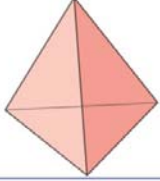
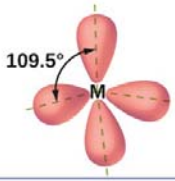
Regions of Electron Density	Arrangement		Hybridization	
2		Linear	sp	
3		Trigonal planar	sp^2	
4		Tetrahedral	sp^3	

Figure 3.1: An illustration of the sp -, sp^2 - and sp^3 -hybridized orbitals and their respective geometry [45].

3.2). The pericondensed PAHs contain C-atoms that are members of three separate rings, i.e. tertiary C-atoms. A subclass of the pericondensed PAHs are the centrally condensed PAHs, where the rings are ordered cyclically around one central ring. The centrally condensed PAHs are among the most stable PAHs, since their structure allows for complete delocalization of the π -electrons [1]. The catacondensed PAHs are more open molecules, since any carbon atom may not be a member of more than two separate carbon rings, i.e. secondary C-atoms only.

In all the experiments presented in this thesis the coronene molecule ($C_{24}H_{12}$) has been used as a model PAH. Coronene is a centrally condensed PAH consisting of 24 carbon atoms where all of the outer edge C-atoms have one hydrogen atom bound to them. This gives the coronene molecule an average mass of 300.33 amu. For a coronene molecule containing only ^{12}C the mass is 300.09 amu. Coronene has an interatomic carbon distance of 1.40 Å [47], very close to the interatomic distance of the basal plan of graphite at 1.41 Å. This is one of the reasons why it is often used as a model for graphite/graphene.

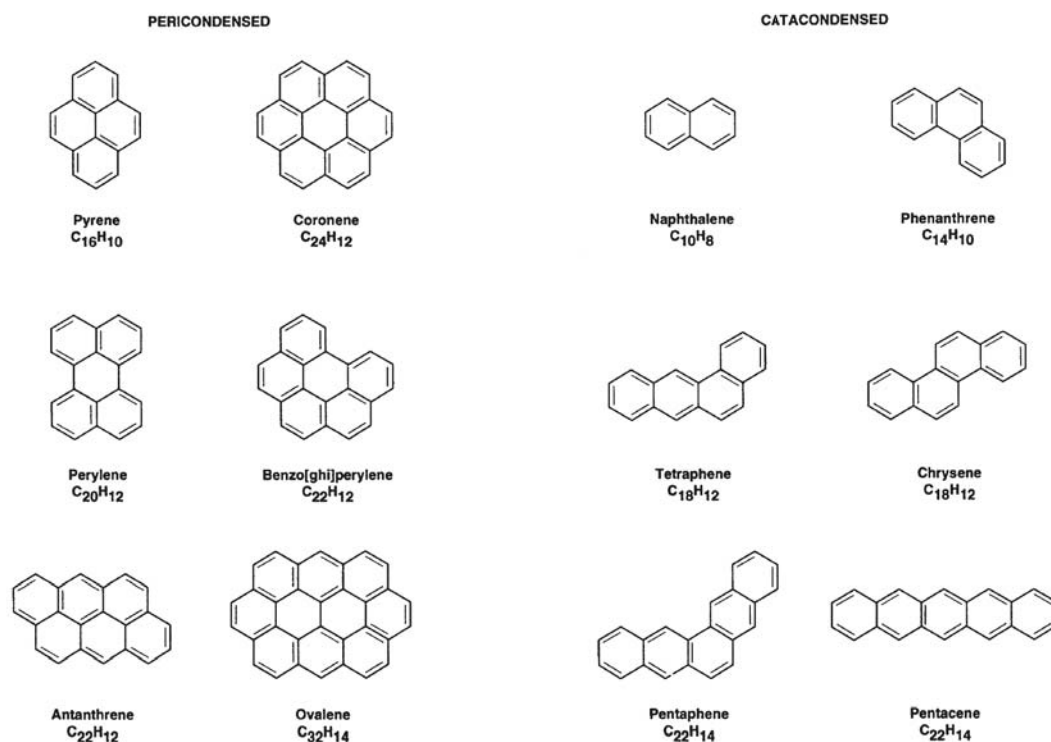


Figure 3.2: The molecular structure of some selected PAHs. The PAHs are arranged in two different families, the pericondensed PAHs on the left and the catacondensed PAHs on the right [46].

3.1.1 PAHs on surfaces

Benzene, naphthalene, and several PAHs have been studied both theoretically and experimentally on a large variety of surfaces. In this thesis the discussion will mainly concern the PAHs on graphite.

PAHs on graphite have previously been studied with TPD, which is the primary technique used in this thesis. Zacharie *et al.* [18] [16] studied the thermal desorption of benzene, naphthalene, coronene and ovalene ($C_{32}H_{14}$) from graphite as a model to investigate the interlayer cohesive energy of graphite. A family of TPD spectra for each species is shown in figure 3.3. Zacharia deduced that benzene (figure 3.3(a)) and naphthalene (figure 3.3(b)) monolayers adsorb flat on the surface and follow simple first-order desorption kinetics, yielding the high temperature peaks in figure 3.3(a) and (b). The low temperature peak was attributed to multilayer desorption following zero-order desorption. Benzene also shows a medium temperature peak, which was attributed to a submonolayer phase change whereby the benzene,

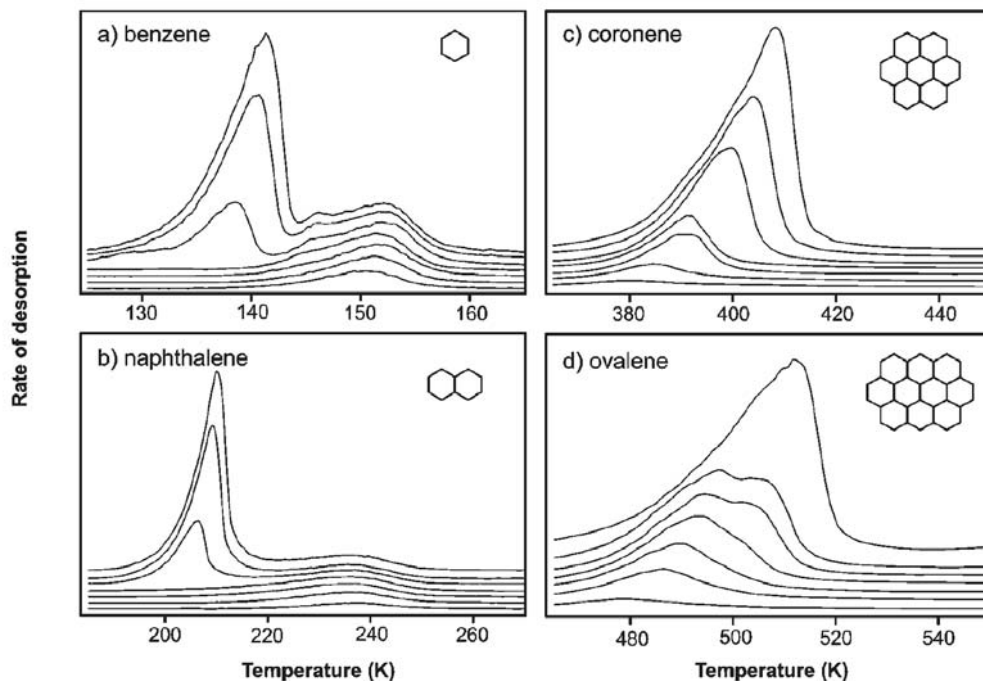


Figure 3.3: Families of TPD spectra from graphite of (a) benzene, (b) naphthalene, (c) coronene and (d) ovalene. The temperature ramp rate was 0.7 K s^{-1} , 1.0 K s^{-1} , 2.0 K s^{-1} , and 2.0 K s^{-1} , respectively [18].

close to monolayer coverage, is oriented with the basal plane perpendicular to the graphite surface to satisfy steric and entropic constraints. This has also been observed with nuclear magnetic resonance measurements [48]. One continuously growing peak was observed for coronene (figure 3.3(c)) and ovalene (figure 3.3(d)) for both monolayer and multilayer. This was attributed to fractional-order kinetics, thought to be due to the high stability of two-dimensional adsorbate islands up to the desorption temperature. The desorption order was determined to be 0.27 ± 0.04 and 0.34 ± 0.01 for coronene and ovalene respectively. This will, for coronene, be disputed by the measurements presented in section 4.1 showing first-order kinetics for the monolayer and zero-order kinetics for the multilayer [49]. Zacharie *et al.* found that benzene, naphthalene, coronene and ovalene monolayers have the following desorption energies using the Falconer-Madix analysis: 0.50 eV, 0.85 eV, 1.40 eV and 2.1 eV [18].

Structural measurements generally confirm that PAHs adsorb flat on graphite. Benzene monolayers on graphite have been studied with several techniques such as LEED and x-ray diffraction suggesting a $\sqrt{7} \times \sqrt{7} \text{ R} \pm$

19.1° superstructure in a hexagonal pattern [50][51]. The phase change reported by Zacheria [18], where the benzene molecules stand perpendicular to the substrate at high coverage have, however, not been observed. For naphthalene a $2\sqrt{3} \times 2\sqrt{3} \text{ R} \pm 30^\circ$ hexagonal pattern has been observed with both STM and LEED [50] [52]. The LEED measurements also suggested a higher density packing phase [50], which later was disputed by STM measurements and attributed to multilayer formation [52]. Yamada *et al.* [52] suggest that the naphthalene molecule adsorb with the basal plane tilted slightly away from parallel to the substrate, based on the apparent height of the individual line profiles in the STM images. No supporting measurements have, however, been found on this subject. Multilayer measurements on naphthalene have also been made with STM, showing the formation of a more complicated superstructure and evidence of a Stranski-Krastanov growth mode.

For coronene monolayers on graphite several studies have investigated the structural growth using both STM and LEED [49] [53] [54] [55]. Images from each of the STM studies are shown in figure 3.4 and will serve as comparison for the STM measurements presented in chapter 5. All measurements show the formation of a $\sqrt{21} \times \sqrt{21} \text{ R} \pm 10.9^\circ$ superstructure on graphite. This structure, as well as recent studies investigating the imaging of coronene molecules with STM [56], will be discussed in greater detail in chapter 5. Lackinger *et al.* also studied submonolayer coverages of coronene on graphite with STM at 20 K, and coronene molecules were observed to be extremely mobile on the surface. Only at step edges were stable coronene islands found to be pinned. Zimmermann *et al.* studied multilayer formation of coronene on graphite with LEED and found evidence of a Stranski-Krastanov growth mode.

Larger PAHs have also been investigated on graphite [53] [57] and in a recent study the adsorption of hexa-peri-hexabenzocoronene (HBC) monolayers on graphite and graphene was investigated with STM, LEED and DFT [57]. Similar to the previously mentioned studies, HBC adsorbs in an hexagonal pattern. Very small shifts in molecular position compared to the graphite lattice were observed: the layer was reported to not be epitaxial to the graphite basal plane. The author attributed this shift to a mismatch between the graphite lattice and the molecular structure. The shift happens in different directions for different domains and is evidence of a long range interaction where molecule-substrate energy is gained by moving the molecules slightly away from epitaxy. In the publication this is referred to as static distortion waves (SDWs).

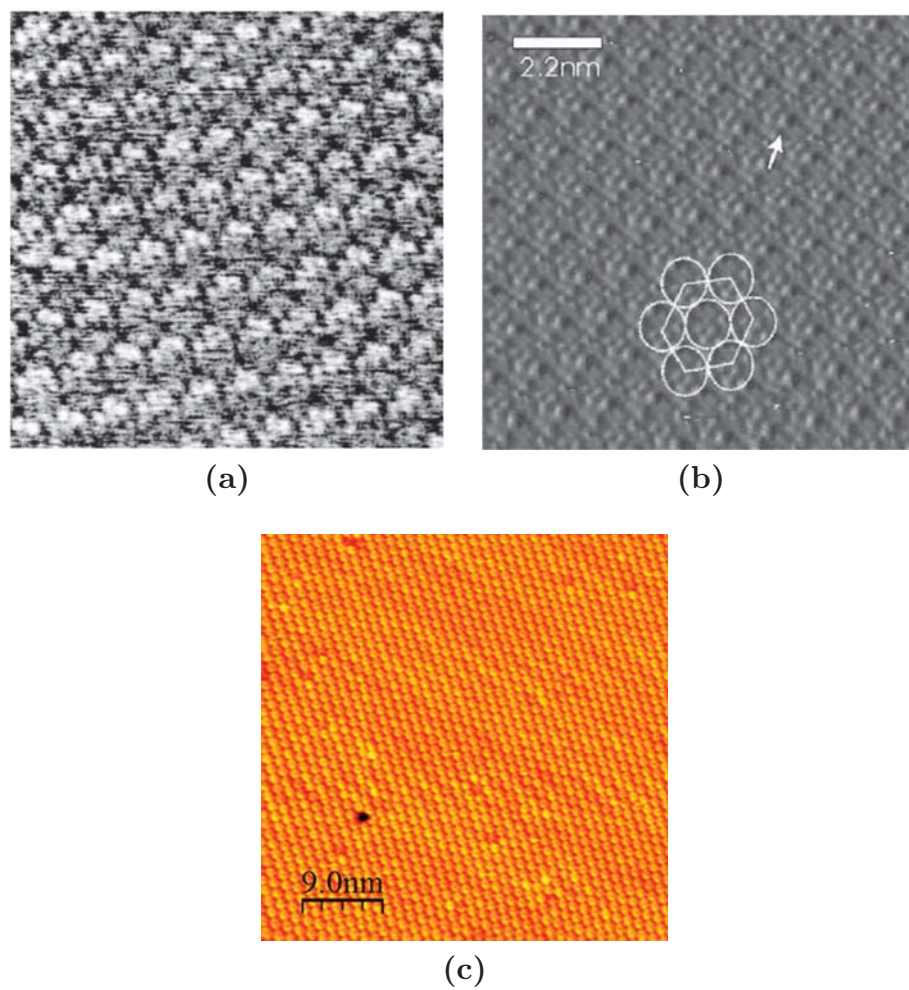


Figure 3.4: Selected STM measurements of a monolayer of coronene on graphite from three different publications. (a) Walzer *et al.* [54] ($90 \times 90 \text{ \AA}$, $V_t = 700 \text{ mV}$, $I_t = 100 \text{ pA}$); (b) Lackinger *et al.* [55] ($V_t = 864 \text{ mV}$, $I_t = 161 \text{ pA}$); (c) Thrower *et al.* [49] ($V_t = -3815 \text{ mV}$, $I_t = 310 \text{ pA}$)

STM measurements of the self-assembly of coronene have been obtained on several other substrates: Cu [58], Ag [59] [58], Ge [60] [61], Si [62] and MoS₂ [54]. On the metal substrates the coronene molecules generally adsorb in a disordered pattern at low coverage, but form a hexagonal pattern at higher coverages similar to the pattern found on graphite (the specific geometry of course depends on the metal and the surface cut). STM measurements of coronene on Ge(001) and Ge(111), on the other hand, showed that the molecules adsorb in an upright position at coverages close to a monolayer [60] [61].

3.2 Interaction between PAHs and atomic hydrogen

Although the interaction between PAHs and atomic hydrogen has mainly been studied through calculations, experimental studies have also been carried out, both for neutrals and ions, within recent years. The main motivation for these studies is often to study the interaction between atomic H and PAHs in relation to the ISM. However, a few studies have also focused on using H-addition to PAHs as a tool to reduce negative health effects of PAHs. Furthermore PAHs have also been suggested as a possible hydrogen storage medium and patents have been obtained [63]. The presented studies might also enlighten if this is energetically favourable. The main focus in this section will be on neutral PAHs, especially coronene.

When a H-atom interact with a PAH molecule there are generally up to 5 different adsorption sites at nearest neighbour level. These are illustrated in figure 3.5. On the edge of the PAH an H-atom can bind to an outer edge site, a secondary C-atom with one H-atom already bound or an inner edge site, a tertiary C-atom, on the edge of the carbon skeleton. Since the edges can have either zigzag or armchair configurations, this results in four different adsorption sites. This, together with a centre site, results in five different adsorption sites [64]. The bonding of a H-atom will change the hybridization of the C-atom from sp^2 to sp^3 resulting in a modification to the local π -electron structure. It will also change the geometry of and strain nearby C-atoms. These changes in the local environment generally lower the barrier for H-addition to adjacent C-atoms, meaning that more different addition sites become energetically accessible.

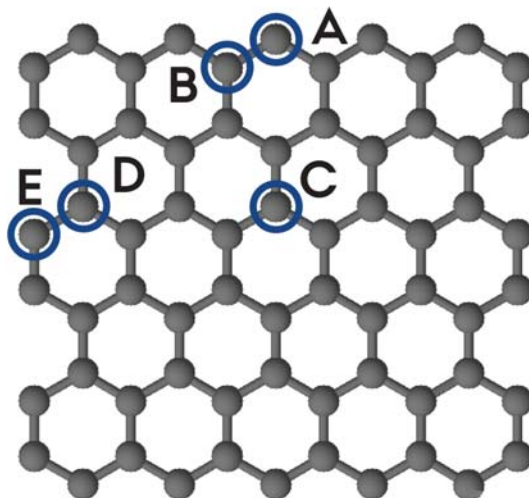


Figure 3.5: The five different adsorption sites on PAH molecules. (A) The outer zigzag edge site, (B) the inner zigzag edge site, (C) the center site, (D) the inner armchair site and (E) the outer armchair edge site [14]

3.2.1 Neutrals

For neutral coronene the barriers for addition and abstraction of hydrogen were studied using DFT by Rauls and Hornekær in 2008 [65]. Since coronene only has zigzag edges, there are initially only three different types of sites; outer edge, inner edge and center. These are illustrated in figure 3.6. The DFT calculations investigated the energetically most favourable route for the first 8 H-additions. This route is illustrated in figure 3.7. For the first addition the lowest barrier is 60 meV and was found for addition at an outer edge site, with a binding energy of 1.45 eV. This barrier is one third that of the other sites and suggest that if the H-atom has sufficient energy to overcome the 60 meV barrier it will bind to an outer edge site. The subsequent addition will find the highest binding energy at the adjacent outer edge site. By tilting the C-C bond the C-H bonds are stabilized and the binding energy of the second H-atom was found to be 3.25 eV. Addition at the adjacent outer edge site has no energy barrier, making this the most likely reaction. For the third hydrogen atom the energetically preferred site is one of the inner edge sites next to the newly hydrogenated outer edge site. The reaction barrier was found to be 30 meV and the binding energy is 1.55 eV. H-atoms no. 4 and 5 can be bound to the neighbouring outer edge sites without any reaction barrier and high binding energies (2.8 - 3 eV).

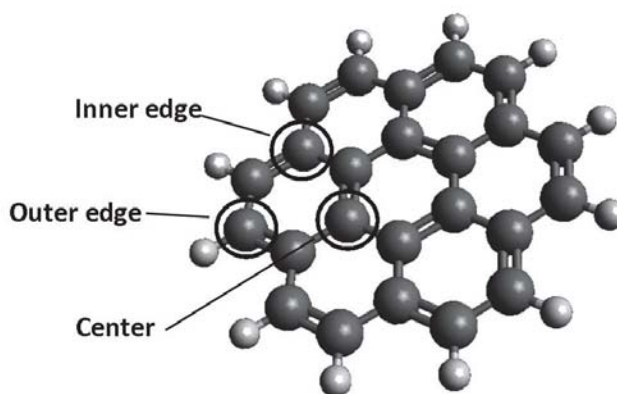


Figure 3.6: Examples of the three adsorption sites on coronene: Outer edge, inner edge and center sites

The sixth H-atom can be bound to the centre site next to H-atom no. 3, without any reaction barrier and a binding energy of 3 eV, if it is adsorbed on the bottom side of the coronene molecule (opposite side of H no. 3). A seventh H-atom can be bound to a neighbouring centre site on top of the molecule, without any reaction barrier and with a binding energy of 1.5 eV. The 8th H-atom can be bound to the neighbouring inner edge site without any barrier and with a binding energy of 3.2 eV. The DFT calculations also examined the barrier for Eley-Rideal abstraction leading to formation of H₂. There is no barrier for abstraction after the first H-addition. In general the highest reaction barrier involved is the 60 meV barrier for addition of the first H-atom, which means that if the H-atoms have sufficient energy to overcome this barrier all of the subsequent reactions should be possible, i.e. superhydrogenated coronene will result, and H₂-formation via abstraction reactions is likely.

Other theoretical studies of the hydrogenation of PAHs include a similar DFT study on pyrene (C₁₆H₁₀) [66], where only two H-atoms were adsorbed. This also showed that the lowest barrier for the first addition is 60 meV, while the subsequent addition is barrierless. The lowest barrier for H₂-formation was found to be 50 meV through Eley-Rideal abstraction, while the lowest barrier through the Langmuir-Hinselwood was found to be 800 meV. The first addition has also been investigated with DFT on anthracene, again giving a barrier of 60 meV, while polyacene (an infinitely extended chain of aromatic rings) yielded a lower barrier of 34 meV due to the partial radical character of their edge C-atoms [67]. A general investigation of the binding energies of

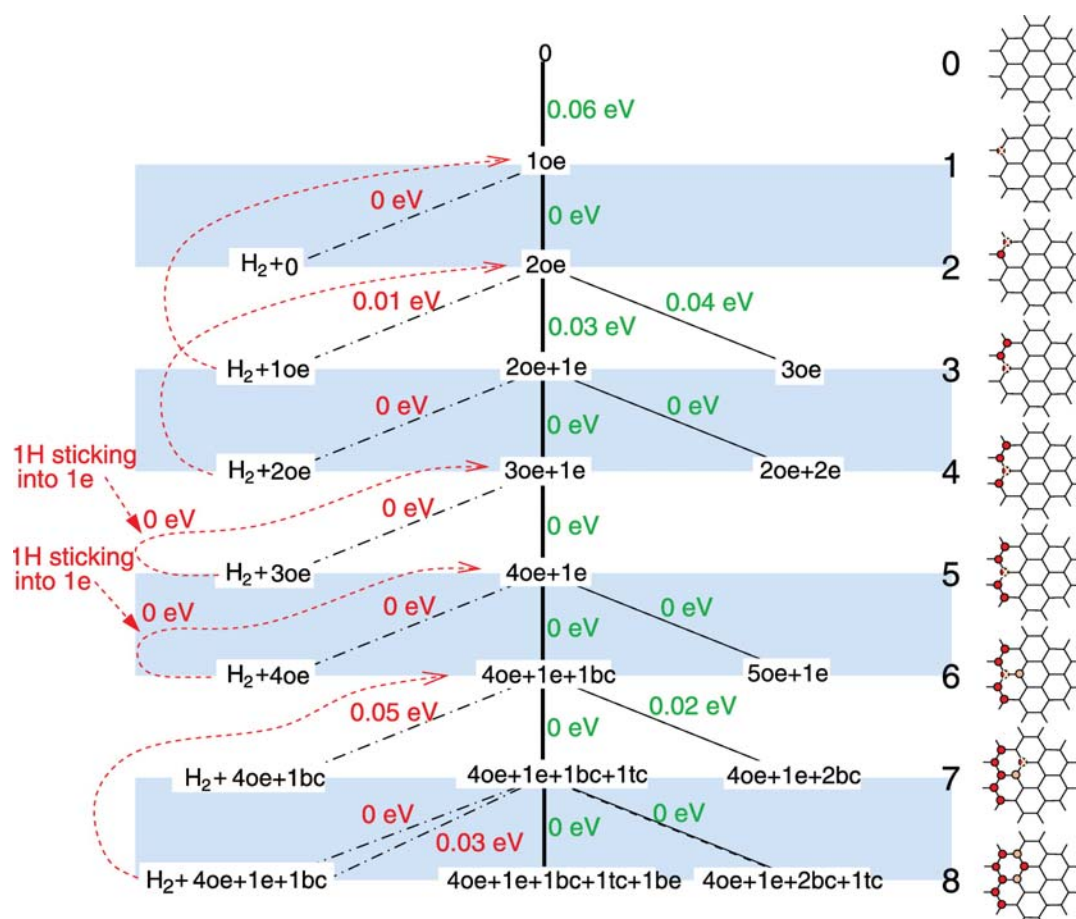


Figure 3.7: Reaction pathways for H-addition to coronene and H₂ abstraction from coronene, as calculated with DFT. The total number of H-atoms involved in each step is shown on the right side of the figure. The centre line in the figure represents the energetically most favourable addition reaction, while the dashed lines going to the left indicate the abstraction reactions and lines going to the right indicate less favourable additions. The resulting structures are described with abbreviations, where *oe* refers an outer edge site, *e* refers to an inner edge site, *tc* refers to a top centre site and *bc* refers to a bottom centre site. To the right the structure of the carbon backbone is also shown [65]

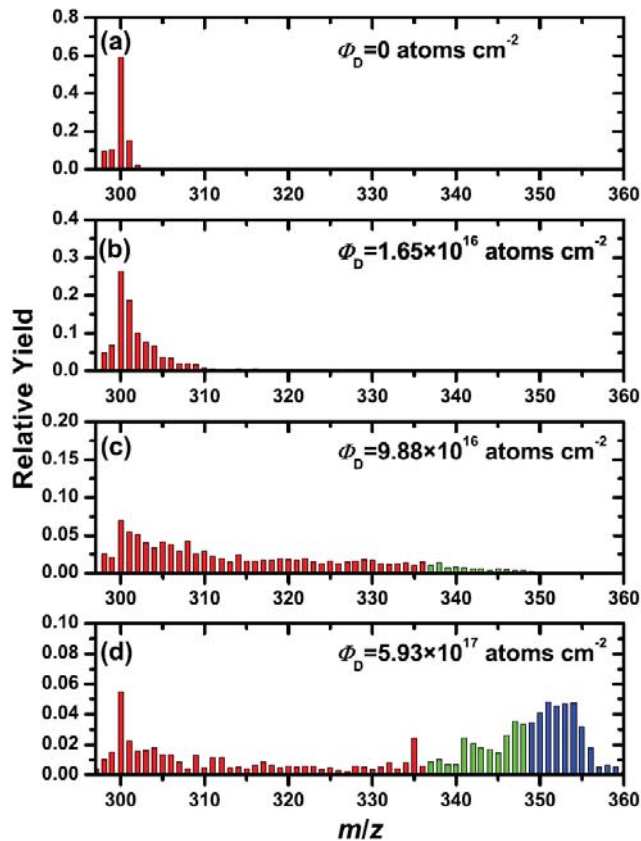


Figure 3.8: Mass distributions of desorbing molecules for a monolayer of coronene on graphite exposed to 4 different D-fluences [71].

the different sites found at a range of PAHs was investigated by Rasmussen in [68] and showed that the favoured position for the first addition always is an outer edge site. Similar results were found by Bonfanti *et al.* [69]. A DFT study by Goumans [70] investigated hydrogenation of pyrene through quantum tunneling at low temperatures, which may be relevant in cold parts of the ISM. It was found that at 40 K the rate of addition was non-negligible and a large isotope effect was found between the rate constant of H (k_H) and D (k_D), $k_H/k_D \approx 64$.

The interaction between H-atoms and coronene has been investigated experimentally by both Thrower *et al.* [72] [71] and Mennella *et al.* [73] [74]. In [71] the study was carried out at the Big Chamber in the SDL group. Here coronene monolayers on graphite were exposed to different atomic D fluences and subsequently heated while measuring the masses of the desorbing species. Some of the resulting mass distributions are shown in figure 3.8. Masses above 348 amu are observed, as shown in figure 3.8(d), and

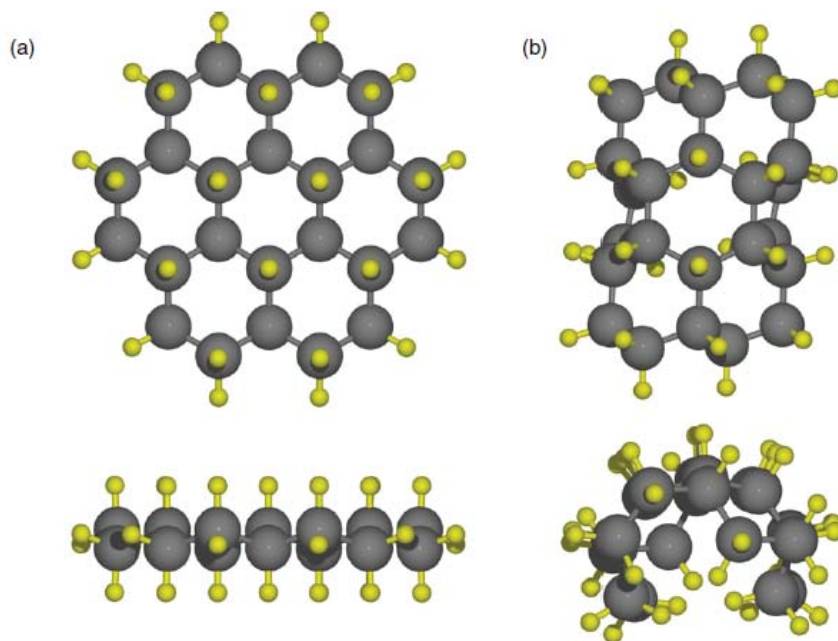


Figure 3.9: The relaxed structures of (a) trans-perhydrocoronene and (b) cis-perhydrocoronene calculated with DFT [71].

these masses can only be reached if substitution of the original H-atoms with D-atoms takes place. This suggests that superhydrogenated coronene can work as a catalyst for H_2 -formation, since the substitution is expected to happen through abstraction of an HD-molecule following the Eley-Rideal mechanism. This experiment is similar to those presented in section 4.2 and more in depth discussion about the results are obtained there. Throrer *et al.* [71] also included DFT calculations investigating the stability of coronene depending on which side of the molecule the hydrogenation takes place. This shows that both for the completely double-sided hydrogenation, creating trans-perhydrocoronene ($C_{34}H_{36}$) (figure 3.9(a)), and for the completely single-sided hydrogenation, creating cis-perhydrocoronene figure (3.9(b)), the molecules are stable. An important thing to notice is that the cis-perhydrocoronene molecule buckles in order to relax. This is expected to have an effect on the interaction between hydrogenated coronene and graphite, as shown in section 4.4. Another conclusion is that the most stable route to the formation of cis-perhydrocoronene is found if the center ring is hydrogenated last.

Mennella *et al.* [74] studied the hydrogenation of coronene using infrared (IR) spectroscopy. Coronene multilayers of 150 - 180 nm were prepared on

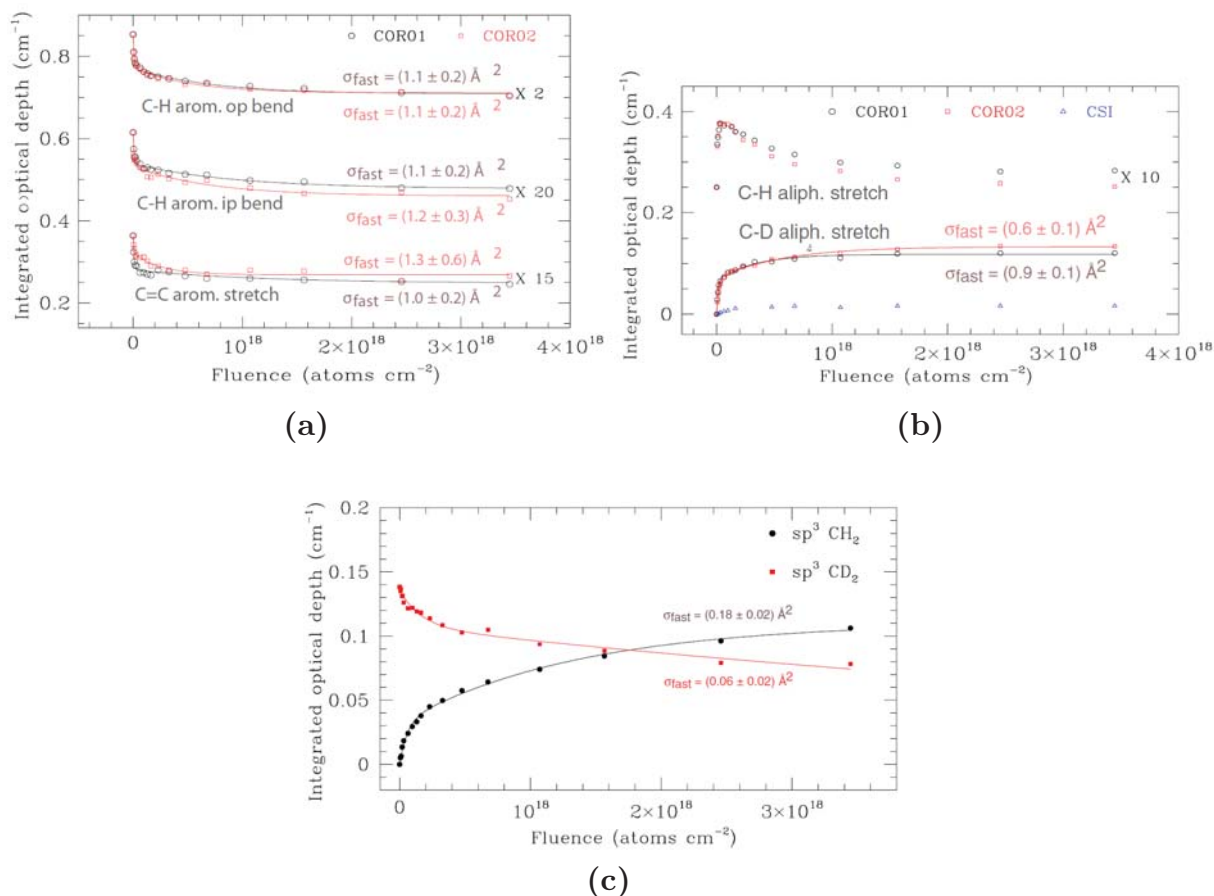


Figure 3.10: (a) and (b) shows the change in C-H aromatic out-of-plane bend, C-H aromatic in-plane bend, C=C aromatic stretch, C-H aliphatic stretch and C-D aliphatic stretch as measured with IR spectroscopy of a coronene film during deuteriation. (c) shows the change in aliphatic C-D stretch and aliphatic C-H stretch as measured with IR spectroscopy during a subsequent hydrogenation [74]

CsI substrates and exposed to 300 K D-atoms while measuring the evolution of the IR-spectrum. The results are shown in figure 3.10(a) and (b). The C-H aromatic out-of-plane bend, the C-H aromatic in-plane bend and the C=C aromatic stretch are observed to decrease upon exposure of the coronene film to a fluence of D, with a reaction cross-section of around 1.1 \AA^2 (figure 3.10(a)). This shows the clear change from sp^2 - to sp^3 -hybridisation expected when adding D to the coronene molecule. The C-H aliphatic stretch initially increases until a fluence of $5 \cdot 10^{16} \text{ atoms cm}^{-2}$ and then decreases, while the C-D aliphatic stretch increases with a cross-section of $0.6 - 0.9 \text{ \AA}^2$. This is illustrated in figure 3.10(b) and shows the exchange of H for D, which is presumed to occur through the abstraction of HD-molecules. The

samples were also subsequently exposed to atomic H and the aliphatic C-D stretch decreased, while the aliphatic C-H stretch increased, again showing substitution through abstraction of HD, as shown in figure 3.10(c). The estimated HD abstraction cross-section was found to be $0.06 \pm 0.02 \text{ \AA}^2$.

Experiments on the hydrogenation of other neutral PAHs have not been conducted. However, experiments have been carried out on hydrogenated benzene on graphite covered Pt(111) [75] and on Cu(111) [76]. In the study on Pt(111), the crystal was covered with a monolayer of graphite, which we would now call graphene. A monolayer of benzene was deposited and the sample was exposed to D-atoms. The reaction was studied with TPD and high resolution electron energy loss spectroscopy. The addition cross-section of D was found to be 8 \AA^2 . Eley-Rideal abstraction was observed, but the abstraction cross-section could not be measured. An abstraction cross-section of 1.7 \AA^2 was, however, measured for 1,4-dimethyl-cyclohexane (the fully hydrogenated version of benzene with two methyl groups, C_8H_{16}). These cross-sections seem high compared to that measured for coronene on graphite, however, graphene, on some metal substrates, is known to be easier to hydrogenate than graphite, which might speed up the reaction. On top of that benzene might be easier to hydrogenate, because of the smaller π -electron system. For Cu(111) the experiment was similar and an addition cross-section of 15 \AA^2 was measured, although the errors were stated to be one order of magnitude. The abstraction cross-section for cyclohexane (the fully hydrogenated version of benzene, C_6H_{12}) on Cu(111) was found to be 0.5 \AA^2 [77].

The absorption of light by a superhydrogenated PAH is also expected to lead to H_2 desorption. This has been studied experimentally and theoretically for the slightly hydrogenated PAH 9,10-dihydroanthracene (DHA, $\text{C}_{14}\text{H}_{12}$) [78]. The DHA molecules were trapped in an Ar matrix and irradiated with UV light from a Hg-lamp, while measuring the IR absorption spectrum of the Ar/DHA matrix. After long exposures the appearance of anthracene bands were observed, suggesting the desorption of hydrogen. After the experiments the Ar/DHA matrix was subsequently evaporated and a slight increase in H_2 was observed compared to that from an irradiated Ar matrix. DFT calculations showed the lowest barrier for H desorption to be through H_2 -formation from the H-atoms on the two sp^3 -hybridized carbon atoms, rather than the desorption of two individual H-atoms.

Many PAHs are toxic, carcinogenic, and/or teratogenic [10] and are therefore unwanted in emission from cars, power plants, factories, etc.. Re-

moving the aromaticity of PAHs, by changing the carbon hybridisation from sp^2 to sp^3 , will reduce their negative health effects. Hydrogenation of neutral PAHs has been suggested as a way of achieving this and has been studied in this context as well [79] [80] [81]. The reactions investigated are generally very different from our work. A recent example includes hydrogenation of PAHs on high-density-polyethylene-stabilized Pd nanoparticles held at 40 - 50 °C in supercritical CO₂, with a CO₂ pressure of 20 MPa and a H₂ pressure of 1 MPa [81].

3.2.2 Ions

PAH cations have also been studied in an astrochemical context. Bauschlicher [82] investigated the addition and abstraction of H and D on naphthalene cations using DFT. Low or no barriers were found for addition of the first two H-atoms. Bauschlicher highlights that the additions were found to be very exothermic, which could render small PAHs unstable. Abstraction of H₂ by an incoming H-atom was described as having virtually no barrier (11 meV). The abstraction of HD had a slightly higher barrier (29 meV), suggesting that this can lead to D enrichment of the PAHs. Hirama *et al.* found similar results with DFT for the first additions of H to anthracene and pyrene [83]. The hydrogenation of naphthalene was revisited by Ricca *et al.* [84] with similar results to that found by Bauschlicher [82] for the first two additions, with only the second additions having a barrier (30 meV). Higher degrees of hydrogenation were also investigated in this study showing that after the second addition all the secondary carbons can be hydrogenated without any barrier if the lowest energy route is followed.

Experiments on the hydrogenation of naphthalene cations were carried out by Le Page *et al.* [85] and Snow *et al.* [86]. Here the first two hydrogenation levels after exposure to atomic H were investigated. High rate constants of $1.9 \cdot 10^{-10} \text{ cm}^3 \text{ s}^{-1}$ and $4 \cdot 10^{-12} \text{ cm}^3 \text{ s}^{-1}$ were found for the first and second additions to naphthalene respectively. The same study was also carried out for pyrene in [86] with similar results; $1.4 \cdot 10^{-10} \text{ cm}^3 \text{ s}^{-1}$ and $3 \cdot 10^{-12} \text{ cm}^3 \text{ s}^{-1}$ for the first and second addition respectively.

Klærke *et al.* [87] studied the hydrogenation of pentacene (C₂₂H₁₂) cations experimentally as well as theoretically using DFT. It was found that pentacene could be driven to complete hydrogenation at the secondary C-atom sites, while the tertiary C-atom remained unhydrogenated. A clear difference was also observed between the measured yield of the molecules hydro-

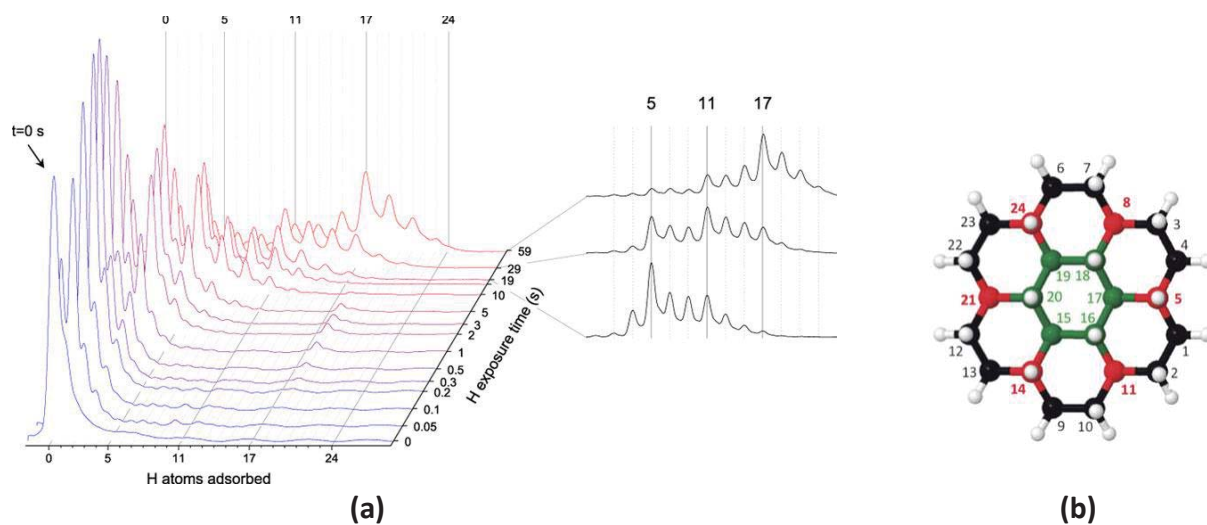


Figure 3.11: (a) Mass distributions of coronene cations after exposure to different fluences of atomic H. The distributions for the three highest fluences are highlighted. (b) Illustration of the lowest energy hydrogenation route determined with DFT. Modified from [89]

generated with an odd or even number of H-atoms, specifically the molecules hydrogenated with an odd number of H-atoms were significantly more stable, due to their closed shell configuration.

The hydrogenation of coronene cations was studied both experimentally and theoretically using DFT by Boschman *et al.* [88] and Cazaux *et al.* [89]. Boschman *et al.* [88] found a clear dominance of the odd masses in the experimental mass spectrum, in agreement with the higher stability of closed shell molecules mentioned by Klærke *et al.* [87]. Experimentally determined barriers for the second and fourth additions were found to be 72 meV and 40 meV respectively, while the first and third additions were thought to be barrierless. They continued the studies in [89] and included DFT calculations to estimate some of the barriers. The experiments showed higher stability of the odd hydrogenation states, moreover the 5th, 11th and 17th hydrogenation state were found to have extra high stability. These results are shown in figure 3.11(a). The reaction route, shown by the numbers in figure 3.11(b), was calculated with DFT to be the most likely. The largest barriers were found for addition of the 6th, 12th and 18th H-atom. These barriers were 110 meV, 170 meV and 320 meV respectively, supporting the high stability of the 5th, 11th and 17th hydrogenation state.

Light induced H₂ desorption from hydrogenated PAH cations has also

been investigated experimentally. Vala *et al.* [90] and Szczepanski *et al.* [91] investigated IR multiphoton dissociation of 1,2-dihydronaphthalene, acenaphthene ($C_{12}H_{11}$) and 9,10-dihydrophenanthrene ($C_{14}H_{13}$) cations. In all cases a loss of two H-atoms was measured and DFT calculations suggest that the lowest energy barriers are for loss of H_2 when compared with loss of 2 H-atoms. Zhen *et al.* [92] [93] investigated the effects of exposing PAH cations to high energy UV light (7 - 40 eV). These studies generally show that smaller PAHs lose two H-atoms, while larger PAHs get doubly ionized. Whether this leads to the formation of H_2 or 2 H was not investigated further. The effects of collision between high energy He^+ -ions and hydrogenated PAH cations have also been studied in several cases [94] [95] [96]. One of the more interesting results was found by Chen *et al.* [95], who through He^+ collision experiments and DFT calculations, found that H_2 -formation becomes important when the internal temperature of the molecule exceeds ~ 2200 K, regardless of the PAH size and the excitation agent.

3.2.3 Summary

In summary neutral PAHs show barriers for the first addition, of around 60 meV at the outer edge sites, while the subsequent additions have lower or vanishing barrier. For cations, on the other hand, the first H-addition has a low or no barrier because of the closed shell nature of this configuration. The second addition to cations generally has the highest addition barrier, of any of the secondary C-atoms, ranging from around 30 meV to 70 meV. As discussed for coronene cations, however, some hydrogenation levels show higher stability and higher barriers occur for subsequent hydrogenations. H_2 -formation via abstraction reactions is possible after the first addition; for neutrals with no barrier and with low barriers for cations (~ 10 meV), meaning that cations should be able to catalyse H_2 -formation from H-atoms with energies as low as 10 meV and neutrals for H-atom with energies above 60 meV. These barriers have been investigated mostly through DFT calculations and further experimental studies are in many cases still needed to confirm this and determine the specific hydrogenation route of the molecules. Both ions and neutrals might be prone to fragmentation due to the exothermic nature of the addition reaction, especially for small PAHs. This will probably not be a problem for neutral PAHs on surfaces, since the surface can absorb the excess energy. In relation to the ISM, the PAHs investigated are generally too small to be stable in the ISM, as will

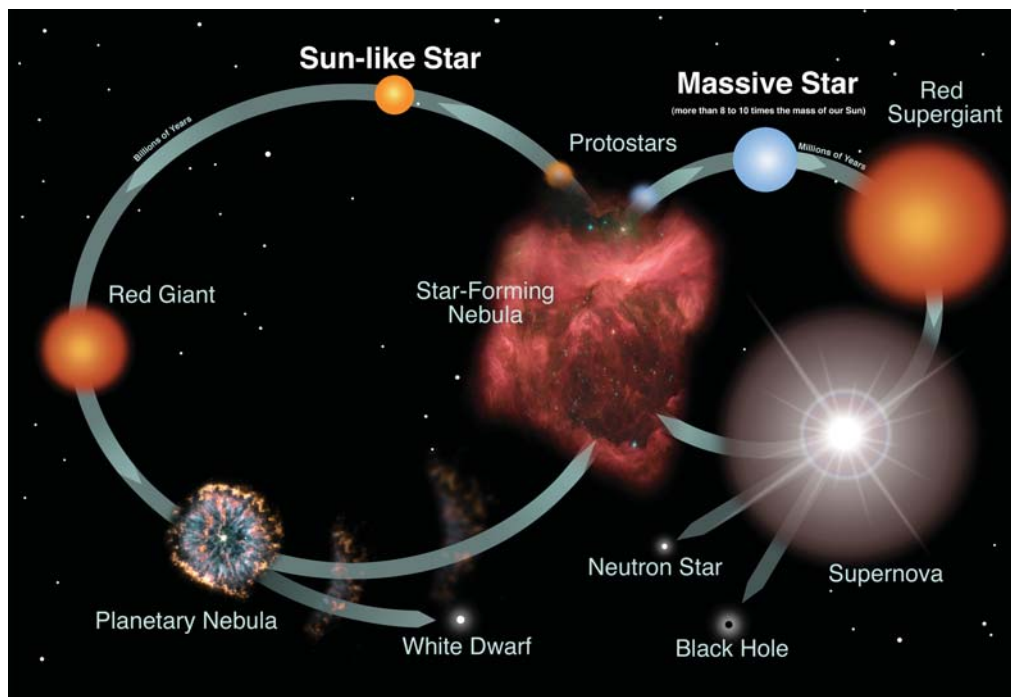


Figure 3.12: Illustration of the lifecycle of a sun-like star and a massive star [100]

be discussed in section 3.3. However because of experimental and computational limitations larger PAHs can often not be used, meaning that results will have to be extrapolated to be applicable in the ISM.

3.3 The interstellar medium

The interstellar medium (ISM) is the region of a galaxy situated between stars. It has been estimated that stars and planetary systems only occupy $3 \cdot 10^{-8}\%$ of the volume of our galaxy [1], meaning that most of our galaxy is ISM. The ISM is relatively empty, with densities ranging from $100 - 10^{12}$ atoms m^{-3} [97], compared to $3 \cdot 10^{35}$ atoms m^{-3} in the Earth's atmosphere. On top of that there can be a high flux of high energy photons and temperatures can vary from ~ 5 K to $\sim 10^4$ K [97]. Despite this harsh environment the ISM still contains a large variety of molecules and larger particles. The ISM is essentially where stars and planets are formed and furthermore the molecules formed there have been suggested to be important in the creation of life [98]. This section is largely based on reference [1], [2] and [99], which give an introduction to the ISM and molecules in the ISM.

The formation of stars begins and ends in star-forming nebulae, as illustrated for a sun-like star and a massive star in figure 3.12. The star-forming nebulae are generally divided into two different types of clouds, based on their chemical and physical properties; diffuse and dense clouds.

The diffuse clouds are low density clouds. The density of these regions is typically $\sim 5 \cdot 10^7$ atoms m^{-3} and the temperatures are ~ 80 K. Typical sizes are ~ 10 pc and masses are $\sim 500M_{\odot}$ [101]. Diffuse clouds are quite transparent, meaning that ultraviolet (UV) photons play an important role in the physical and chemical environment. The high UV flux hinders the build up of large and complex molecules and the diffuse clouds are dominated by atomic gas and small molecules typically consisting of 2 - 5 atoms [2]. These molecules often exist as radicals or ions. Hydrogen predominantly exists as atomic H, which can be detected through the 21 cm emission line associated with a hyperfine transition in the ground state. However, H_2 is also present and can be detected directly through the Lyman and Werner bands.

Larger molecules are found in the dense clouds also known as giant molecular clouds (GMCs). GMCs have average densities of $\sim 1.5 \cdot 10^8$ atoms m^{-3} and average temperatures of (~ 10 K). Typical sizes are 40 pc and masses of $\sim 4 \cdot 10^5 M_{\odot}$. It is, however, important to note that these clouds are not uniform and they contain denser areas, like dark clouds and prestellar cores, with densities up to $\sim 10^{12}$ atoms m^{-3} and temperatures down to ~ 6 K [102]. This is the birth place of new stars. Photodominated/Photodissociation regions (PDRs), on the other hand, are parts of the GMCs subject to higher radiation fields and have higher temperatures and the chemistry is dominated by photodissociation [1]. Most of the GMC is shielded from this radiation field and therefore contain a larger variation of molecules than diffuse clouds, as their name suggest. Presently around 170 individual molecules have been identified, as shown in table 3.1. High energy UV photons often do not penetrate these areas, resulting in a H_2/H ratio approaching unity. The lack of UV photons, however, mean that H_2 is not directly observable and therefore CO is often used as tracer, since it can be observed through the $J = 1-0$ transition line. Molecular clouds are the active sites of star formation, upon which the cloud can be destroyed through stellar winds, heat and radiation.

Besides molecules, larger particles are also found in the ISM. They can range from large carbonaceous molecules like PAHs, fullerenes and diamondoids to micrometer sized dust particles. These dust particles are primarily

Simple hydrides, oxides, sulfides, halogens				
H ₂ (IR, UV)	CO	NH ₃	CS	HCl
O ₂	H ₂ O ₂	PO	CO ₂ (IR)	NaCl ^a
H ₂ O	SO ₂	OCS	H ₂ S	KCl ^a
PN	SiO	SiH ₄ ^a (IR)	SiS	AlCl ^a
N ₂ O	CH ₄ (IR)	HSCN	HF	AlF ^a
HONC	HNCO	AlOH		
Nitriles and acetylene derivatives				
C ₂ (IR)	HCN	CH ₃ CN	HNC	C ₂ H ₄ ^a (IR)
C ₃ (IR,UV)	HC ₃ N	CH ₃ C ₃ N	HNCO	C ₂ H ₂ (IR)
C ₅ ^a (IR)	HC ₅ N	CH ₃ C ₅ N	HNCS	C ₆ H ₂ (IR)
C ₃ O	HC ₇ N	CH ₃ C ₂ H	HNCCC	C ₃ H ₆
C ₃ S	HC ₉ N	CH ₃ C ₄ H	CH ₃ NC	C ₃ H ₇ CN
C ₄ Si ^a	HC ₁₁ N	CH ₃ C ₆ H	HCCNC	
H ₂ C ₄	HC ₂ CHO	CH ₂ CHCN	CH ₂ CCHCN	
Aldehydes, alcohols, ethers, ketones, amides				
H ₂ CO	CH ₃ OH	HCOOH	HCOCN	CH ₃ CH ₂ CN
CH ₃ CHO	CH ₃ CH ₂ OH	HCOOCH ₃	CH ₃ NH ₂	NH ₂ CH ₂ CN
CH ₃ CH ₂ CHO	CH ₂ CCHOH	CH ₃ COOH	CH ₃ CONH ₂	NH ₂ CN
NH ₂ CHO	(CH ₂ OH) ₂	(CH ₃) ₂ O	H ₂ CCO	CH ₂ CHCN
CH ₂ OHCHO	(CH ₃) ₂ CO	H ₂ CS		
C ₂ H ₅ OCHO		CH ₃ SH		
Cyclic molecules				
C ₃ H ₂	SiC ₂	<i>c</i> -C ₃ H	CH ₂ OCH ₂	C ₆ H ₆ (IR) ?
<i>c</i> -SiC ₃	H ₂ C ₃ O	C ₂ H ₄ O		
Molecular cations				
CH ⁺	CO ⁺	HCNH ⁺	OH ⁺	HN ₂ ⁺
CH ₃ ⁺	HCO ⁺	HC ₃ NH ⁺	H ₂ O ⁺	H ₃ ⁺ (IR)
HS ⁺	HOC ⁺	H ₂ COH ⁺	H ₃ O ⁺	SO ⁺
HCS ⁺	HOCO ⁺	CF ⁺	HCl ⁺	H ₂ Cl ⁺
Molecular anions				
C ₄ H ⁻	C ₆ H ⁻	C ₈ H ⁻		
CN ⁻	C ₃ N ⁻	C ₅ N ⁻		
Radicals				
OH	C ₂ H	CN	C ₂ O	C ₂ S
CH	C ₃ H	C ₃ N	NO	NS
CH ₂	C ₄ H	HCCN ^a	SO	SiC ^a
NH (UV)	C ₅ H	CH ₂ CN	HCO	SiN ^a
NH ₂	C ₆ H	CH ₂ N	C ₅ N ^a	CP ^a
SH	C ₇ H	NaCN	KCN	MgCN
C ₃ H ₂	C ₈ H	MgNC	FeCN	
C ₄ H ₂	HNO	H ₂ CN	HNC ₃	HO ₂
C ₆ H ₂	AlNC	SiNC	C ₄ Si	SiCN
HCP	CCP	AlO		
Fullerenes				
C ₆₀ (IR)	C ₇₀ ^a (IR)	C ₆₀ ⁺ (VIS) ?		

^aThese species have been detected only in the circumstellar envelope of carbon-rich stars.**Table 3.1:** Identified interstellar and circumstellar molecules [2]

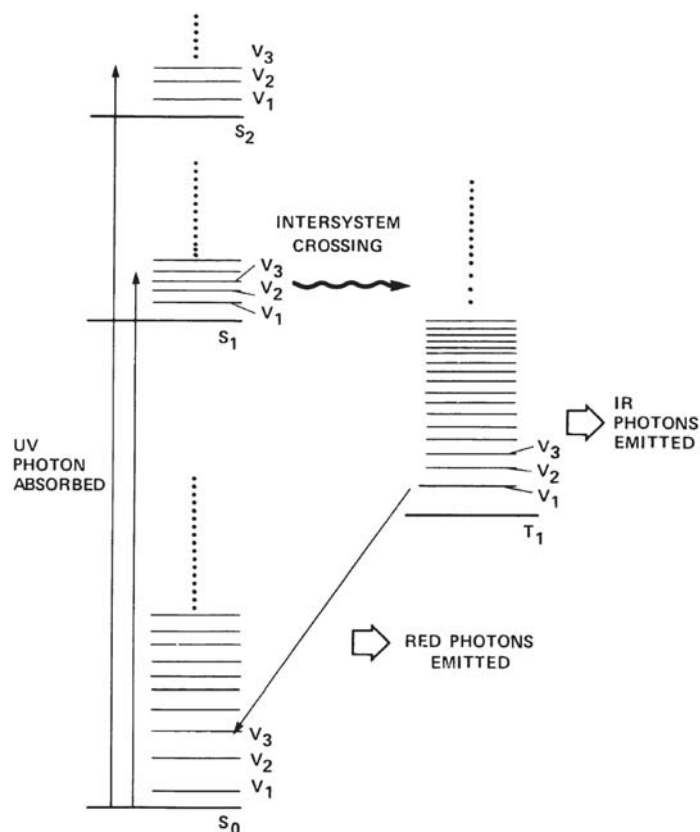


Figure 3.13: Energy level diagram showing excitation and relaxation routes for a PAH molecule [107]

carbonaceous or siliceous and contain metals like magnesium and iron [103]. In cold regions of the ISM the dust grains are covered by ice, consisting mainly of water but other molecules as CO, CO₂, CH₃OH, NH₃, etc. have also been observed [104]. Dust grains are generally thought to be very important for the formation of molecules in the ISM, working as catalysts as well as a meeting place for molecules and atoms.

3.3.1 PAHs in the ISM

PAHs were first identified in the ISM 1984 by Leger and Puget in 1984 [105] and in 1985 by Allamandola *et al.* [106]. PAHs are now thought to be ubiquitous to the ISM and account for 5% to 20% of all carbon in the ISM [6] [7].

PAHs can be detected through their interaction with light. In the ISM PAHs are electronically excited through absorption of UV photons. The en-

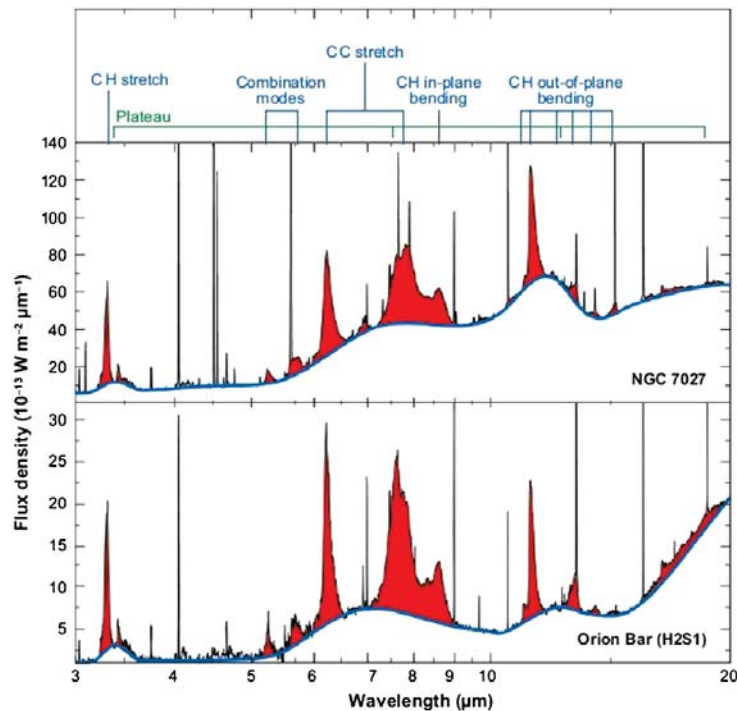


Figure 3.14: The mid IR spectra from two different PDRs. The association with known features from certain vibrational modes in PAHs are labeled in the top [2]

energy diagram in figure 3.13, shows that an UV photon can excite the molecule from its ground singlet state, S_0 , to the S_1 , S_2 , S_3 , etc. state. The molecule can then relax through a variety of processes. In a low density environment the most common one will be through the internal conversion from an excited electronic state to a highly vibrationally excited state in the underlying electronic state. The molecule can also undergo intersystem crossing to a vibrationally excited triplet state, as illustrated in figure 3.13. This means that the PAHs can relax through a combination of visible emission due to electronic relaxation (fluorescence/phosphorescence), as well as IR emission due to vibrational relaxation. Other important relaxation processes in the ISM include ionisation and photodissociation.

The IR spectra from almost all interstellar objects are dominated by features at 3.3, 6.2, 7.7, 11.3 and 12.7 μm [99] [105] [106] [107] [108], as well as some weaker features. For a long time the origin of these features was unknown and they were named the unidentified IR bands (UIR). Now they are generally thought to be from the vibrationally excited PAHs and the specific wavelengths can be related to known vibrational modes in aromatic molecules. The bands are therefore now referred to as the aromatic IR bands

(AIR). An example of the AIR from two PDRs is shown in figure 3.14. In this figure the vibrational modes responsible for the observed peaks have been labelled. The $3.3 \mu\text{m}$ band corresponds to an aromatic C-H stretching mode, the $6.2 \mu\text{m}$ band corresponds to a C-C stretching mode, the $7.7 \mu\text{m}$ band corresponds to C-H in-plane bending, while the $11.3 \mu\text{m}$ band corresponds to out of plane C-H bending. The IR-spectra of multiple PAHs have been investigated both experimentally [109] [110] [111] and theoretically [112] [113] and are used for comparison with spectra from observations [114] [115].

By comparing ratios between the observed features several things can be deduced about the PAH in the ISM. By calculating the typical emission temperature an estimate for the size of the emitting molecules can be made. This suggests that the size of PAHs are typically 50-150 C-atoms [2] [99]. Smaller PAHs are thought to photo-dissociate, while larger PAHs will instead start forming van der Waals carbon clusters and, in the end, nano-sized carbon grains [116] [117]. It is also worth mentioning that interstellar PAHs exist in different charge states. This can be deduced by looking at the ratios of the different IR emission bands, for instance, the C-C stretching mode versus the C-H bending mode. They are often found as cations in regions with intermediate to high UV flux where they have lost electrons due to photo ionization [2]. They can also be found as anions [2]. The charge state will have an influence on their chemistry. In certain areas of the ISM bands potentially attributable to superhydrogenated PAHs are also observed. These include the aliphatic features at 3.4 , 6.9 and $7.25 \mu\text{m}$, relating to a CH-stretching mode and two CH in-plane bending modes respectively [11] [12]. It is still debated whether they are due to excess hydrogenation of PAHs, side groups attached to the PAHs or other aliphatic molecules [2].

The formation of PAHs in the ISM is still poorly understood and a subject of current research. There are two overall approaches to the formation of PAHs, bottom-up or top-down. The bottom-up approach suggest a route to PAH formation similar to that in soot formation, through the aromatication of acetylene (C_2H_2). The limiting step in this process is the transfer from aliphatic to aromatic. Cherchnef [118] highlights four reaction routes for the formation of benzene (C_6H_6) or phenyl radicals ($\text{C}_6\text{H}_5^\bullet$). These formation routes starts with either two propargyl radicals ($\text{C}_3\text{H}_3^\bullet$) [119], 1-buten-3-ynyl (C_4H_3) [120] and C_2H_2 , or 1,3-butadienyl ($\text{C}_4\text{H}_5^\bullet$) and C_2H_2 [121]. The reactions look like this:

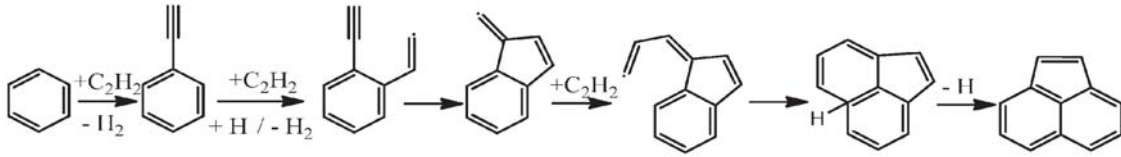
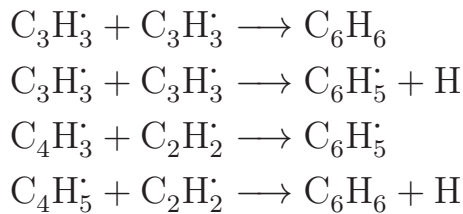


Figure 3.15: A suggested formation route for PAHs after the first aromatic ring is closed [123]



Once the first aromatic ring is closed larger PAHs will be able to grow from this through reactions with C_2H_2 and the abstraction of H [120]. One of the suggested growth processes is illustrated in figure 3.15 [118]. These reactions generally require high temperatures (900 K - 1100 K) and densities, and are therefore limited to the stellar ejecta of asymptotic giant branch stars [118]. Reaction routes suggesting ion-molecule reactions have also been suggested [122] and a recent publication has shown that SiC grains can catalyse the formation of PAHs from C_2H_2 [123], suggesting this as a possible route. The top-down approach generally involves the destruction of larger carbon dust grains by shocks from supernova explosions [124] [125]. The grain remnants might include PAHs or PAH fragments, which can be used to form PAHs. A recent paper has also suggested that PAHs can be formed through the etching of graphene layers on SiC with atomic H, as an alternative top-down approach [126].

3.3.2 Molecular hydrogen formation

H_2 is by far the most abundant molecule in the ISM and is of great importance to several processes in the ISM. First of all H_2 -molecules together with other small molecules are important in the cooling of molecular clouds, because of the vibrational and rotational energy levels available through which the excess energy can irradiate and escape the cloud. H_2 also helps to shield the inner parts of molecular clouds, due to photodissociation of the H_2 in

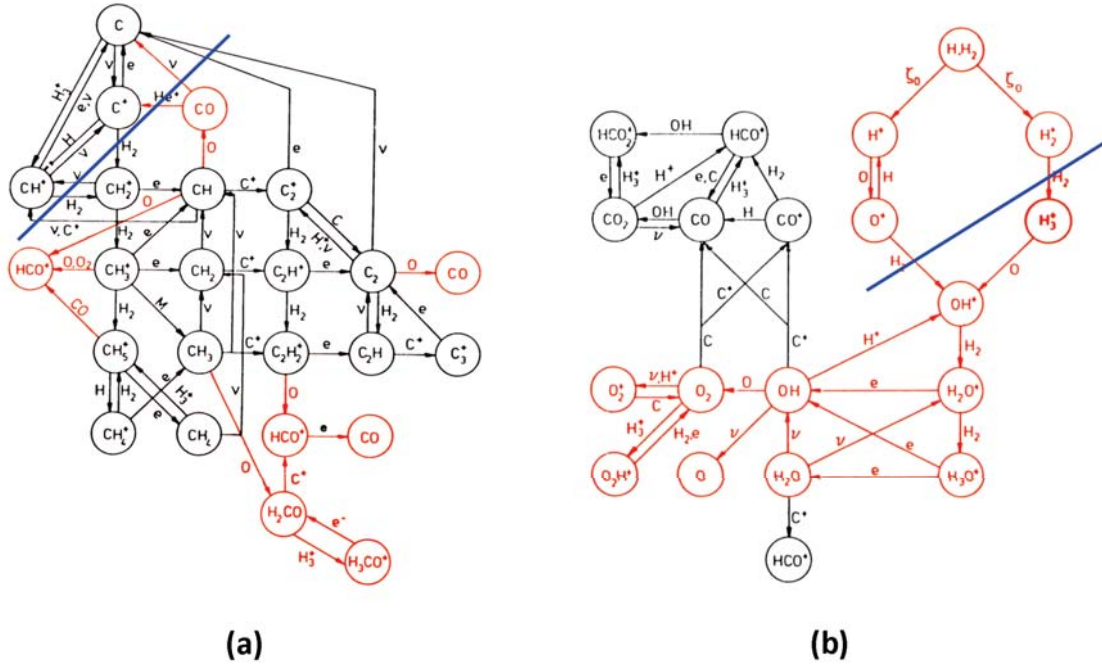


Figure 3.16: Chemical reaction networks for (a) carbon and (b) oxygen in the ISM. The blue line shows the cut-off point where H_2 becomes necessary for further molecular formation either as a catalyst or a reactant. Modified from [1]

the outer parts of the clouds. Lastly H_2 is important for the formation of other molecules in the molecular clouds for both the carbon and oxygen chemistry. This is illustrated in figure 3.16 showing the reaction networks for the oxygen and carbon chemistry in the ISM. The blue line represents the cut-of where H_2 becomes necessary for further molecule formation as either reactant or catalyst. This means that we would not observe the same molecular complexity if not for the H_2 abundance.

Due to the photo dissociation of H_2 , efficient formation routes are needed to explain the observed abundance. The required formation rate in diffuse clouds, $R(H_2)$, can be derived semiempirically using observations of atomic and molecular hydrogen. This yields the following formula [1]

$$R(H_2) = 1 - 3 \times 10^{-17} n n(H) cm^{-3} s^{-1} \quad (3.1)$$

where n is the density of H nuclei and $n(H)$ is the density of H-atoms [2]. The gas phase route is not efficient enough to reach this formation rate, since if two hydrogen atoms collide, they have to lose energy. A radiative transition is strongly forbidden, hence the energy loss can only happen through collision

with a third H-atom. This is, however, too unlikely at the low densities of the ISM to provide a sufficiently efficient reaction route. H₂ can more efficiently be formed through a reaction between the H⁻-ion and an H-atom. This will yield a formation rate a factor of $\sim 10^4$ to low in diffuse clouds, hence still too low to explain the observed abundance [1].

It is generally accepted that grain surfaces work as catalysts for H₂-formation under certain conditions. At low temperatures H-atoms physisorb to the grain surface and diffuse across the surface until they react with each other (Langmuir-Hinselwood reaction). This has been studied experimentally on several surfaces relevant for the ISM; silicates [127] [128] [129] [130], carbonaceous surfaces [131] [132] [133] and water ice [3] [134] [135]. This reaction route, however, only works for low grain temperatures (< 20 K), since at higher temperatures the residence time for a H-atom becomes too short for the Langmuir-Hinselwood mechanism to remain active. By increasing the roughness of the surface, this route might, however, work at slightly higher temperatures [136]. At high gas temperatures ($\gtrsim 1000$ K) H can chemisorb to carbonaceous grains and a secondary incoming H-atom can then react with the chemisorbed H-atom and abstract it as H₂ through Eley-Rideal abstraction [4] [137]. The high temperatures are needed to overcome an adsorption barrier of approx. 200 meV for addition of the first H-atom [138].

An efficient formation route still has to be found at intermediate temperatures. Observations have suggested a correlation between areas of efficient H₂-formation and areas of strong PAH emission in PDRs [5] [139]. Therefore PAHs have been suggested as a possible catalyst for H₂-formation in certain areas. The suggested routes include the superhydrogenation of neutral PAHs and interaction with PAH ions, and are supported by the experiments and calculations discussed in section 3.2. It is, however, still debated whether the PAH route is efficient enough and a recent publication modelling the H₂-formation in two PDRs finds the PAH route to be too inefficient [140]. It is in this context all of the experimental and theoretical investigations discussed in section 3.2, as well as the new results presented in this thesis should be viewed. These investigations provide a greater insight in reaction mechanisms, pathways and cross-sections, which can be used in future models to get a better understanding of H₂-formation and the ISM in general.

Chapter 4

Thermal desorption measurements

In this chapter all of the TPD results obtained during my PhD are discussed. Section 4.1 will look into the thermal desorption of pristine coronene from graphite and the associated desorption kinetics. These results have been published in [49].

The remaining part of the chapter will focus on deuteration of coronene on graphite. Section 4.2 will discuss the evolution of the coronene mass distribution during deuteration. This section contains results published in [141], as well as unpublished work. Section 4.3 will describe how the mass evolution can be compared to kinetic simulations in order to extract reaction cross-sections. These results are published in [141]. Section 4.4 will look into how the interaction between hydrogenated coronene and graphite changes through hydrogenation. These results have been submitted for publication to the Journal of Chemical Physics. Section 4.5 will focus on the hydrogenation of coronene through interaction with hydrogenated graphite. These results are published in [142]

The work presented here was a collaborative effort, with many people involved. The following people were involved in the experimental work: John David Thrower, Pernille Ahlmann Jensen, Frederik Doktor Simonsen, Henri Lemaître, Bjarke Jørgensen and Emil Petersen-Friis. The DFT calculations were carried out by Mie Andersen under supervision of Bjørk Hammer.

4.1 Thermal desorption of coronene

This section gives a brief overview of the TPD measurement of coronene from a highly ordered pyrolytic graphite surface (HOPG; SPI grade 1). Most of this is presented in the article "Interaction between Coronene and Graphite from Temperature-Programmed Desorption and DFT-vdW Calculations: Importance of Entropic Effects and Insights into Graphite Inter-layer Binding." [49]. I took an equal part in collecting the data, as well as analysing it and I commented on the paper prior to publication.

The HOPG substrate was cleaved before it was mounted in the UHV chamber and cleaned by annealing to 1100 K prior to experiments. Coronene (Sigma-Aldrich, sublimed 99%) was deposited using our Knudsen-cell evaporation source at 165°C, while the HOPG was kept at room temperature. The depositions were performed with dosing times ranging from 0.5 s to 3000 s. The sample was heated linearly with a ramp of 1 K s⁻¹, in front of the Extrel CMS LLC QMS.

Figure 4.1 shows TPD traces illustrating the desorption of coronene from graphite. Two desorption peaks are observed one at 360 K and a second at 465 K which are labelled B and A respectively. For exposures up to around 40 s only peak A is present. Peak A is therefore assigned to desorption from the coronene monolayer and the almost constant T_p suggests that the desorption follows first-order kinetics. As the coverage is increased further peak B begins to grow and is therefore attributed to desorption from multilayers of coronene. It should be noted from figure 4.1(a) that the monolayer peak continues to grow even after the observation of multilayer deposition. It should also be noted that the monolayer peak gradually broadens and shifts towards lower temperature (black curves) suggesting a more complicated film growth. There is a pronounced broadening associated with the growth of a shoulder at around 390 K (blue curves). With increasing coverage a clear multilayer peak is visible (red curves). The shoulder is attributed to desorption of islands of a second layer of coronene molecules. This is consistent with the appearance of a multilayer peak prior to saturation of the monolayer. From the high coverage traces (figure 4.1(c)) it is clear that the multilayer peaks share a common leading edge, which is characteristic for zero-order desorption kinetics. The relative coverages shown in figure 4.1 have been obtained by comparing the area under the desorption peaks to that of a saturated monolayer, for which a coverage of 1 ML is defined. A saturated monolayer was prepared by depositing coronene for 60 s and

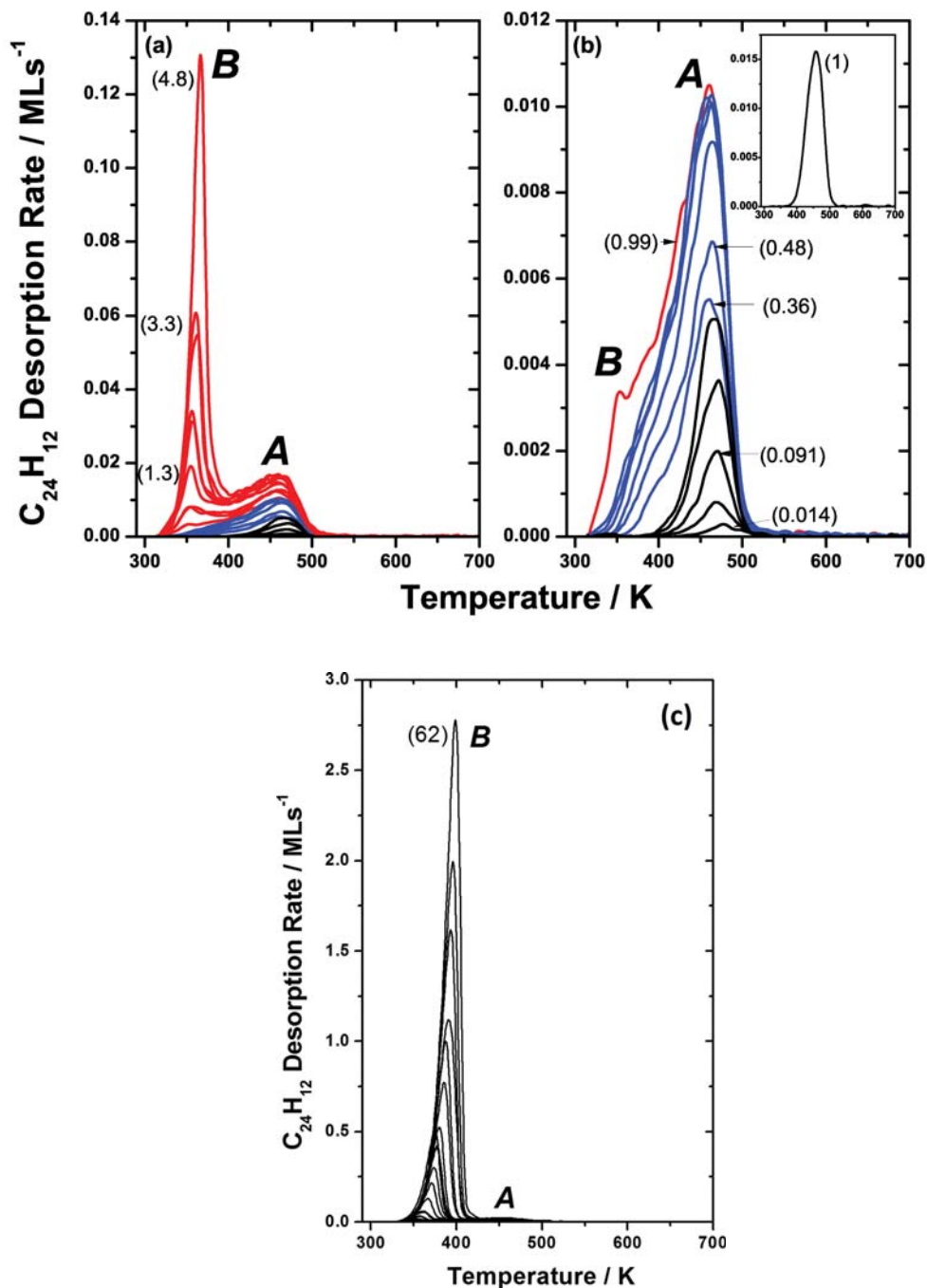


Figure 4.1: TPD spectra for coronene desorbing from graphite for (a) all coverages up to 4.8 ML and (b) coverages from 0.014 to 1 ML. The inset shows a saturated monolayer TPD (c) coverages from 1.3 ML to 62 ML. [49]

then annealing to 390 K to desorb the multilayers. The TPD trace from a saturated monolayer is shown in the inset to figure 4.1(b). That this process in fact creates a saturated monolayer is supported by STM measurements. These measurements are in disagreement with the TPD investigations of coronene from graphite made by Zacharia *et al.* [18] [16] shown in figure 3.3(c). They observed only one peak at around 380 K following fractional order kinetics with $n = 0.27 \pm 0.04$. The monolayer to multilayer transition was attributed to a rather minor change in the leading edge of the desorption traces. The form of their peak closely resembles the peak we assign to the multilayer, suggesting that they only observed multilayer desorption. It should also be noted that, in their study the coronene desorption signal was recorded by observing the pressure rise on the chamber, yielding a much lower detection sensitivity than when using a QMS.

As mentioned in section 2.1.3 several analytical techniques exist for analysis of TPD data. Several methods were tried on the coronene TPDs including the Falconer-Madix analysis [24], the Habenschaden-Küppers analysis [26], the complete analysis [25] and comparison with TPD simulations. These methods yielded values of ν between 10^8 s^{-1} - 10^{13} s^{-1} for the monolayer. These values are considered to be too low and non-physical for such a large molecule; it is expected that it is because of the broadening of the monolayer mentioned earlier. This also means that the corresponding E_{des} found through these analysis methods will be too low due to the compensation effect.

A value for ν can, however, be calculated using transition state theory through formula 2.7. The outer theoretical limits for the pre-exponential factor can be calculated considering the complete mobile and immobile adsorption state. This will yield the values $\nu_{mobile} = 2.8 \cdot 10^{17} \text{ s}^{-1}$ and $\nu_{immobile} = 5.9 \cdot 10^{23} \text{ s}^{-1}$. These calculations are described in greater detail in [49]. This provides the outer theoretical limits for ν . A qualified estimate of the actual pre-exponential factor which describes the desorption kinetics of the monolayer can be made with a recent empirical model based on a large number of experimental studies [143]. There the pre-exponential factor is calculated as:

$$\nu = \frac{k_B T}{h} \exp \left(\frac{S_{gas}^0(T) - S_{gas,1D-trans}^0(T) - S_{ad}^0(T)}{R} \right) \quad (4.1)$$

where S_{gas}^0 is the gas phase entropy, $S_{gas,1D-trans}^0(T)$ is the entropy associated with the translation perpendicular to the surface and $S_{ad}^0(T)$ is the entropy

of the adsorbed state. $S_{gas}^0(465\text{ K})$ can be obtained using tabulated values [144]. $S_{gas,1D-trans}^0(T)$ can be determined from the following formula:

$$S_{gas,1D-trans}^0(T) = \frac{1}{3} \left(S_{Ar,298K}^0 + T \left[\left(\frac{m}{m_{Ar}} \right)^{1/3} \left(\frac{T}{298K} \right)^{5/2} \right] \right) \quad (4.2)$$

where m is the molecular mass of coronene and m_{Ar} is the molecular mass of Ar. If $S_{gas}^0(T) > 60R$, $S_{ad}^0(T)$ can be determined as:

$$S_{ad}^0(T) = S_{gas}^0(T) - 20.7R \quad (4.3)$$

Computing ν based on these equations yields a value of $\nu = 4.8 \cdot 10^{18} \text{ s}^{-1}$.

For multilayer desorption ν can be calculated by assuming a balance between a condensed film in equilibrium with its vapour pressure as [18]:

$$\nu = \frac{sA}{\sqrt{2\pi mk_B T}} p_0 \quad (4.4)$$

where s is the sticking coefficient (taken to be unity), A is the surface area per adsorbed molecule, which can be determined from LEED and STM [53] [54] [55] and p_0 is the vapour pressure at infinity, which can be extrapolated from tabulated data [145]. This will yield a value of $\nu_{mul} = 8.9 \cdot 10^{18} \text{ s}^{-1}$. ν can also be determined experimentally using Arrhenius plots under the assumption of zero-order. This yields $\nu_{mul} = 3.5 \cdot 10^{18} \text{ s}^{-1}$ with a corresponding binding energy of $E_{des} = 1.4 \pm 0.1 \text{ eV}$.

Since the pre-exponential for the multilayer usually yields a reasonable estimate for the monolayer these values gives a quite good estimate for ν for the monolayer. If we now use the Redhead equation the monolayer E_{des} can be determined to be $1.8 \pm 0.1 \text{ eV}$. This is in good agreement with DFT calculations made using the optB88-vFW functional [44], which gave a binding energy of 1.90 eV . The technical details of these calculations will not be discussed in this thesis, but the geometrical considerations will be discussed in the STM measurements chapter.

The determined binding energy can be used to estimate the interlayer binding energy of graphite. The binding energy per C-atom in coronene was from the experiment found to be 75 meV . In order to use this energy to estimate the interlayer binding energy in graphite, one has to adjust for the additional binding energy gain in PAHs due to the interaction between hydrogen atoms in the PAH molecules and graphite. This yields an interlayer

binding energy for graphite of 57 ± 4 meV/C-atom, which is in good agreement with the exfoliation energy of 58 meV/C-atom that can be obtained with the optB88-vdW functional [49].

4.2 Deuteration of coronene

In this section data from deuteration experiments of coronene on graphite are presented. These experiments were carried out with D-atoms created with a hot capillary source heated to approx. 2300 K yielding D-atoms with a gas temperature of 2300 K. Experiments were also performed where a short quartz tube was attached to the source to reduce the gas temperature to approx. 1000 K through collisions. Initial experiments were also performed where a longer quartz tube was used to further reduce the gas temperature to approx. 500 K. The data from the 2300 K atomic D experiments is similar to the previously published data from our group [71] shown in figure 3.8, but of superior quality. This new data was used for comparisons with the kinetic simulations presented in the article "Polycyclic aromatic hydrocarbons - catalysts for molecular hydrogen formation" [141], which will be described in greater detail in section 4.3. The hydrogenation data for 1000 K and 500 K D is still unpublished. I took an equal part in collecting the 2300 K data and took a major part in analysing it. For the 1000 K and 500 K data I designed the experiment, as well as the calibration experiment and I took a major part in collection and analysis.

For all experiments a freshly cleaved HOPG crystal was used, which had been annealed to at least 1100 K prior to experiments. Complete coronene monolayers were then prepared by depositing coronene for 60 s, yielding 2-3 ML, and then subsequently heating the sample to 390 K to remove the multilayers. The sample was then exposed to D for different exposure times.

For the 2300 K D beam, exposure times ranged from 15 s to 10800 s yielding D fluences ranging from $4.3 \cdot 10^{15}$ atoms cm^{-2} to $3.1 \cdot 10^{18}$ atoms cm^{-2} . Figure 4.2 shows an intensity map, representing TPD traces measured for channels ranging from 295 - 365 amu e^{-1} for three different exposures. Since only single ionization is expected amu is used hereafter, rather than amu e^{-1} . Figure 4.2(a) shows the desorption traces for a monolayer of coronene without any exposure to D. Here it is evident that the main peak primarily consists of the parent ion with a mass of 300 amu and $T_p = 465$ K as observed in the previous section. The signal, however, also contains a significant

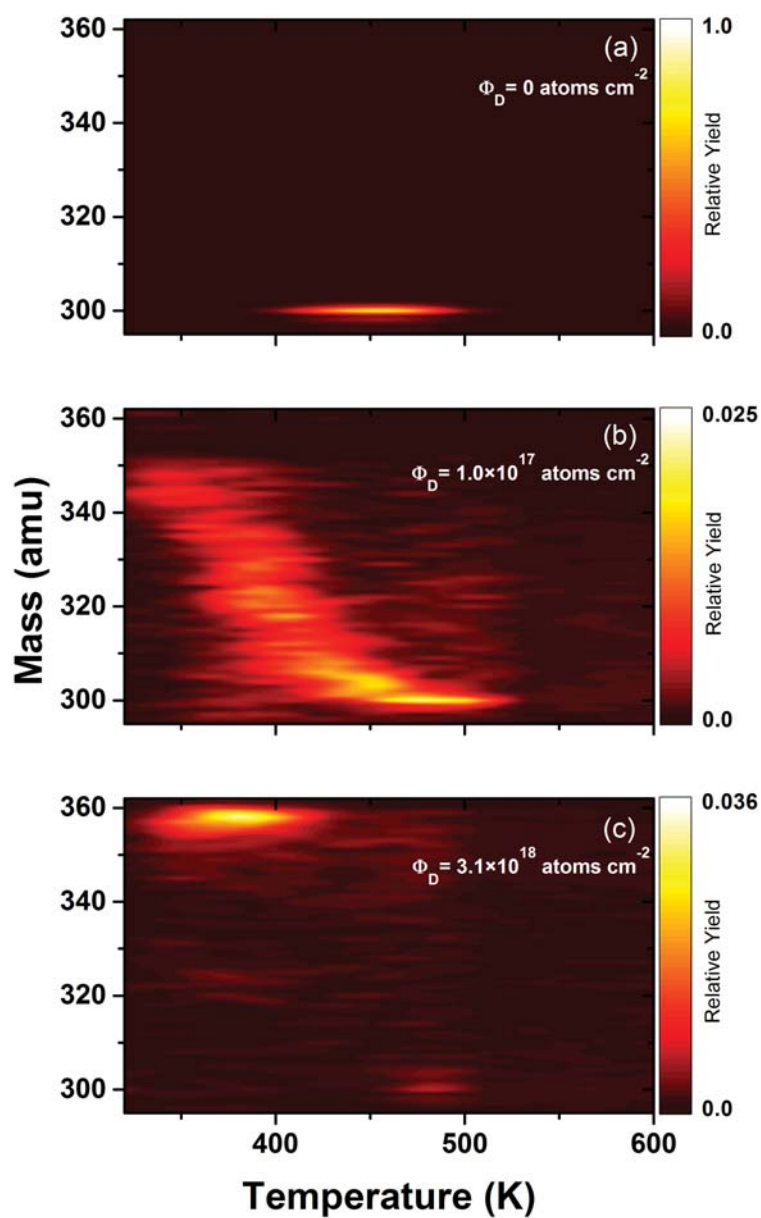


Figure 4.2: TPD traces for masses from 295 - 365 amu for a prepared monolayer of coronene on graphite exposed to different fluences of 2300 K atomic D, Φ_D .

contribution from other channels ranging from 295 - 302 amu. Here the lower mass contribution is attributed to the fragmentation of molecules in the ionization source. The higher masses are due to the natural abundance of ^{13}C of 1.1 %. This will yield a probability of 20.5 %, 2.6 % and 0.2 % for a molecule containing one, two or three ^{13}C -atoms. Two examples of desorption traces after exposure to D-atoms are shown in figures 4.2(b) and 4.2(c). In both cases higher mass species are observed. In figure 4.2(b), desorption traces following exposure to a D-atom fluence of $1.0 \cdot 10^{17}$ atoms cm^{-2} show that the 300 amu peak and T_p remain at 465 K. Higher mass species form a significant fraction of the desorbing molecules and masses as high as 350 amu are observed. The higher mass desorption peaks are observed to shift to lower desorption temperatures and at 348 amu, $T_p = 350$ K. In figure 4.2(c) the desorption traces following exposure to a D-atom fluence of $3.1 \cdot 10^{18}$ atoms cm^{-2} is shown. Here the majority of the desorbing molecules have a mass above 350 amu and masses up to 360 amu are observed. The main peak is located at 358 amu for which $T_p = 376$ K. The reason for the change in T_p is investigated more thoroughly in section 4.4.

In order to investigate the mass evolution further, a series of histograms are plotted in figure 4.3 displaying the mass distribution of desorbing species for several different D fluences. These were obtained by integrating the desorption traces for each mass over the entire temperature range. Initially, before D exposure, primarily a 300 amu signal is obtained, as mentioned earlier. For low D-atom fluences the mass distribution broadens which is illustrated in figure 4.3(b) and (c). For a fluence of $1.40 \cdot 10^{17}$ atoms cm^{-2} the distribution of desorbing species ranges from 300 amu - 350 amu as illustrated in 4.3(c). If the coronene molecules are exposed to even higher D fluences the distribution narrows towards high masses as shown in figure 4.3(d) and (e). For the highest applied fluence of $3.11 \cdot 10^{18}$ atoms cm^{-2} the distribution peaks around 358 amu and masses up to 360 amu are observed corresponding to fully deuterated coronene ($\text{C}_{24}\text{D}_{36}$). These masses can only be obtained if all sites, i.e., outer edge, inner edge and centre sites have been deuterated. Furthermore the H-atoms initially bound to the outer edge carbon atoms have to be exchanged with D-atoms. This is expected to happen through the following reaction scheme (where C represents an outer edge carbon):

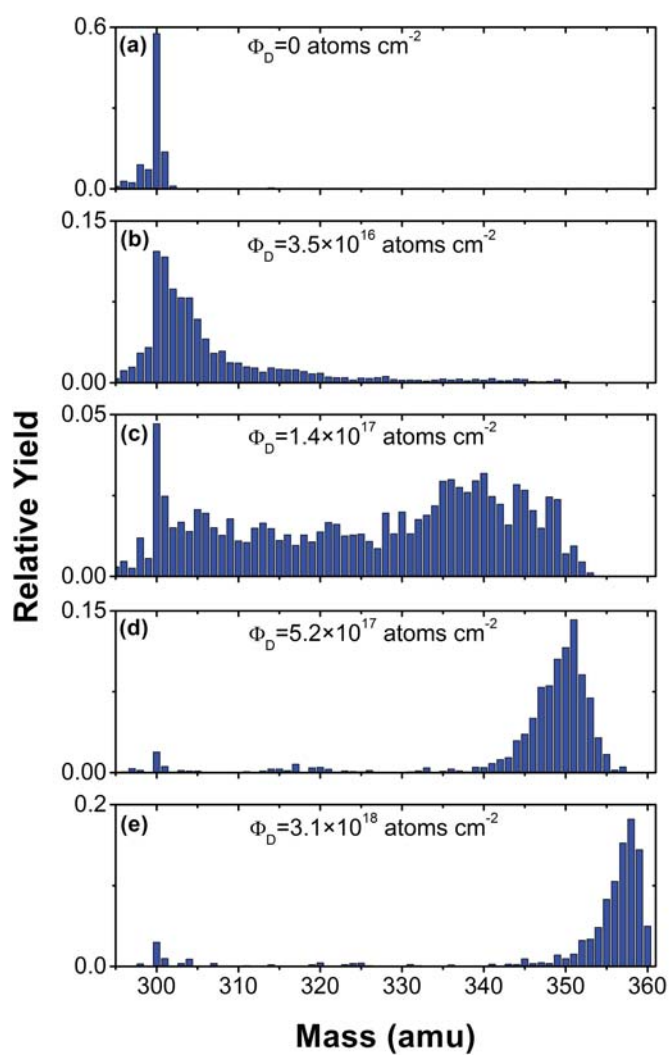
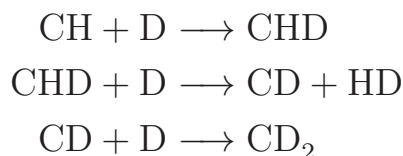


Figure 4.3: Mass distributions for desorbing molecules from a prepared monolayer of coronene on graphite exposed to different fluences of 2300 K atomic D, Φ_D .



This means that our measurements provide indirect evidence that coronene can work as a catalyst for H₂-formation or in this case HD formation. Even for the longest deuterium exposure a small signal still remains at 300 amu. This is attributed to background desorption from the sample mount.

Deuteration experiments using a 1000 K D-beam were also carried out. The reason for lowering the temperature is to use gas temperatures more applicable for the areas of the ISM where PAHs are thought to be important in H₂-formation. The reaction cross-sections will most likely vary with temperature and at this beam temperature deuteration of the graphite does not occur, which might change the reaction pathway. For the 1000 K D beam, exposure times ranging from 60 s to 55000 s were used. A flux of $8 \cdot 10^{13}$ atoms s⁻¹ cm⁻² was determined for the 1000 K D beam through deuteration of Si(100), giving in fluences ranging from $5 \cdot 10^{15}$ atoms cm⁻² to $3.1 \cdot 10^{18}$ atoms cm⁻². Five of the resulting mass distributions can be seen in figure 4.4. The pristine coronene distribution looks the same as for previous measurements and for short dose lengths a broadening of the mass distribution is still observed similar to the 2300 K D-atoms (Fig. 4.4(b) and (c)). However, several smaller peaks are observed in the broad distributions. In figure 4.4(b) these peaks appear at 310, 322, 330 and 336 amu, while in figure figure 4.4(c) they are observed at 308, 338 and 350 amu. For higher fluences the mass distribution narrows into the two high mass peaks initially observed at 338 and 352 amu. These can be seen both in figure 4.4(c) and (d). With increasing dose length the positions of the peaks are observed to shift toward higher masses. The peaks are always the same number of amu apart. The high mass peaks are always approx. 12 amu apart and with increasing dose the highest mass peak increases in intensity, while the lower mass peak decreases. In figure 4.4(e) the low mass peak is completely gone and the high mass peak is peaking at 359 amu with masses up to 361 amu measured. This means that hydrogenation of all sites continues to take place, as do abstraction reactions, when the D beam is cooled and coronene continue to work as a catalyst for HD formation.

The different peaks observed are thought to be related to distinct stable hydrogenation configurations, as was observed for coronene cations by

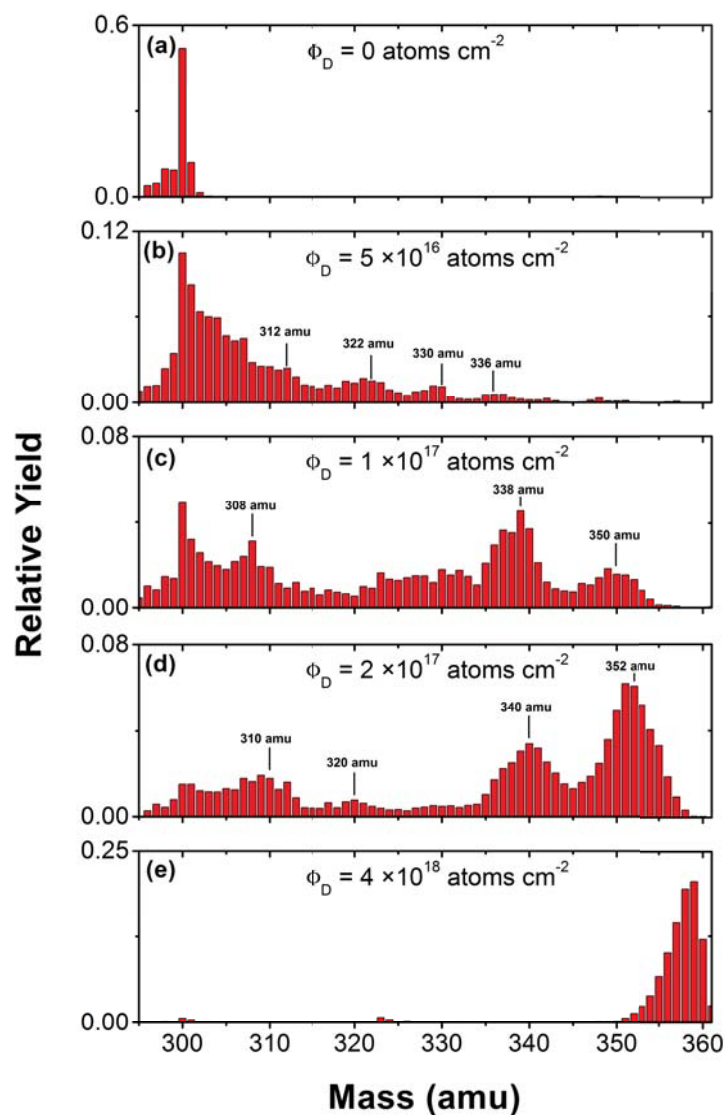


Figure 4.4: Mass distributions for desorbing molecules from a prepared monolayer of coronene on graphite exposed to different fluences of 1000 K atomic D, Φ_D . Some of the significant peaks in the mass distributions are labelled

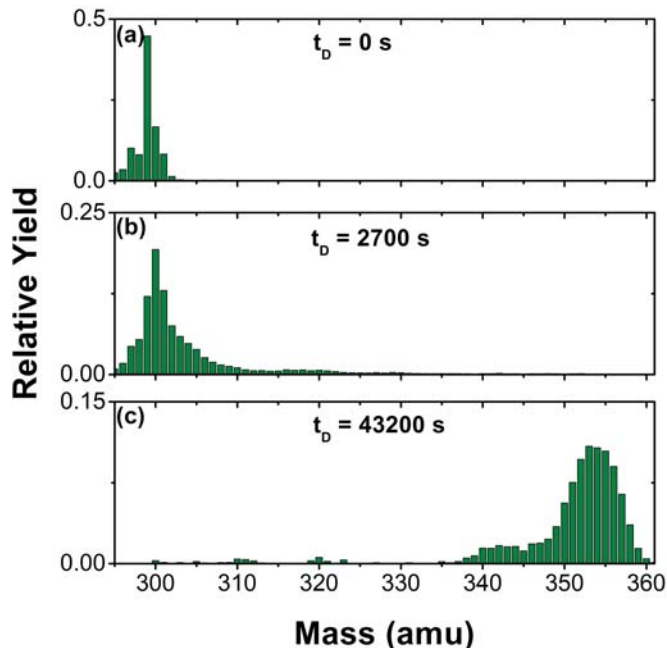


Figure 4.5: Mass distributions for desorbing molecules from a prepared monolayer of coronene on graphite exposed to 500 K atomic D for different exposure times, t_D .

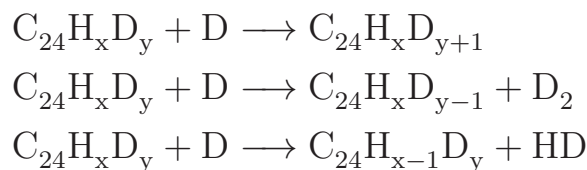
Cazaux *et al.* [89]. We observe, however, a shift of all peaks towards higher masses as a function of fluence, due to the substitution of H with D. This makes it hard to determine the specific stable configurations. However, since the two high mass peaks observed in figure 4.4(c)-(e) are always approx. 12 amu apart, their appearance is expected to be related to the deuteration of centre sites. This suggests that there is a high barrier for the first centre site addition. The high barrier leads to a low reaction probability and the other sites continue to gain and exchange D-atoms, resulting in the build up of the low mass peak. When the first D-atom has been added to the centre ring the π -electron structure of the centre ring weakens resulting in a lowering of the barrier for subsequent additions. The high mass peak then corresponds to a fully deuterated centre ring. This is in disagreement with the DFT calculations on hydrogenation of coronene made by Rauls and Hornekær [65], which showed a zero barrier to centre site for the 6th addition. This was, however, under the assumption that the addition could happen from below the coronene molecule. This might not be possible in the current experiment geometry, since the D-beam is too cold to deuterate the graphite.

This needs to be investigated in more detail. Experiments using an atomic H beam, rather than a D beam, are already planned and will give a greater insight into the stable hydrogenation states of coronene, since a mass change due to H/D substitution does not take place.

Initial measurements were also made with 500 K D-atoms yielding the mass distributions seen in figure 4.5. Here masses above 348 amu are also observed, meaning that all types of sites are hydrogenated and that abstraction takes place. Further more the double peak structure at high masses is also observed in figure 4.5(c).

4.3 Kinetic simulations of the deuteration of coronene

This section shows how kinetic simulations can be used to extract reaction cross-sections from the experimentally measured mass distributions showed in the previous section. This work is published in the paper "Polycyclic aromatic hydrocarbons - catalysts for molecular hydrogen formation" [141]. The algorithm used for kinetic simulations was created in MatLab by me and I wrote the majority of the paper. In the simulation, the molecular distribution was evaluated through a series of time steps. For each time step three possible reactions can happen:



where the first reaction is an addition reaction and the two others are abstraction reactions, whereby an incoming D-atom abstracts a D- or H-atom as D₂ or HD respectively. This means that the algorithm is not site specific, hence it does not distinguish between outer edge, inner edge and centre sites. The rate of an addition reaction involving a hydrogenated coronene molecule with n excess H/D-atoms was determined by the D-atom flux, ϕ_D and an addition cross-section, $\sigma_{add}(n)$, dependent on the degree of hydrogenation. Since the cross-section for addition was treated as being only dependent on the number of excess H/D-atoms on the molecule it is in essence an average over additions onto all available sites of all possible conformers of the hydrogenated coronene for a given degree of hydrogenation. The cross-section for

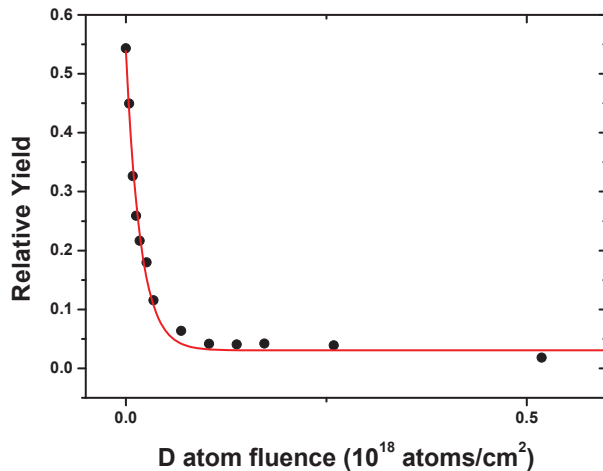


Figure 4.6: Relative yield of the coronene 300 amu signal as a function of D-atom fluence (black dots). The decay can be fitted by a single exponential decay function (red curve).

the first addition, $\sigma_{add}(0)$, can be determined by plotting the relative yield of the 300 amu signal as a function of the D fluence as seen in figure 4.6 (black dots). $\sigma_{add}(0)$ can then be determined by fitting an exponential decay

$$I_{300} = I_0 \exp(-\Phi_D \sigma_{add}(0)) + I_\infty \quad (4.5)$$

where I_{300} is the relative yield, I_0 is the initial relative yield and I_∞ is the relative yield at infinity. The fit is also shown in figure 4.6 (red line). The best fit for the decay gives a cross-section for the first D-atom addition of $\sigma_{add}(0) = 0.55 \pm 0.03 \text{ \AA}^2$.

For $n > 0$, $\sigma_{add}(n)$ was treated as a variable parameter. The rate of abstraction scales linearly with the ϕ_D , n , and the abstraction cross-section, $\sigma_{abs}(n)$, for each excess H/D-atom. Abstraction was not allowed for $n = 0$, so the molecules will always have at least 12 H/D-atoms. The cross-section for both H and D were taken to be equal. For each simulated time step, the corresponding final mass distribution was evaluated. The molecular distributions were modifying to reflect the correct $^{13}\text{C} : ^{12}\text{C}$ ratio and by including fragmentation in the mass spectrometer ionization process. Since the fragmentation pattern of the superhydrogenated species is unknown it was assumed to be the same as for pristine coronene. This might not be a completely valid assumption, since the deuterated species most likely are more unstable and therefore more prone to fragmentation. For pristine coronene

	Simulation 1	Simulation 2	Simulation 3
σ_{abs} per site	0.06	0.01	0.01
$\sigma_{\text{add}}(0)$	0.55	0.55	0.55
$\sigma_{\text{add}}(1)$	0.55	0.55	3.45
$\sigma_{\text{add}}(2)$	0.55	0.55	3.30
$\sigma_{\text{add}}(3)$	1.00	1.00	3.15
$\sigma_{\text{add}}(4)$	2.50	2.00	3.00
$\sigma_{\text{add}}(5)$	2.50	2.00	2.85
$\sigma_{\text{add}}(6)$	2.50	2.00	2.70
$\sigma_{\text{add}}(7)$	2.50	2.00	2.55
$\sigma_{\text{add}}(8)$	2.50	2.00	2.40
$\sigma_{\text{add}}(9)$	2.50	2.00	2.25
$\sigma_{\text{add}}(10)$	2.50	2.00	2.10
$\sigma_{\text{add}}(11)$	2.50	2.00	1.95
$\sigma_{\text{add}}(12)$	2.50	2.00	1.80
$\sigma_{\text{add}}(13)$	2.50	2.00	1.65
$\sigma_{\text{add}}(14)$	2.50	2.00	1.50
$\sigma_{\text{add}}(15)$	2.50	2.00	1.35
$\sigma_{\text{add}}(16)$	2.50	2.00	1.20
$\sigma_{\text{add}}(17)$	2.50	2.00	1.05
$\sigma_{\text{add}}(18)$	1.30	1.00	0.90
$\sigma_{\text{add}}(19)$	1.30	1.00	0.75
$\sigma_{\text{add}}(20)$	1.30	1.00	0.60
$\sigma_{\text{add}}(21)$	1.30	1.00	0.45
$\sigma_{\text{add}}(22)$	1.30	1.00	0.30
$\sigma_{\text{add}}(23)$	1.30	1.00	0.15

Table 4.1: Abstraction (σ_{abs}) and addition (σ_{add}) cross-sections used in the simulations presented in this section. All values are in units of \AA^2 . [141]

the probability of losing 1 H/D-atom is 7.5%, 2 H/D-atoms is 9.7%, 3 H/D-atoms is 2.8% and 4-5 H/D-atoms is less than 1%.

Several sets of cross-sections were tried both for addition and abstraction reactions. Three sets of cross-sections have been picked out and are listed in table 4.1. In simulation 1 $\sigma_{\text{abs}}/n = 0.06 \text{ \AA}^2$, which is an experimentally determined value found by Mennella *et al.* [74] for a 300 K D beam. The $\sigma_{\text{add}}(n)$ used were then the ones yielding the best fit with this σ_{abs}/n . The corresponding evolution in the mass abundances are plotted relative to D-atom fluence for the masses 300 amu, 320 amu, 340 amu, 350 amu and 355 amu as the blue curve in figure 4.7(a), (b), (c), (d) and (e) respectively. The corresponding experimental values are plotted in figure 4.7 as black dots. It can be seen that this model reproduces the experiment well at low masses, but fails for the high masses. In simulation 2 σ_{abs}/n was reduced to 0.01 \AA^2 where the best fit was found. The corresponding mass evolutions are plotted

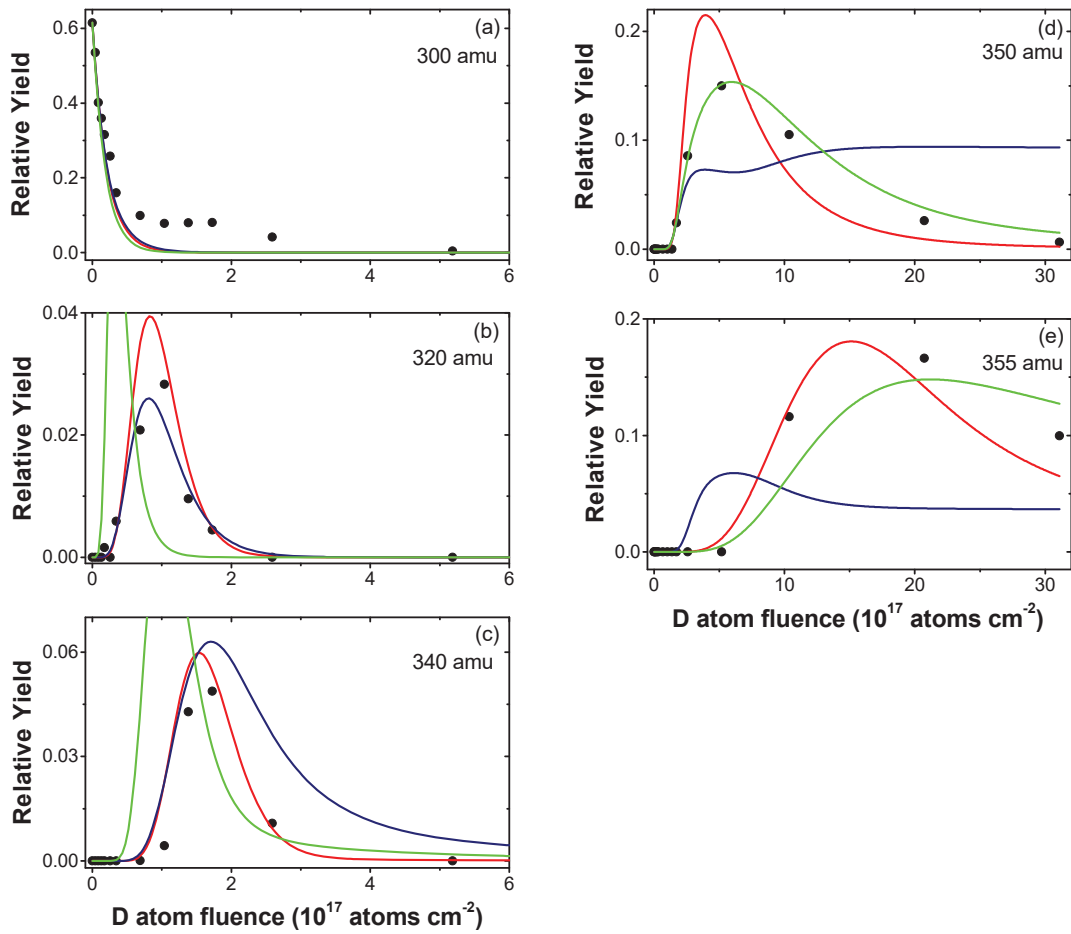


Figure 4.7: Evolution in the abundance of (a) mass 300 amu, (b) 320 amu, (c) 340 amu, (d) 350 amu and (e) 355 amu as a function of D-atom fluence. Black dots are the experimental data, blue curves are simulation 1, red curves are simulation 2, while green curves are simulation 3. [141]

in figure 4.7 as the red curve. This model replicates the experimental data reasonably well for all masses. A model was also tried where $\sigma_{add}(n)$ was set to be dependant on the available sites for additions hence $\sigma_{add}(n) = (24 - n) \times 0.15 \text{ \AA}^2$ (simulations 3). This model is plotted in figure 4.7 as green lines and can only reproduce the experimental data at high masses, but fails at low masses.

The mass distributions found through simulation 2 have also been plotted (in grey) together with 5 different experimental mass distributions (in black) in figure 4.8. Here it should be noted that this model in general resembles the experimental data very well for most masses, but it has a few problems for the lowest fluences. Non-hydrogenated coronene is experimentally observed in higher quantities, than expected from the model. This can partly be explained by coronene desorbing from the sample holder, where it is not as easily hydrogenated.

The cross-section is small for the first addition reactions as seen in the second column of table 4.1. This is consistent with the barrier of 60 meV predicted by DFT [65]. These calculations suggested a reduced energy barrier for additions on the neighbouring sites, however the majority of the addition sites will still have high barriers resulting in an overall small cross-section, as observed. The $\sigma_{add}(n)$ suggested for the intermediate masses is generally independent of the available sites for addition. This may indicate that the incoming D-atoms are mobile on the coronene molecule and are able to scan the molecule for available addition sites. Similar behaviour has been observed for the hydrogenation of graphite [146]. The odd-even variation predicted by the simulations are generally not observed in the experimental data. This could be related to differences in fragmentation patterns for the deuterated molecules or because of reactions with atomic H created from H₂ contamination in the gas line.

The more complex structure of the mass distribution of the coronene hydrogenated with 1000 K D-atoms can not be reproduced by this simple simulation algorithm. This is probably due to the lack of site specificity in the algorithm. A site specific kinetic simulation algorithm is however under development together with one of our collaborators, Herma Cuppen from Nijmegen, Netherlands.

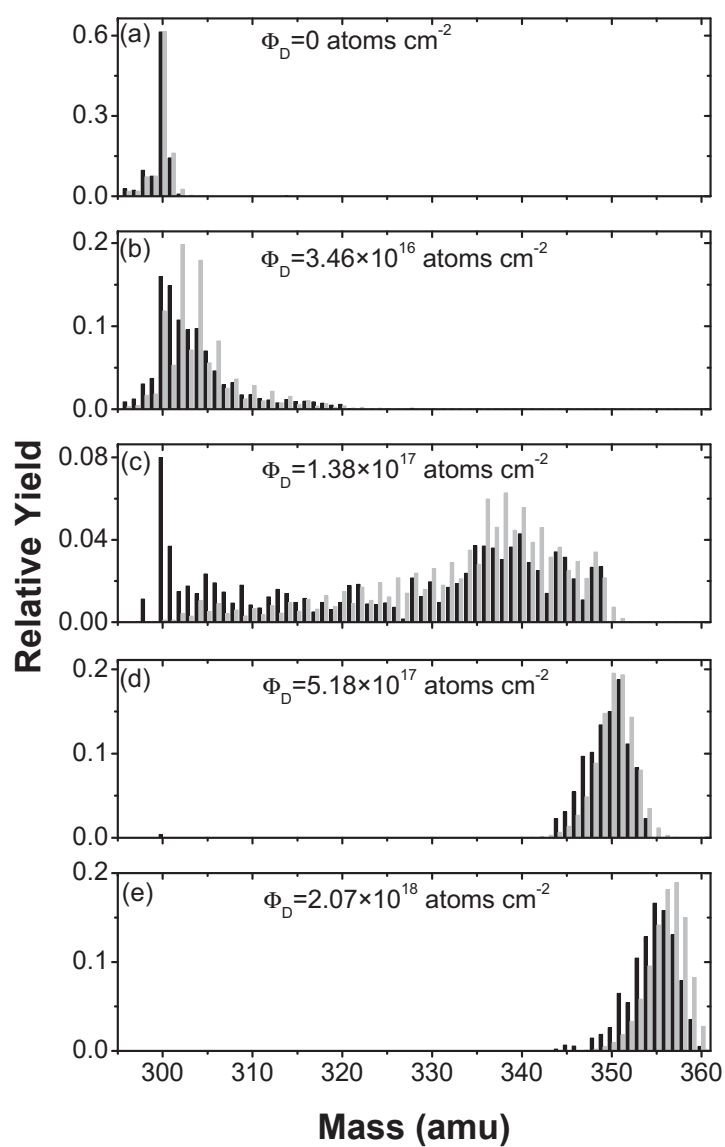


Figure 4.8: Experimental (black) and simulated (grey) mass distributions for simulation 2. [141]

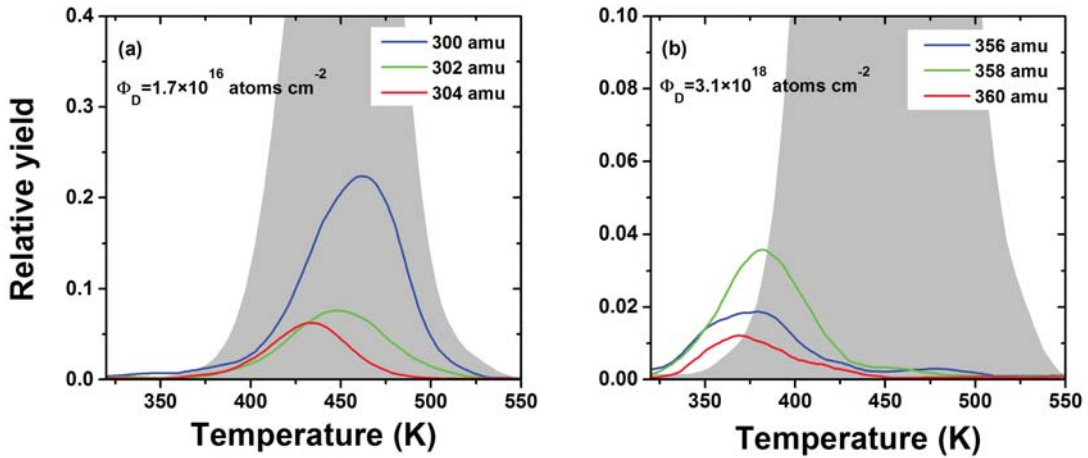


Figure 4.9: The three most significant even massed TPD traces after exposure to atomic D plotted together with the TPD trace from a pristine coronene monolayer (grey area). (a) Shows the TPD traces after exposure to an atomic D fluence of $1.7 \cdot 10^{16} \text{ atoms cm}^{-2}$ and (b) to an atomic D fluence of $3.1 \cdot 10^{18} \text{ atoms cm}^{-2}$.

4.4 The coronene-graphite interaction during deuteration

In this section data on the change in E_{des} resulting from deuteration of coronene is presented. The results presented here are based on analysis of the 2300 K D data presented in section 4.2. These results have been submitted for publication to Journal of Chemical Physics. I carried out the analysis and wrote the majority of the paper.

Examples of the three most significant even mass desorption traces for two different fluences of 2300 K D are shown in figure 4.9 together with the 300 amu trace from a pristine monolayer plotted in grey. In figure 4.9(a) the three largest even mass desorption traces for a short D dose with a fluence of $1.7 \cdot 10^{16} \text{ atoms cm}^{-2}$ are illustrated. The blue curve is the desorption trace for 300 amu and the T_p remains at 465 K. The green and red curves are for 302 amu and 304 amu respectively corresponding to single and double deuterated coronene molecules. Already here a decrease in T_p is observed with $T_p = 448 \text{ K}$ for 302 amu and $T_p = 432 \text{ K}$ for 304 amu. In figure 4.9(b) the three largest even mass desorption traces for a long D dose with a fluence of $3.1 \cdot 10^{18} \text{ atoms cm}^{-2}$ are illustrated. The blue, green and red curves are for 356 amu, 358 amu and 360 amu and all show a lower T_p compared to the

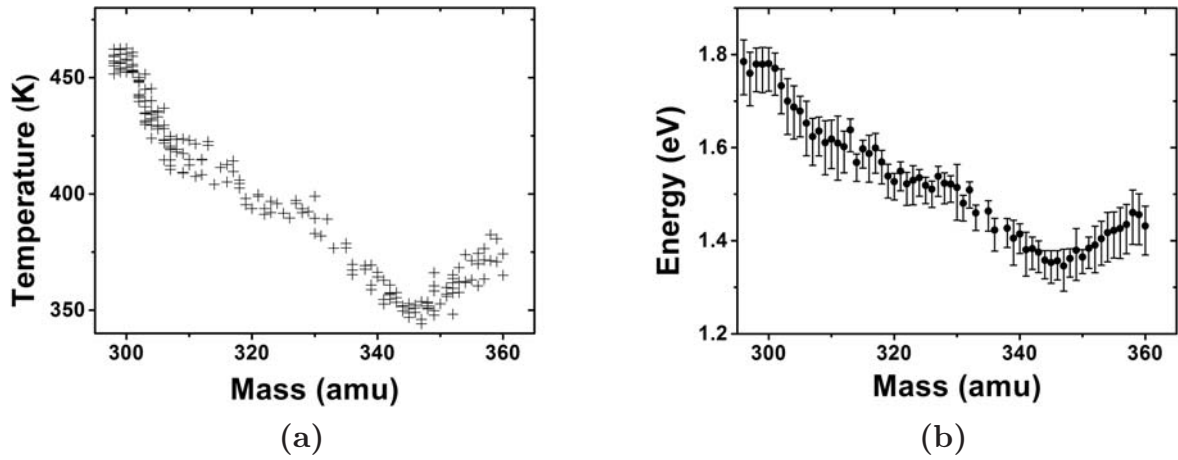


Figure 4.10: (a) T_p found for the most significant desorption peaks for 16 different fluences of 2300 K D-atoms, plotted relative to mass. (b) E_{des} found from the T_p shown (a), plotted relative to mass

300 amu peak. It is also worth noticing that even the largest peaks are more than 20 times smaller than the 300 amu peak from the pristine coronene film for the long D dose. This is partly due to the broader distribution of molecules and partly due to a loss of molecules during hydrogenation. A loss of up to 75 % of molecules during deuteration has previously been observed, when hydrogenating with a 2300 K D beam [141]. It is also worth noticing that the TPDs appear to still exhibit first-order kinetics, hence the Redhead equation can be used to determine E_{des} for the desorbing molecules.

In order to determine E_{des} over the whole mass range T_p has been determined for the observed desorption peaks for 16 different fluences of 2300 K D-atoms. The resulting temperatures are plotted relative to mass in figure 4.10(a). It is assumed that ν is between $8.9 \cdot 10^{17} \text{ s}^{-1}$ and $4.8 \cdot 10^{18} \text{ s}^{-1}$ as determined for pristine coronene mentioned in section 4.1 and $\nu = 2.9 \cdot 10^{18} \text{ s}^{-1}$ has been used to determine the binding energies. The resulting binding energies are plotted relative to mass in figure 4.10(b). Initially E_{des} decreases very rapidly with mass from 1.78 eV for non-deuterated coronene to 1.55 eV at 318 amu. After this E_{des} decreases to a minimum 1.34 eV at 347 amu and then increases to 1.43 eV at 360 amu. This general decrease in E_{des} is expected and attributed to the removal of π -electrons from the π -electron system through the conversion of the carbon hybridisation from sp^2 to sp^3 , as well as the simultaneous buckling of the molecule predicted

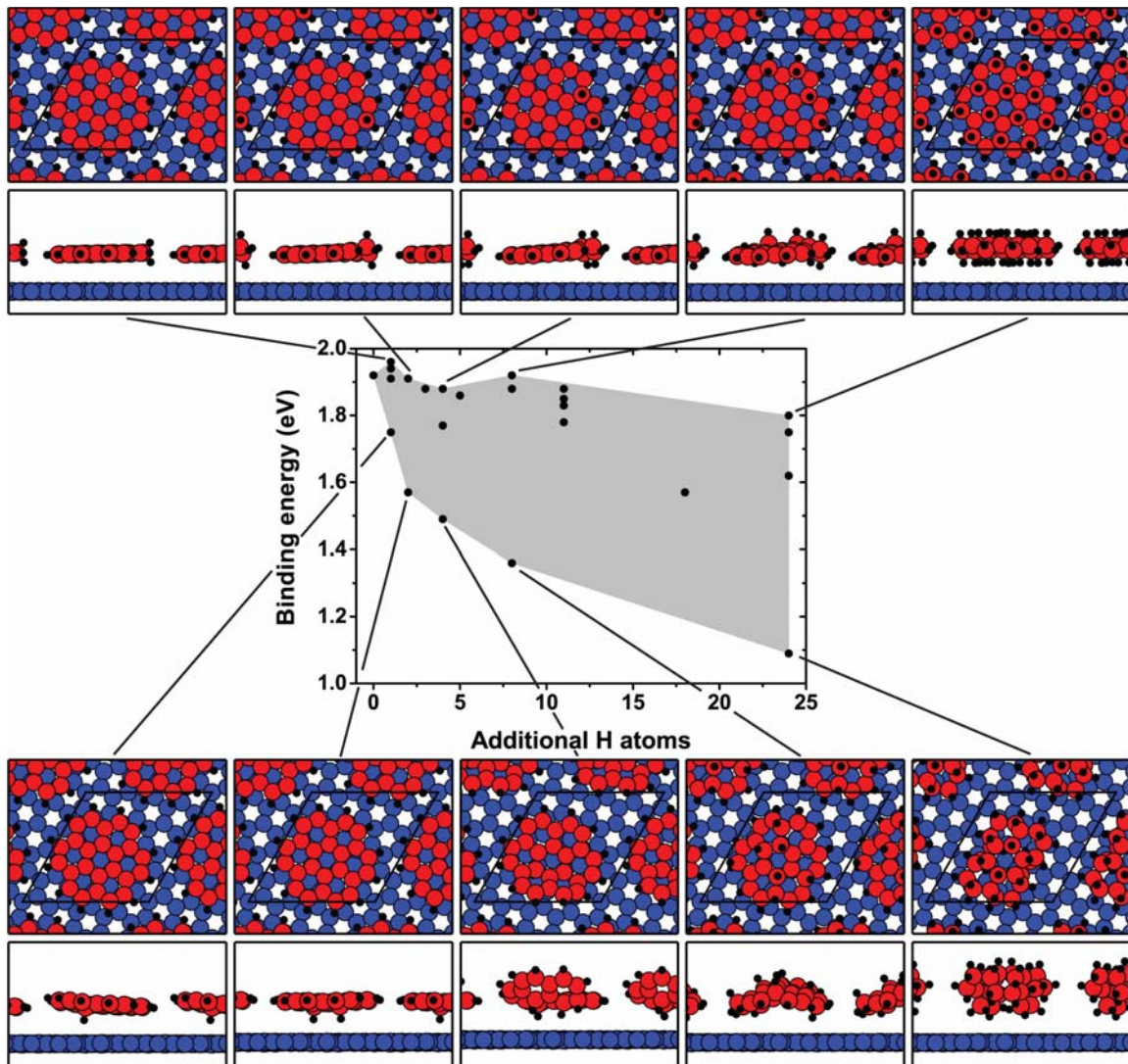


Figure 4.11: DFT calculations of the binding energy for several different conformations of hydrogenated coronene plotted relative to the number of additional H-atoms. The conformations promoting the least amount of buckling are shown at the top and conformations promoting the most amount of buckling are shown at the bottom. The grey area shows the range within which the DFT calculations predict the binding energy should be.

by DFT calculations [71].

DFT calculations on the binding energy of several different configurations of hydrogenated coronene have been carried out by Mie Andersen. The calculations were performed using the optB88-vDW functional [44] in a similar manner to those concerning pristine coronene on graphite [49]. The resulting energies are plotted as dots relative to the number of additional

H-atoms attached in figure 4.11. Each hydrogenation state can be realized in different configurations, which all contain the same number of H-atoms, but differ from each other with respect to the positions of the H-atoms. The binding energy has been determined for 25 different configurations covering 10 different degrees of hydrogenation. 10 of these configurations are illustrated in figure 4.11. The grey area marks the boundaries of the calculation. That is the grey area covers the binding energy of all possible hydrogenated coronene molecules according to the DFT calculations. The details of all of the individual configurations will not be discussed here. It is, however, worth noting that the highest binding energies are those that promote the least amount of buckling. For 24 additional H-atoms this occurs for coronene that is equally hydrogenated on both sides of the molecule, i.e. fully trans-hydrogenated coronene. These configurations are shown at the top of figure 4.11. The lowest binding energies are on the other hand generally the ones that promote the most buckling of the molecule, which for 24 additional H-atoms is for completely single sided hydrogenation, i.e. fully cis-hydrogenated coronene. For up to 4 additional H-atoms the lowest binding energy is, however, achieved through hydrogenation of centre sites on the bottom side of the molecules, i.e. with the adsorbed H-atom sitting between the coronene carbon skeleton and the graphite. The lowest energy configurations are shown in the bottom of figure 4.11. The reduction of the π -electron system only results in a minor decrease in binding energy, since the fully trans-hydrogenated coronene has a binding energy of 1.80 eV, compared to 1.90 eV for ordinary coronene. The buckling on the other hand seems to result in a much larger decrease since the fully cis-hydrogenated coronene has a binding energy of 1.09 eV.

When comparing the experimental data to the DFT calculations, several problems occur. The DFT calculations, for non-hydrogenated coronene, yields a binding energy which is 0.14 eV higher than that observed experimentally. Furthermore due to the exchange of H and D, the predicted calculated desorption energies for a given hydrogenation state can cover up to 13 amu, since the amount of H exchanged to D is unknown. In other words the binding energy of a given hydrogenation state n can apply to all the molecules described by the formula $C_{24}H_{12-i}D_{n+i}$, where $i = 0 - 12$ and describes the number of H exchanged with D. In order to overcome these differences and compare the trend of the DFT with that found in the experimental data, 0.14 eV has been subtracted from all the values found through DFT calculations and all possible molecular species have been taken into

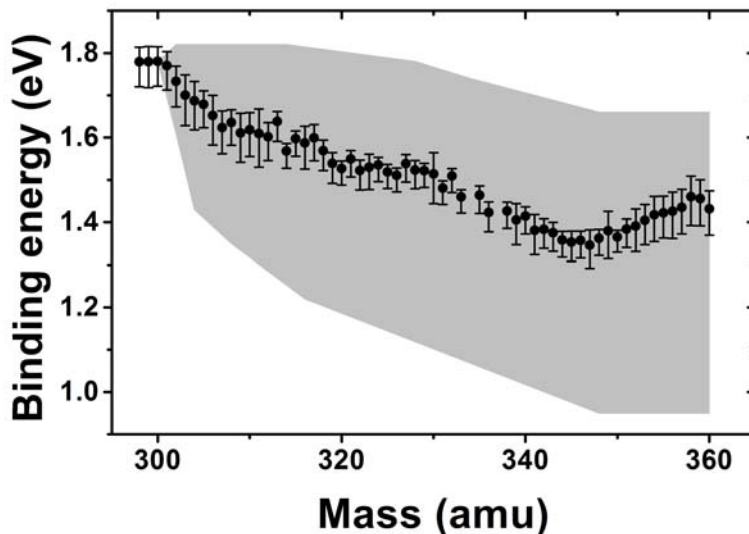


Figure 4.12: The grey area shows the range within which the DFT calculations predict the binding energy should be, after subtracting 0.14 eV and taking all molecular species for each hydrogenation state into account. The experimentally found values are plotted in black.

account for each hydrogenation state. These two corrections result in the light grey area plotted in figure 4.12 as the possible energies predicted by the DFT calculation. The experimentally determined binding energies are plotted in figure 4.12 as well. The decrease in energy observed from 301 - 310 amu lies below what can be achieved through hydrogenation from the top. Even for the configuration yielding the maximum amount of buckling, i.e. centre side addition. For these masses only bottom side hydrogenation of centre sides yields low enough binding energies. This is contradictory to DFT calculations [65] and the expected addition path for 1000 K D-atoms described in section 4.2. However, the 2300 K D beam has sufficient energy to deuterate the graphite, hence the additions might rely on surface abstraction instead of gas phase impingement, as will be described in section 4.5. For the higher masses the binding energies suggest a combination of single sided and double sided hydrogenation since the values lie between the cis- and trans-hydrogenation limit. The increase in binding energy from 347 amu to 360 amu could suggest a decrease in the buckling of the molecule occurring through the final deuterium addition reactions.

4.5 Coronene deuteration through interaction with deuterated graphite

This section will discuss how coronene can be deuterated through interaction with graphite that has already been deuterated. These results have been published in the paper "Hydrogenation of PAH molecules through interaction with hydrogenated carbonaceous grains" [142]. I only took a minor part in collecting this data and analysing it. I commented on the paper prior to publication.

For all experiments a freshly cleaved HOPG crystal was used, which had been annealed to at least 1200 K prior to experiments. D-atoms were dosed with the hot capillary source held at 2000 K and coronene was deposited with the Knudsen-cell evaporation source held at 180°C. Graphite was deuterated by exposing it to the bare hot capillary source. A typical TPD spectrum of D₂ from graphite is shown in figure 4.13(a), labelled 0 s. The TPD trace shows two distinct desorption peaks at 490 K and 580 K respectively in agreement with the literature [137]. These peaks follow first-order kinetics and have been shown to come from recombination of pre paired dimers [4]. The TPD trace in figure 4.13(a) (0 s) results from a graphite saturated with atomic D, leading to a saturation coverage of 0.4 ± 0.2 [137]. The other TPD traces in figure 4.13(a) are from graphite exposed to coronene for the labelled amount of time and subsequently exposed to an atomic D fluence corresponding to the saturation fluence. There is a dramatic decrease in the D₂ signal and after 6 s of coronene exposure the signal is almost completely suppressed.

TPD measurements of coronene desorbing from graphite indicate that a 40 s coronene dose is needed to completely cover the graphite surface with molecules. The D₂ signal, however, decreases rapidly with coronene exposure and 25 % of a monolayer is enough to completely suppress the signal, as shown in figure 4.13(b) (filled circles). This suggests that the coronene molecules can scan the surface and react with the D adsorbed to the graphite surface. That coronene is mobile on the surface is consistent with the pre-exponential factor found in section 4.1, which was close to the mobile limit predicted by transition state theory [49]. This is also supported by DFT calculations [49] and STM [55]. If the dose is reversed, hence the sample is saturated with atomic D and then coronene is deposited, the picture is the same, as seen in 4.13(b) (open circles). Here the D₂ signal is also completely suppressed for doses with a coverage of less than half a

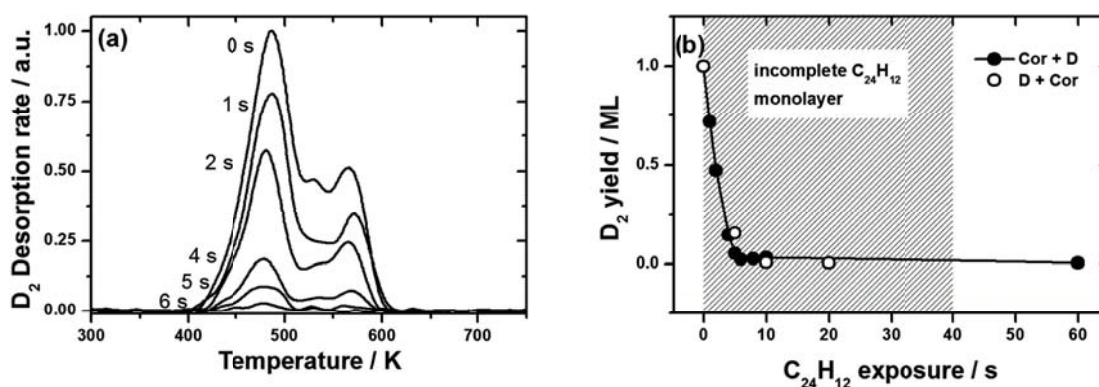


Figure 4.13: (a) TPD traces for the desorption of D₂ from 0, 1, 2, 4, 5 and 6 s exposures of coronene on HOPG subsequently exposed to a D-atom fluence sufficient to saturate the clean graphite. (b) Decay of the D₂ desorption yield corresponding to the data in (a) (filled circles) and for the reverse system where the HOPG was first exposed to a saturation D-atom dose followed by coronene (open circles). [142]

monolayer of coronene.

That the coronene in fact reacts with the adsorbed D can be confirmed by measuring the masses of the desorbing coronene species after the reverse dose. The result is shown in figure 4.14. Figure 4.14(a) shows the mass distribution for a pristine coronene monolayer, while figure 4.14(b)-(e) shows the desorption of coronene species from graphite saturated with D after exposure to different amounts of coronene. For the 5 s coronene dose it is clear that the coronene does in fact react with the pre adsorbed D. There is a clear reduction of the 300 amu signal, corresponding to pristine coronene, and superdeuterated species with masses up to at least 340 amu are detected. This corresponds to addition of up to 20 D-atoms. For longer coronene doses the signal seems to be dominated by species with a lower degree of hydrogenation, however masses up to 340 amu can be observed.

We can now consider the number of D-atoms available for reaction. Since the amount of available sites for deuteration, as well as the saturation coverage [137] is known, the amount of available D-atoms can be calculated as $(1.5 \pm 0.8) \cdot 10^{15} \text{ cm}^{-2}$. For a monolayer of coronene on graphite it is known that a $\sqrt{21} \times \sqrt{21} \text{ R} \pm 10.9^\circ$ superstructure is formed [49] [53] [54] [55]. This gives a coronene surface density of $8.4 \cdot 10^{13} \text{ cm}^{-2}$, meaning that 17 ± 9 D-atoms should be attached to each coronene molecule on average if all D-atoms were to react. This means that the average mass of the coronene

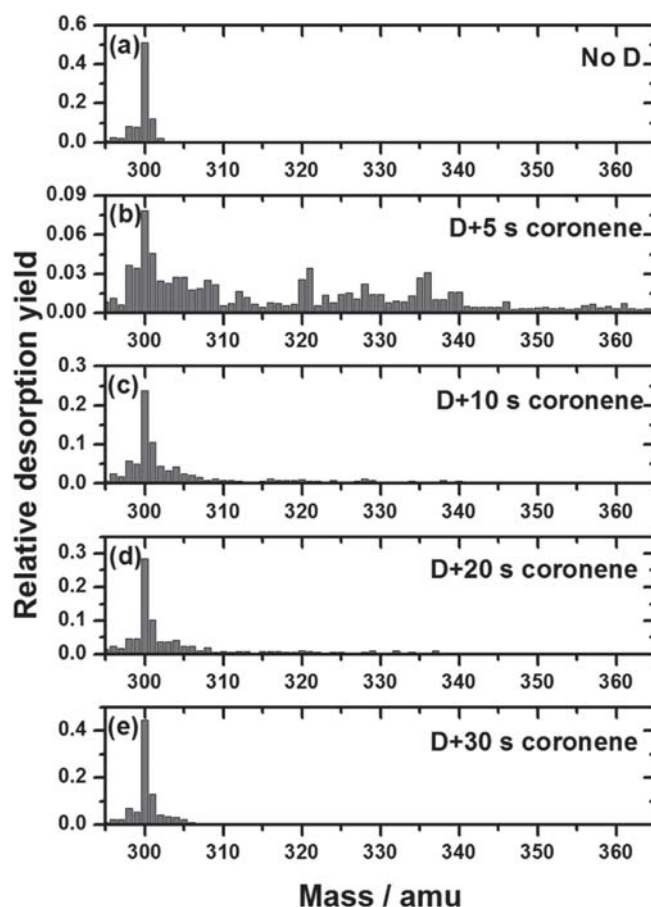


Figure 4.14: Mass distributions for desorbing coronene species obtained for (a) coronene adsorbed on a non-deuterated graphite surface and following exposure of a D-atom saturated graphite surface to coronene exposures of (b) 5, (c) 10, (d) 20 and (e) 30 s. [142]

molecules desorbing from a complete monolayer deposited on a D covered surface should be 332 ± 18 amu. This is clearly not the case for any of the mass distributions shown in figure 4.14, even for the 5 s dose where the coronene coverage is close to 0.1 ML. This suggest that D-atoms are "lost" in the reaction.

The coronene dose times of 5, 10, 20 and 30 s can be recalculated to coverages of 0.09, 0.42, 0.54 and 0.85 ML respectively. Based on this and the mass distributions shown in figure 4.14, together with D_2 detected directly from the surface (figure 4.13), the fraction D-atoms accounted for can be estimated. The estimated fraction of detected/available D-atoms have been plotted as a function of coronene exposure time (open circles) in figure 4.15. The coronene coverages have also been plotted here (filled circles). The

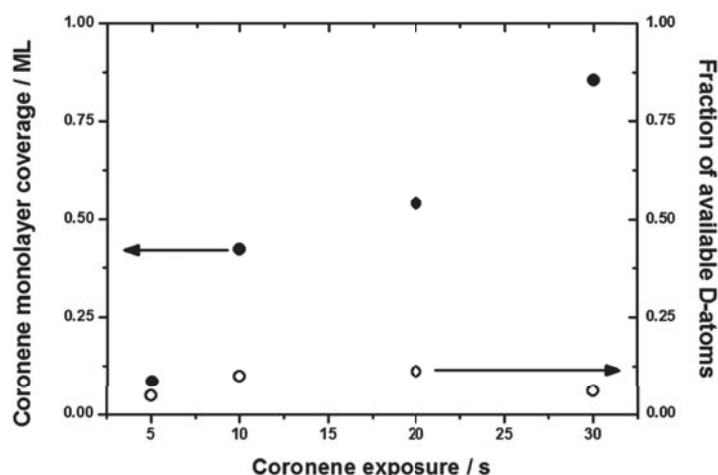


Figure 4.15: Growth of the coronene monolayer (filled circles) and the fraction of available D-atoms present in detected superhydrogenated species (open circles) as a function of increasing coronene exposure. [142]

fraction of detected D-atoms remains almost constant at $8 \pm 3 \%$, meaning that around 90 % of the D-atoms are "lost".

DFT calculations suggest, as mentioned earlier, that the barrier for addition and abstraction of H/D to coronene after the first addition is small or zero [65]. Since addition is clearly observed, we suggest that the "loss" of D-atoms is due to the abstraction of H/D and thereby release of HD/D₂. This suggest that PAHs can facilitate desorption of H₂/HD/D₂ even below the minimum desorption temperature. However because of the heating needed for TPD measurements it is not possible to determine at which temperature the reactions starts to occur. Coronene is, however, expected to be mobile on graphite down to even 100 K [49] and smaller PAHs will be mobile at even lower temperatures.

4.6 Conclusion

In summary we have shown that TPD spectra from coronene on graphite show two distinct desorption peaks; one peaking at 465 K attributed to the monolayer and one continuously growing peak at lower temperature attributed to the multilayer. The monolayer peak follows first-order kinetics and E_{des} was determined to be 1.8 ± 0.1 eV in good agreement with DFT calculations executed using the opt-B88 functional and yielding 1.90 eV. The multilayer was found to follow zero-order kinetics and E_{des} was determined

to be 1.4 ± 0.1 eV. These measurements improve on the previous accuracy of TPD measurements [18].

When the coronene monolayer gets exposed to atomic D masses above 348 amu are observed upon desorption of the molecular film for 2300 K, 1000 K and 500 K D-atoms. These masses can only be created if deuteration of outer edge, inner edge and centre sites take place, as well as the exchange of the original H-atoms with D-atoms. These exchange reactions are expected to happen through the abstraction of HD, hence this suggests that coronene can work as a catalyst for H₂-formation. Furthermore, for the deuteration of coronene with the 1000 K atomic D beam, several peaks were observed in the mass distribution. This is attributed to the higher stability of certain hydrogenation states. At high masses two significant peaks appear which are always 12 amu apart. These are proposed to relate to centre site addition, suggesting a high barrier for the first centre site addition reaction.

The cross-sections for addition and abstraction of D during deuteration with 2300 K D-atoms were investigated by comparing the experimental measurements with kinetic simulations. This investigation suggests that the cross-section for D addition is independent of the number of available sites for addition. This may indicate that the incoming D-atoms are mobile on the coronene molecule and are able to scan the molecule for available addition sites. Furthermore the simulations suggest that the cross-section for abstraction scales linearly with the number of sites for abstraction, i.e., the number of excess D-atoms added to the molecule. It was found that a cross-section for abstraction of 0.01 \AA^2 per site replicated the experimental data best. This is lower than a previously measured cross-section of 0.06 \AA^2 found for 300 K D-atoms measured by Mennella *et al.* [74]. We suggest that this is partly caused by the observed loss of molecules during the deuteration process when using 2300 K D-atoms, which is thought to consist mainly of deuterated molecules. However, other factors than the beam temperature differs in the two studies. Mennella *et al.*, for instance, used multilayers of coronene rather than monolayers on graphite.

E_{des} was also calculated for the deuterated coronene films. This analysis revealed that the deuteration of the coronene molecule reduces E_{des} from 1.78 eV at 300 amu to 1.34 eV at 348 amu. For higher masses E_{des} increases again resulting in $E_{des} = 1.43$ eV at 360 amu. The decrease in E_{des} is expected to be because of the removal of electrons from the π -electron system, as well as a buckling of the coronene molecule. DFT calculations show that the decrease in the number of π -electrons results in only a small decrease

in binding energy; fully trans-hydrogenated coronene results in a binding energy of 1.80 eV, compared to 1.90 eV for ordinary coronene. Buckling and hydrogenation from the bottom, on the other hand, seems to result in a much larger decrease; fully cis-hydrogenated coronene has a binding energy of 1.09 eV. When comparing the DFT calculations with the experimental data, the DFT suggest that the coronene molecules initially gets hydrogenated on the bottom side for masses below 310 amu. For masses above 310 amu the DFT calculations predict that the molecules are slightly buckled. The increase in binding energy from 347 amu to 360 amu, could suggest a decrease in the buckling of the molecule through the final addition reactions. That is, the molecule gain a more planar geometry as the saturated superhydrogenated structure is approached.

Hydrogenation of coronene through interaction with deuterated graphite was also investigated and shows that 0.25 ML of coronene is sufficient to suppress the D desorption signal regardless of whether D or coronene is dosed first. This suggests coronene to be mobile on the surface and that it can react with the adsorbed deuterium. This was confirmed by measuring the masses of the desorbing coronene molecules which showed masses up to 340 amu. Only 8 ± 3 % of the adsorbed D-atoms were accounted for following the experiment. The rest are expected to have desorbed as HD/D₂, suggesting that PAHs adsorbed on hydrogenated carbonaceous grains may serve as a route to release H₂ as well as a route to superhydrogenated PAH species.

Chapter 5

Scanning tunneling microscopy measurements

In this chapter all the scanning tunneling microscopy results obtained during my PhD will be discussed. The first section (5.1) will focus on STM measurements of pristine coronene on graphite and the different structures and imaging modes observed. The second section (5.2) will look into STM measurements of hydrogenated coronene on graphite, where both a 2300 K and a room temperature (RT) H-atom beam were used.

All the new STM measurements presented in this chapter were carried out at LHe temperatures (~ 5 K) and are unpublished. The DFT calculations on adsorption geometry used for comparison were published in [49].

The measurements presented here were carried out together with Jakob Holm Jørgensen, Richard Balog and Frederik Doktor Simonsen. The DFT calculations on adsorption geometry were made by Mie Andersen and Lara Ferrighi under supervision of Bjørk Hammer.

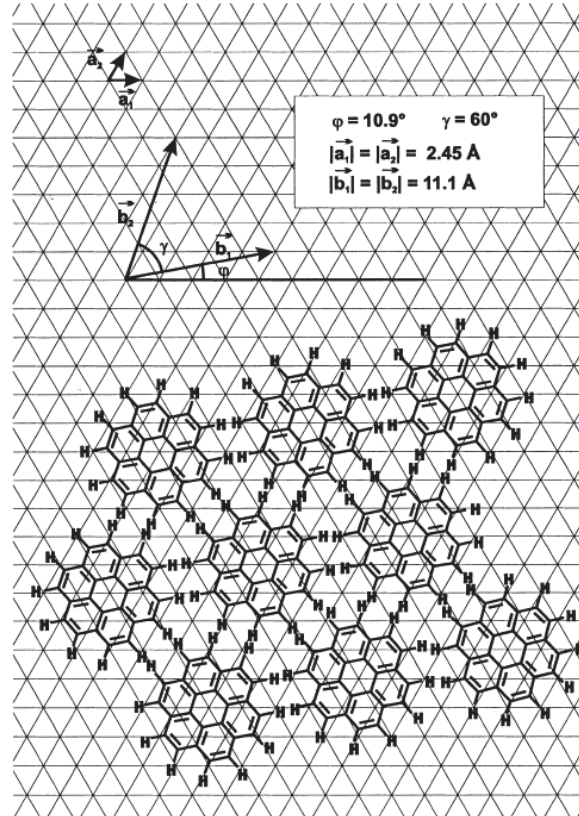


Figure 5.1: Illustration of the adsorption pattern of a coronene monolayer on graphite. The coronene creates a $\sqrt{21} \times \sqrt{21} \text{ R} \pm 10.9^\circ$ superstructure on the graphite [54]

5.1 Pristine coronene on graphite

Coronene monolayers on graphite have previously been investigated using STM [49] [54] [55], as mentioned in section 3.1 where a selection of such STM images are shown. All studies revealed a close-packed structure following a $\sqrt{21} \times \sqrt{21} \text{ R} \pm 10.9^\circ$ superstructure on the graphite. This superstructure is illustrated in figure 5.1 and corresponds to an intermolecular distance of 11.1 \AA , hence $b_1 = b_2 = 11.1 \text{ \AA}$. Submonolayer coverages of coronene have also been investigated before with STM at 20 K [55], however, coronene molecules were observed to be extremely mobile and stable coronene islands were only found at step edges.

Recently, an attempt to simulate STM images of coronene on graphite was made using DFT. This was done using the optB88-vdW functional [56] and compared to experimental work. Two different imaging simulation approaches were used together with the DFT; the Tersoff-Hamann approxima-

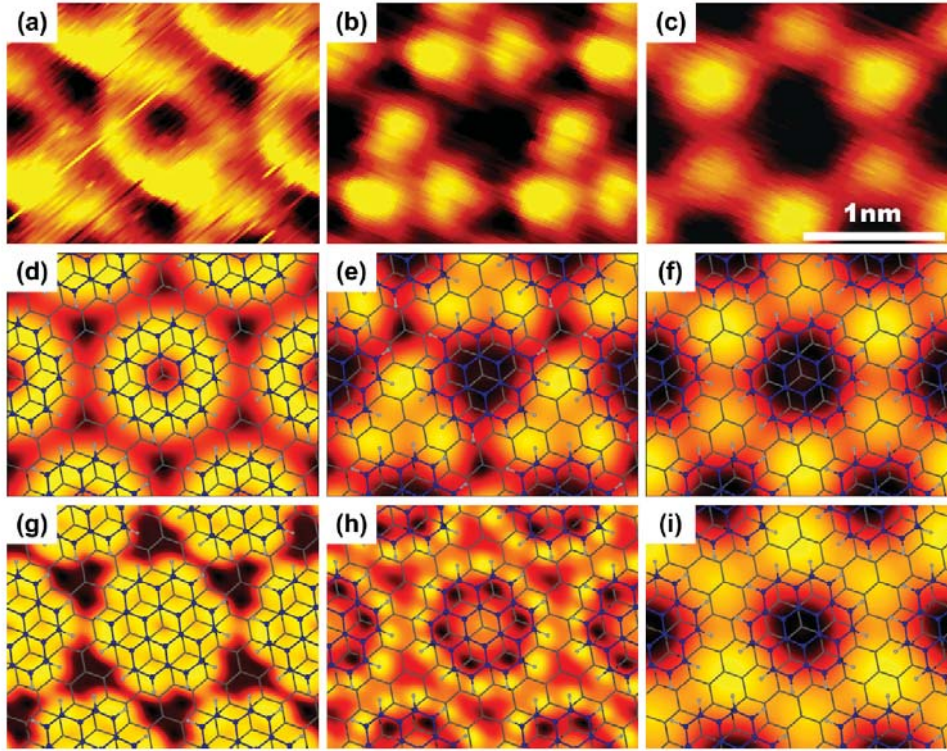


Figure 5.2: Experimental [(a)-(c)] and simulated [(d)-(i)] STM images of a coronene monolayer on graphite (graphene from simulations). The experimental scanning parameters are (a) $V_t = -3.11$ V, $I_t = 70$ pA, (b) $V_t = 1.74$ V, $I_t = 120$ pA, and (c) $V_t = 4.14$ V, $I_t = 110$ pA. (d)-(f) ESQC simulated images with the superimposed atomic structure. The simulated tunneling parameters are (d) $V_t = -2.83$ V, $I_t = 70$ pA, (e) $V_t = 3.46$ V, $I_t = 23$ pA, (f) $V_t = 4.20$ V, $I_t = 2.2$ pA. (g)-(i) DFT-TH simulated images with the superimposed atomic structure. The simulated tunneling parameters are (g) $V_t = -2.83$ V, $I_t = 500$ pA, (h) $V_t = 3.46$ V, $I_t = 500$ pA, (i) $V_t = 4.20$ V, $I_t = 500$ pA. Figure reproduced from [56].

tion (DFT-TH) [37] and the elastic scattering quantum chemistry (ESQC) method [147] [148]. DFT-TH models the tip as a sphere with a single s-wave state, whereas the ESQC method allows for a more realistic tip description by choosing a specific tip apex. The resulting calculated images were compared with experimental measurements for three different imaging modes, the results are shown in figure 5.2. The experimental images were measured at the SDL lab using an Aarhus STM [149] at 120 K and are shown in figure 5.2(a)-(c). The images generated using the ESQC method reproduce the experimental images well at all scanning parameters, while the DFT-TH only shows a good agreement at high bias voltages. Two important things

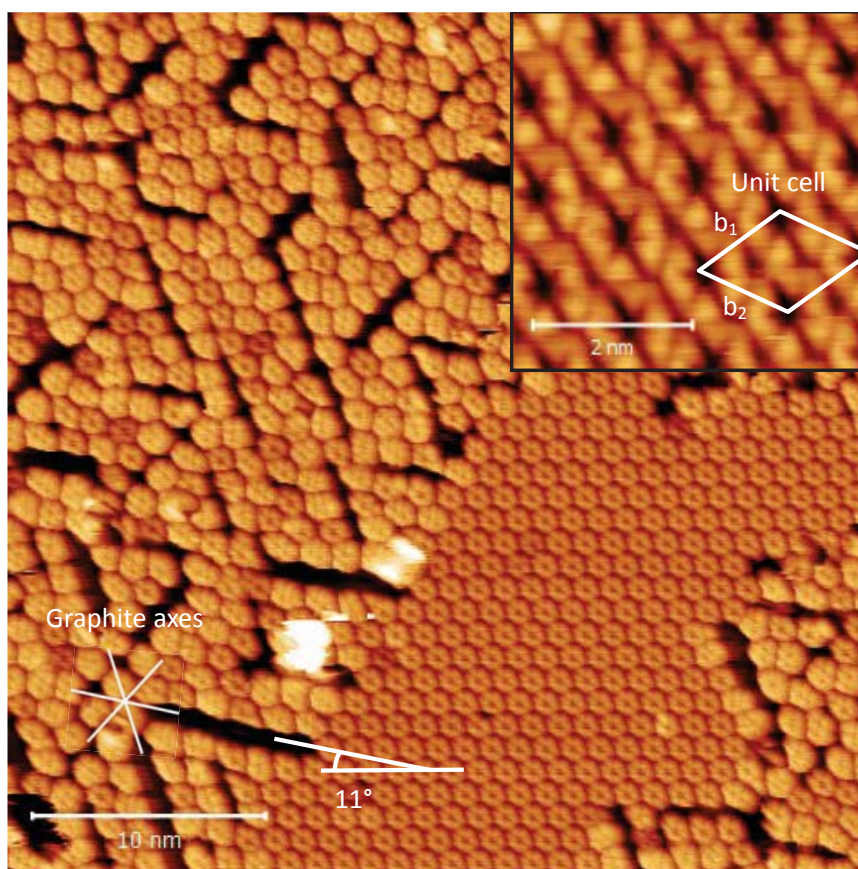


Figure 5.3: STM image of coronene on graphite at 5 K with a coverage close to a monolayer. The graphite axes and angle between one axis and the coronene superstructure are illustrated. The scanning parameters are: $V_t = -1.90$ V, $I_t = 68$ pA. The inset shows the closed packed structure in a similar imaging mode, with the unit cell superstructure illustrated. The scanning parameters are: $V_t = -3.00$ V, $I_t = 60$ pA

should be taken from this study. First a realistic tip description is extremely important for the image-simulations of the coronene molecules using DFT. Second the molecules can appear both as bright (figure 5.2(a)/(d)) and as dark (figure 5.2(b)+(c)/(e)+(f)) compared to the space between them, when observed with STM. Therefore DFT calculations are often crucial to determine their specific configuration.

In this thesis STM measurements of coronene deposited on HOPG at varying coverages were performed. The HOPG was cleaved prior to being mounted in the sample holder and annealed to at least 1100 K before experiments. Coronene was deposited using our Knudsen-cell evaporation source and the sample was subsequently annealed to approx. 390 K to desorb

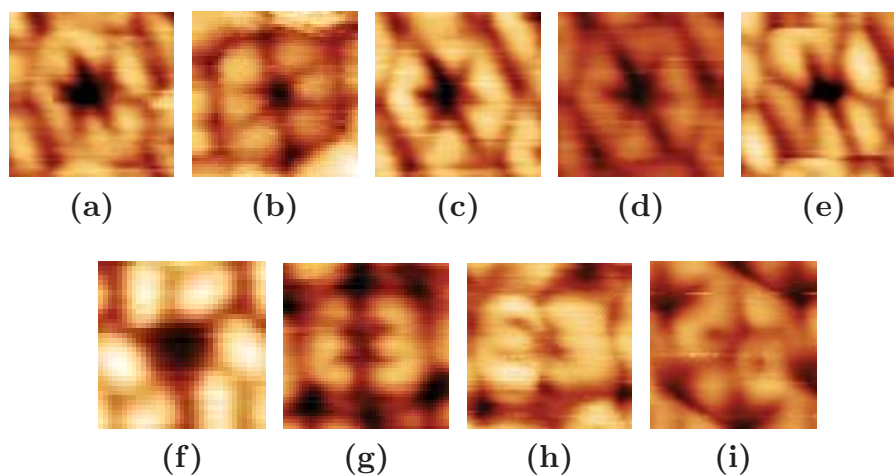


Figure 5.4: STM images of individual coronene molecules as found in close-packed configuration on graphite. Images were taken with different scanning parameters and/or imaging mode. All images are $14 \times 14 \text{ \AA}$. The scanning parameters are: (a) $V_t = -3.25 \text{ V}$, $I_t = 60 \text{ pA}$, (b) $V_t = -3.00 \text{ V}$, $I_t = 68 \text{ pA}$, (c) $V_t = -3.00 \text{ V}$, $I_t = 60 \text{ pA}$, (d) $V_t = -2.75 \text{ V}$, $I_t = 60 \text{ pA}$, (e) $V_t = -2.25 \text{ V}$, $I_t = 60 \text{ pA}$, (f) $V_t = -3.56 \text{ V}$, $I_t = 65 \text{ pA}$, (g) $V_t = -3.17 \text{ V}$, $I_t = 56 \text{ pA}$, (h) $V_t = -3.00 \text{ V}$, $I_t = 56 \text{ pA}$ and (i) $V_t = -2.76 \text{ V}$, $I_t = 60 \text{ pA}$

multilayers and create a saturated monolayer.

An STM image taken at a coverage close to 1 ML is shown in figure 5.3. Here two different packing structures are observed. In the bottom right side of the image a close packed structure with six fold symmetry is present, where all molecules are imaged in the same way. The rest of the image shows a less dense packing phase with vacancy lines occurring in three different directions. Here individual molecules do not look symmetric, which is attributed to differences in the local environment for the individual molecules. Small patches of the close packed phase are also observed in the less dense phase. Close inspection of the low density phase reveals that the three directions observed follow the graphite axes. As illustrated in figure 5.3 the close packed area is rotated $11^\circ \pm 1^\circ$ compared to the graphite axis. The inset shows an image taken of the close packed phase in a similar imaging mode. A unit cell is illustrated in this inset. The side lengths of the unit cell is identified and $b_1 = b_2 = 11 \pm 1 \text{ \AA}$. This is consistent with the previously observed $\sqrt{21} \times \sqrt{21} \text{ R} \pm 10.9^\circ$ superstructure [49] [53] [54] [55].

The imaging mode shown in figure 5.3 is very similar to the one observed/simulated in figure 5.2 (a)/(d), however with more sub-molecular

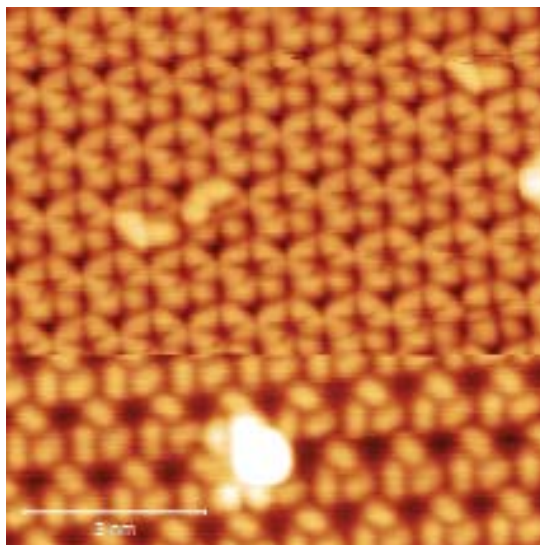


Figure 5.5: STM image of a close packed monolayer of coronene on graphite, where the imaging mode changes while scanning from top to bottom. The layer is slightly hydrogenated. The scanning parameters are $V_t = -3.56$ V, $I_t = 65$ pA

structure. Six individual lobes are observed, rather than a single ring, consistent with the 6 outer benzene rings. A zoom in on an individual molecule from the inset is shown in figure 5.4(c). The same imaging mode is observed for different bias voltages, as shown in figure 5.4(a)-(e), where individual molecules from other measurements are shown. An imaging mode similar to the one in figure 5.2 (b)/(e), has also been observed, as shown in figure 5.4(f). Completely different imaging modes were also observed as shown in figure 5.4(g)-(i). The measurements could suggest that a specific imaging mode is related to what is adsorbed on the tip, rather than the bias voltage, since a specific imaging mode can be found over a large range of bias voltages. The imaging mode can also change completely while scanning at a specific bias. An example of this is shown in figure 5.5, where the scanning parameters are kept constant and the imaging mode changes radically in the bottom 1/3 of the image. We note that this image was recorded after the ML was exposed to atomic H and we attribute the bright protrusion to adsorbed H-atoms. This suggests that DFT comparison might be even more complicated than previously described and a new tip model could be needed.

Submonolayer coverages were established by heating the sample higher than 390 K after exposing the graphite to coronene. Examples are shown in figure 5.6. For coverages close to a monolayer, as in figure 5.6(a) (similar to 5.3), the coronene molecules follow the graphite lattice and narrow lines

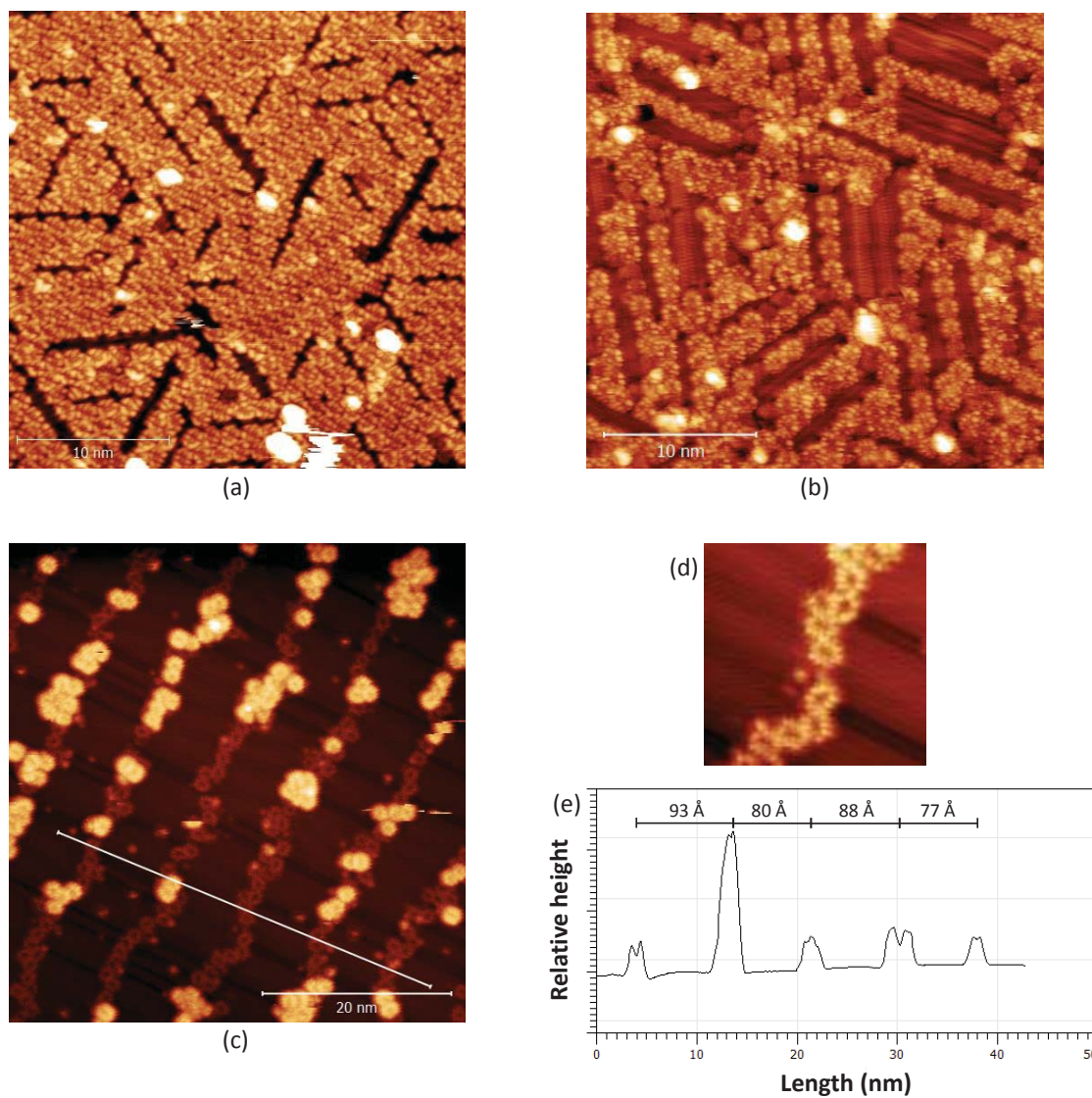


Figure 5.6: STM images of coronene on graphite with submonolayer coverages. The coverages are decreasing from (a) to (c). The scanning parameters are: (a) $V_t = -2.50$ V, $I_t = 76$ pA, (b) $V_t = -2.58$ V, $I_t = 64$ pA and (c) $V_t = -2.46$ V, $I_t = 36$ pA. (d) Is a 110×110 Å zoom in on an area in (c) only containing a single layer of molecules. (e) Is a line profile of the line illustrated in (c) with the length between the coronene lines displayed.

of vacancies are present. When the coverage is very close to a complete monolayer small patches of the $\sqrt{21} \times \sqrt{21} \text{ R} \pm 10.9^\circ$ superstructure is also observed. At intermediate coverages, as shown in figure 5.6(b), the coronene molecules form single or double lines which follow the graphite lattice axes with broader lines of vacancies between them. At very low coverages lines of single coronene molecules have been observed. This is shown in figure 5.6(c). The lines are all following the same graphite axis, although they are not completely straight. The lines are equally spaced and $85 \pm 5 \text{ \AA}$ apart, suggesting a form of long range interaction. Molecules are, in some places, observed to form second layers in disagreement with the Stranski-Karstanov growth mode previously observed, as well as the other submonolayer images. We note that in all of these submonolayer images a new imaging mode is observed, which has only been observed in submonolayers. When scanning on submonolayer films the scanning conditions were generally more unstable than for the close-packed monolayers and molecules were often moved around by the tip. This explains why the structure has not been observed in previous studies, which were carried out at higher temperatures. The bright parts in figure 5.6(a) and (b) are attributed to coronene molecules adsorbed on top of the coronene bottom layer. The graphite is hard to distinguish in the presented images due to the difficult imaging conditions, but close inspection of certain submonolayer images reveals the graphite lattice.

In order to investigate the binding of a monolayer of coronene on graphite, the most stable adsorption structure was investigated with DFT in [49] using the optB88-vdW functional. This is also relevant for the understanding of the monolayer structure in STM and it was also these calculations that yielded the binding energies used for comparison with measurements in section 4.1 and 4.4. The DFT calculations suggest that the most stable structure/lowest energy for a single coronene molecule is achieved when the molecule adsorbs flat at a distance of 3.36 \AA above the graphite basal plane. AB stacking is preferred with respect to the graphite. Hence every second carbon atom in the coronene molecule is located above the center of a carbon hexagon in the graphite and every other coronene C-atom is directly above a carbon atom in the upper graphene layer. This is very similar to what is observed for the different layers in a graphite crystal where the distance between graphene layers is 3.35 \AA [150] and AB stacking predominate. The diffusion barrier was found to be 23 meV for the lowest energy path, supporting the hypothesis that molecules are mobile even at low temperatures. When calculating the stable monolayer structure only AB stacking has been

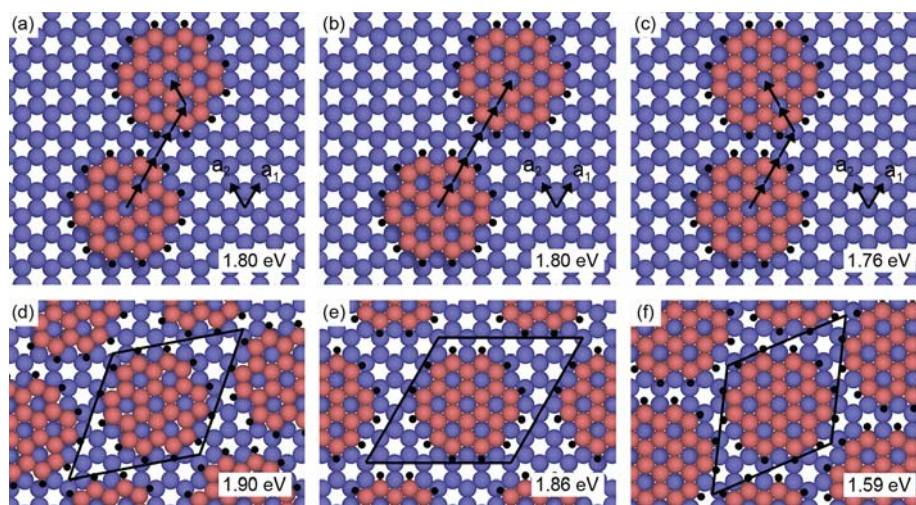


Figure 5.7: (a-c) Adsorption geometries and binding energies per molecule for dimer complexes found with DFT. The distances between the molecules are indicated in units of the graphite lattice vectors a_1 and a_2 and correspond to (a) 11.27 Å, (b) 12.30 Å, and (c) 10.72 Å. (d-f) Monolayer structures constructed from the dimer structures in (a-c) and the corresponding binding energies per molecule. [49]

considered. Three different lattice parameters have been investigated 11.27 Å, 12.30 Å and 10.72 Å, where the 11.27 Å corresponds to what has been experimentally determined by LEED [53]. The structures and the corresponding binding energies are shown in figure 5.7, where (a)-(c) are dimer structures and (d)-(f) are the corresponding monolayer structures. The overall most stable structure with a binding energy per molecule of 1.90 eV, is the one for a lattice parameter of 11.27 Å shown in 5.7(d). The corresponding unit cell is identical to the $\sqrt{21} \times \sqrt{21} \text{ R} \pm 10.9^\circ$ determined by LEED and STM. The effect of rotating the coronene molecule around a fixed point at the center of the molecule was also investigated. This is shown in figure 5.8(a), where the potential energy curve for a 60° rotation of the molecule is plotted. The most stable structure is found at a 3.65° rotation, as illustrated in figure 5.8(b). The slight rotation away from the AB stacking is favoured because it reduces the steric hindrance between H atoms on neighbouring molecules. This avoidance of steric hindrance also gives rise to the other peaks in potential energy curve, as illustrated in 5.8(c) and (d) and means that coronene molecules will be fairly immobile in the monolayer, consistent with the improved STM imaging conditions at monolayer coverage compared to lower coverage.

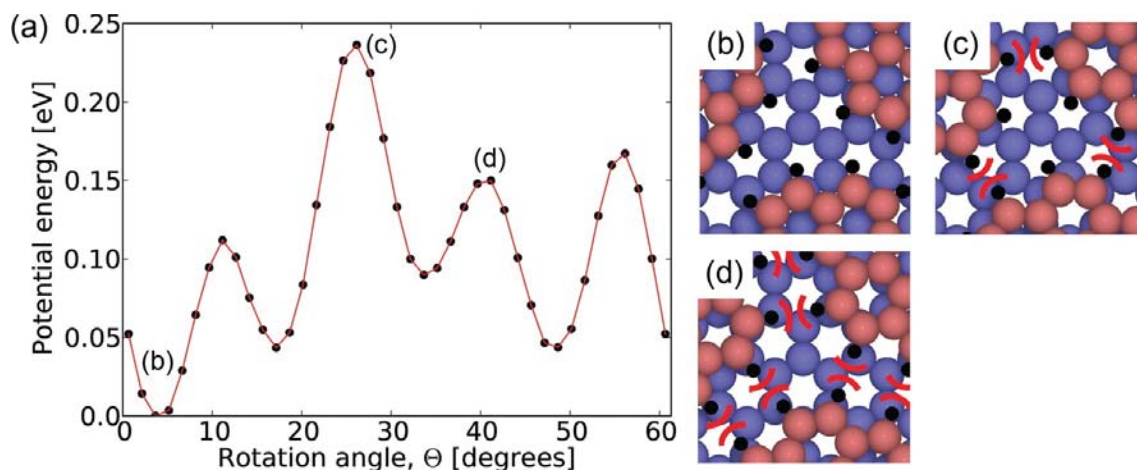


Figure 5.8: (a) The potential energy curve for rotating the coronene molecule in figure 5.7(d) counter clockwise as found with DFT. The most stable configuration is the 3.65° rotated structure shown in (b), whereas (c) and (d) picture the structures corresponding to two of the maxima as indicated on the graph in (a). The red curved lines in (c) and (d) visualize the steric hindrance between H-atoms on neighboring molecules.[49]

5.2 Hydrogenated coronene on graphite

To our knowledge studies of the hydrogenation of coronene or other PAHs using SPM have not previously been published. The reason for studying this is to get a better understanding of the addition pathway of H-atoms to coronene. As mentioned in section 3.2 DFT calculation suggest that the first 5 additions takes place at edge sites, while the 6th and 7th addition takes place at centre sites. These calculations were made on an isolated coronene molecule and the TPD measurements presented in section 4.2 suggest that centre sites are hydrogenated last, since the bottom of the molecule is blocked. A consequence of this single sided hydrogenation will also be that the molecule will start to buckle up because of the uneven hydrogenation. This would be interesting to confirm with STM.

The coronene monolayers on graphite were prepared in the same way as described in the previous section. This layer was subsequently exposed to atomic hydrogen from either a bare HABS yielding 2300 K atomic H or a HABS with a long quartz nose mounted on it, cooling the H-beam to approx. RT. The flux of H-atoms is, at the time of writing, unknown and the fluence for the individual measurements presented in this chapter is

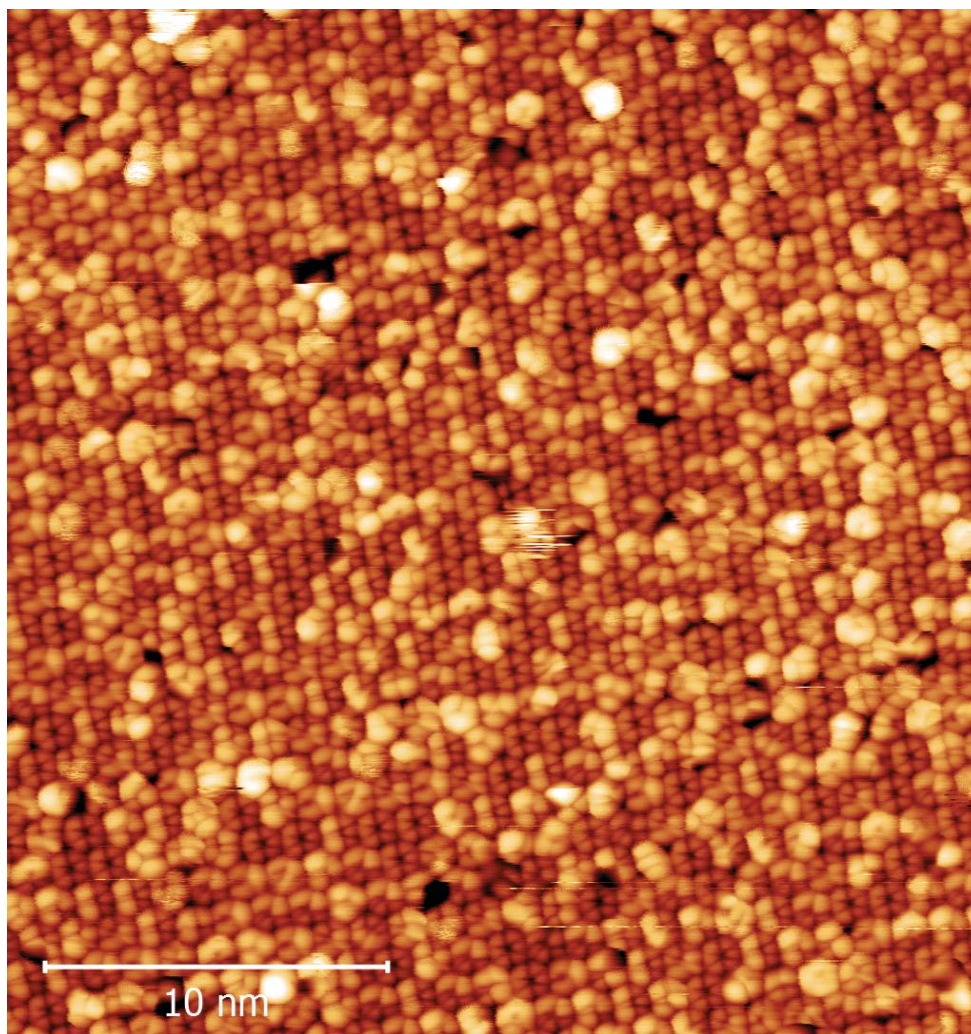


Figure 5.9: STM image of a coronene monolayer on graphite hydrogenated with 2300 K H-atoms. Scanning parameters are: $V_t = -3.00$ V, $I_t = 68$ pA

therefore unknown.

An example of a hydrogenated monolayer of coronene is shown in figure 5.9. This was hydrogenated using 2300 K H-atoms. A clear difference can be seen compared to a pristine coronene monolayer. Only 30 % of the molecules now show the 6 lobe structure mentioned in the previous section (figure 5.4(a)-(e)) and are taken to be non-hydrogenated. The rest of the molecules appear brighter in STM, either some of their lobes seem brighter or they appear to have a completely different structure. This is attributed to different degrees of hydrogenation of the molecules. Several vacancies are also present in the layer imaged as dark areas. The unit cell is, however, the same as for the non-hydrogenated monolayer. A comparison between

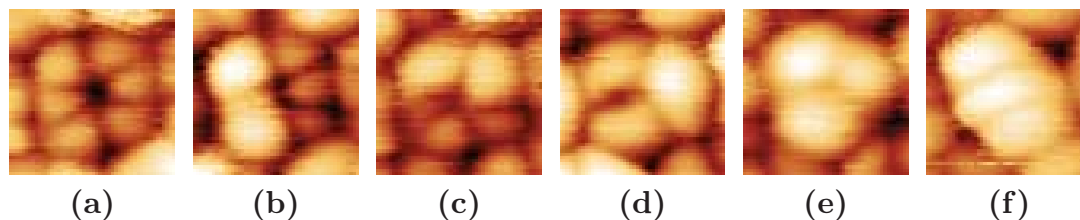


Figure 5.10: Individual molecules have been extracted from figure 5.9 and are shown to illustrate the diversity of structures which were observed in coronene after hydrogenation. (a) Pristine coronene molecule. (b)-(f) hydrogenated coronene molecules. All images are $14 \times 14 \text{ \AA}$. The scanning parameters are: $V_t = -3.00 \text{ V}$, $I_t = 68 \text{ pA}$

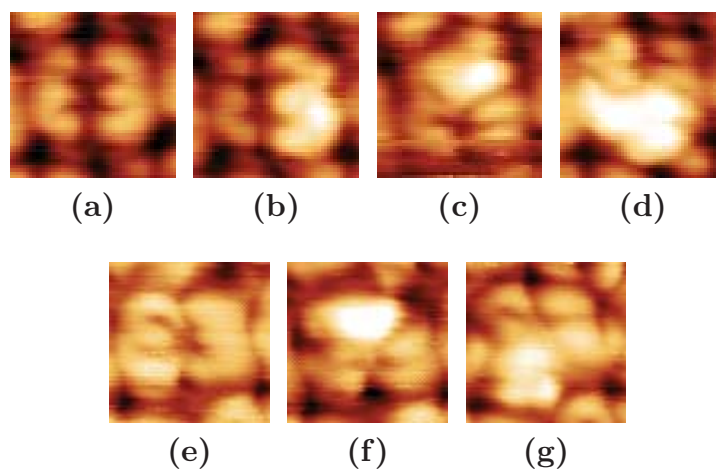


Figure 5.11: Images of individual coronene molecules which were recorded after close-packed coronene monolayers were exposed to 2300 K H-atoms. (a) and (e) are the pristine coronene molecules, (b)-(d) and (f)-(g) are hydrogenated molecules from the respective layers. The scanning parameters are: (a) $V_t = -3.17 \text{ V}$, $I_t = 56 \text{ pA}$ and (b) $V_t = -3.00 \text{ V}$, $I_t = 56 \text{ pA}$. All images are $14 \times 14 \text{ \AA}$

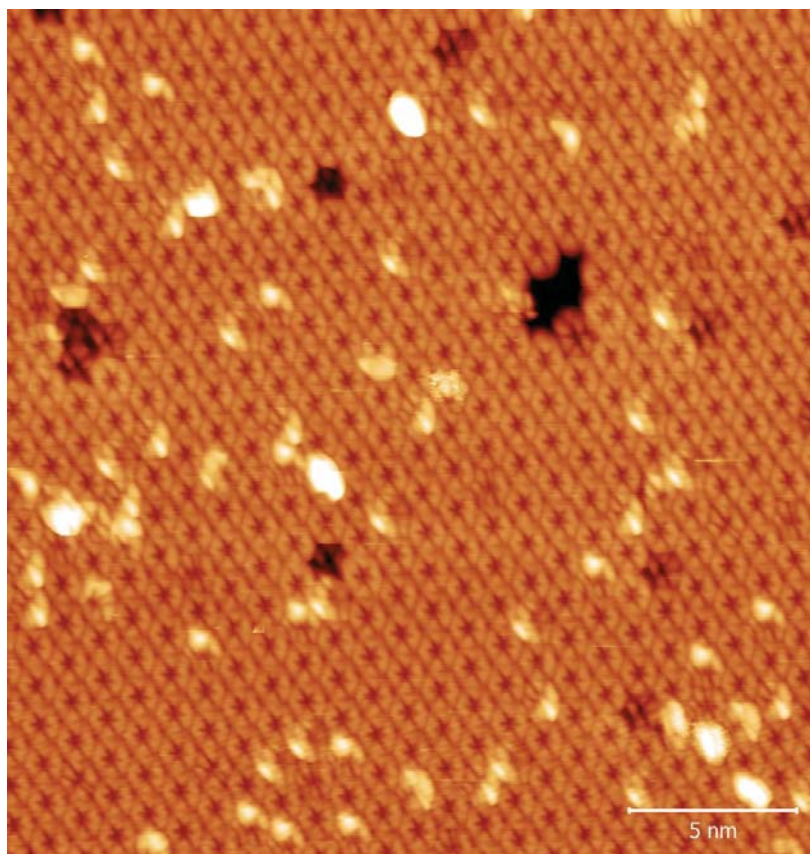


Figure 5.12: STM image of a coronene monolayer on graphite hydrogenated with RT H-atoms. Scanning parameters are: $V_t = -3.00$ V, $I_t = 60$ pA

observed molecular types from figure 5.9 is shown in figure 5.10. Figure 5.10(a) shows an image of one of the molecules that appears unchanged after the hydrogenation and are assumed to be a pristine coronene molecule. The rest of the images in figure 5.10 are the molecules that have changed after exposure to H-atom and are therefore taken to be hydrogenated. These can be separated into three different types. There are molecules showing bright patches, while the rest of the molecule keeps the original lobe structure (Figure 5.10 (b) and (c)). This is the most commonly observed type. Second there are also molecules where most of or the whole of outer ring appears bright, while the original lobe structure has disappeared (Figure 5.10 (d) and (e)). These are also fairly common. Third there are examples where the whole molecule appears bright and looks elongated (Figure 5.10 (f))). Few of these are observed.

Molecules from two other imaging modes are shown in figure 5.11, with (a) and (e) being the pristine molecule for the two modes and (b)-(d) and (f)-

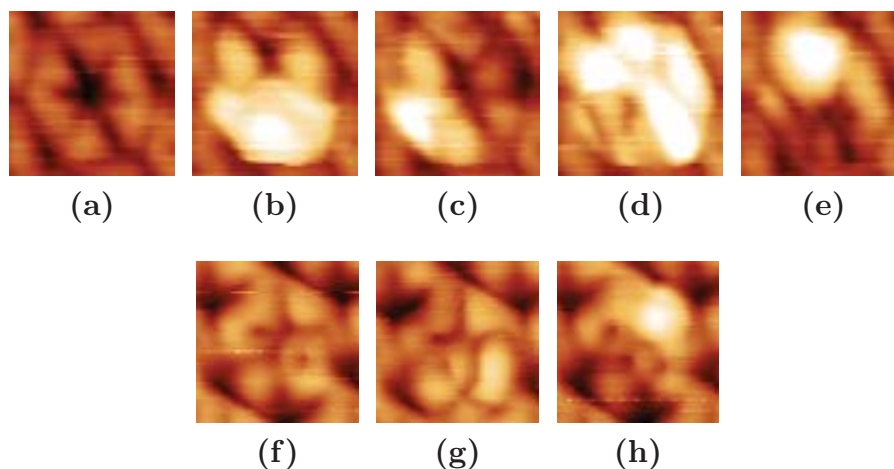


Figure 5.13: Images of individual coronene molecules which were recorded after close-packed coronene monolayers were exposed to RT H-atoms. (a)-(e) are molecules from the image in figure 5.12. (a) and (f) are the pristine coronene molecules, (b)-(e) and (g)-(h) are hydrogenated molecules from the respective layers. The scanning parameters are: (a) $V_t = -3.00$ V, $I_t = 60$ pA and (b) $V_t = -2.76$ V, $I_t = 56$ pA. All images are 14×14 Å

(g) being the respective hydrogenated molecules. The hydrogenation level is generally lower for these measurements because of a lower H flux and only 1/3 or half of the individual molecules appear bright.

Figure 5.12 shows a monolayer of coronene hydrogenated with a RT H-beam. Due to an untested design of the cooling nozzle only low degrees of hydrogenation were achieved. The layer is generally close-packed with some vacancies. A closer look on the hydrogenated molecules is given in figure 5.13(a)-(e), with (a) being the pristine molecule. Here typically only half of the molecule appears bright, consistent with the lower degree of hydrogenation. Another imaging mode is shown in figure 5.13(f)-(h), with (f) being the pristine molecule. Here one third or less appears bright.

For the coronene molecules hydrogenated with the 2300 K H-beam as well as the RT H-beam, the most observed change is that half of the molecule or less appears brighter than for the pristine molecule. This suggests that hydrogen atoms are added to one or more edge sites. The second most common structure is the one where most or all of the outer lobes light up. This suggests a higher degree of hydrogenation, however, since the middle of the molecule still appears dark in both cases, one would think that the centre sites are not hydrogenated. It is of course unknown if this

is because the whole outer ring is hydrogenated or because similar parts of the edge carbon structure is hydrogenated. This is all consistent with DFT studies [65] as well as the TPD studies presented in the previous chapter, suggesting that it is preferential to hydrogenate edge sites before centre sites. In order to determine when the centre sites get hydrogenated higher degrees of hydrogenation will, however, have to be observed. In order to determine the specific addition sites DFT simulated images will properly be needed. The elongated molecule in figure 5.10(f) could be a buckled molecule.

Images of hydrogenated submonolayers were also obtained, but due to the dependence of the local environment for the imaging of the individual molecules, the hydrogenated layer looks very messy. This make any qualitative analysis impossible and will therefore not be discussed here.

5.3 Conclusion

In summary the coronene monolayer was confirmed to follow the $\sqrt{21} \times \sqrt{21}$ R $\pm 10.9^\circ$ superstructure on the graphite in agreement with previous studies, however, with improved sub-molecular structure reported here. The coronene monolayers showed several different imaging modes, which can be attributed to different tunnelling parameters or, in some cases, molecules adsorbed at the tip. The most observed imaging mode showed a 6 lobe structure, with a dark centre ring, consistent with the six outer benzene rings and the one centre ring. Submonolayers were observed to be less stable than a complete monolayer and molecules were observed to be adsorbed along the three graphite axes. At very low coverage the molecules were observed to only follow one direction of the graphite in the form of lines with an equal spacing of 85 ± 5 Å, suggesting a form of long range interaction. DFT calculations attributed the higher stability of the complete monolayer to the molecules interlocking by rotating slightly away from the AB stacking to avoid steric tension.

After hydrogenating a monolayer of coronene with either 2300 K or RT H-atoms several molecules showed brighter parts, when imaged with STM. When imaged in the 6 lobe structure imaging mode, the changed molecules mostly showed one or more brighter lobes. This is attributed to hydrogenation of the edge carbon atoms to different hydrogenation states. This is consistent with the TPD measurements and calculations suggesting that edge atoms get hydrogenated first. A few molecules hydrogenated with 2300

K H-atoms appeared elongated and showed a completely different structure. This could be due to buckling of the superhydrogenated coronene molecule.

Generally more STM investigations are needed to support the suggested hydrogenation pathway for both the 2300 K and RT H-atoms. We will need to achieve higher degrees of hydrogenation and observe the change in the appearance of the molecules as a function of hydrogenation level. This will still only allow us to speculate on the specific hydrogenation configuration based on the STM-images alone and DFT calculations will probably be needed to confirm these speculations.

Chapter 6

Summary and Outlook

This chapter provides a summary of the results presented in this thesis together with an outlook suggesting future experiments. The summary is written in such a way that it can be read independent from the rest of the thesis and can therefore be viewed as an abstract to the entire thesis.

6.1 Summary

PAHs are thought to account for 5 - 20 % of all carbon in the ISM and are believed to be ubiquitous. They have been suggested to catalyse the formation of molecular hydrogen in the ISM and it is this role which motivates the work presented in this thesis.

In this thesis I have presented TPD measurements describing the desorption of pristine coronene from graphite. This showed two distinct desorption peaks; a monolayer peak following first-order desorption kinetics, peaking at 465 K; and a continuously growing multilayer peak following zero-order kinetics with the peak starting at around 320 K. The pre-exponential factor for the monolayer was calculated using transition state theory and the desorption energy of the monolayers was determined to be 1.8 ± 0.1 eV in good agreement with the binding energy found with DFT calculations executed yielding 1.90 eV. The desorption energy for the multilayer was found to be 1.4 ± 0.1 eV.

Pristine coronene films were also investigated using STM. The coronene monolayer was confirmed to follow the $\sqrt{21} \times \sqrt{21}$ R $\pm 10.9^\circ$ superstructure on graphite as reported in previous studies. Coronene monolayers were observed to show several different imaging modes. Submonolayers were also observed and were found to be less stable than the complete monolayer and the molecules were found to adsorb along the three graphite axes.

Coronene monolayers on graphite were exposed to atomic D and probed in TPD experiments. Masses above 348 amu were observed, using 2300 K, 1000 K and 500 K D-atoms. These masses can only be created if deuteration of outer edge, inner edge and centre sites take place, as well as the exchange of the original H atoms with D atoms. These exchange reactions are expected to happen through Eley-Rideal abstraction of HD, hence this indirectly suggests that coronene can work as a catalyst for H₂-formation. Furthermore, for the deuteration of coronene with the 1000 K atomic D beam, several peaks were observed in mass distribution. This was attributed to higher stability of certain hydrogenation states. After high fluence exposure, two significant peaks appear at high masses, which are always 12 amu apart. This may be related to centre site addition, suggesting a high barrier for the first centre site addition.

From the 2300 K D-atom experimental data the reaction cross-sections for addition of D and abstraction of HD/D₂ were investigated by comparing the experimental measurements with kinetic simulations. The experimental

data was best replicated when the cross-section for D addition are independent of the amount of available addition sites. This may indicate that the incoming D atoms are mobile on the coronene molecule and are able to scan the molecule for available addition sites. The simulations also suggest that the cross-section for abstraction scales linearly with the number of sites for abstraction, i.e., the number of excess D atoms added to the molecule.

The desorption energy was evaluated for coronene films deuterated with 2300 K D-atoms. This analysis revealed that the deuteration of the coronene molecule reduces binding energy from 1.78 eV at 300 amu to 1.34 eV at 348 amu and after this it increases to 1.43 eV at 360 amu. This decrease was explained by the removal of π -electrons from the π -electron system, as well as buckling of the coronene molecule. DFT calculations show that hydrogenation from the bottom side of the coronene molecule is needed to replicate the initial decrease in binding energy up to 310 amu. At higher masses the binding energy suggests the molecule to be slightly buckled due to single sided hydrogenation of the molecule. The increase in binding energy at high masses could then be related to a decrease in buckling.

The hydrogenation of coronene was investigated with STM for both 2300 K and RT H-beams, to gain information about the reaction pathway. After exposure to H-atoms parts of some molecules or whole molecules started to appear brighter when imaged with STM. In almost all cases only the outer parts of the molecules appeared bright, suggesting that hydrogenation at low hydrogen fluxes predominantly happens at the edge carbon atoms of the coronene molecule. This is consistent with the TPD measurements and DFT calculations suggesting that edge atoms get hydrogenated first.

The deuteration of coronene through interaction with deuterated graphite was also investigated. This showed that 0.25 ML of coronene is sufficient to suppress the D desorption signal, suggesting that coronene is mobile on the surface and can react with the adsorbed deuterium. This was confirmed by measuring the masses of the adsorbed coronene molecules and these showed highly deuterated species. Only 8 ± 3 % of the deposited D atoms could be accounted for, suggesting that the coronene molecules can abstract H_2 from hydrogenated graphite.

6.2 Outlook

There are plenty of opportunities for further studies of the hydrogenation/deuteration of PAHs and many questions still remain unanswered.

TPD measurements using 1000 K H-atoms rather than D-atoms are the next step and this will give a greater insight in to the stable hydrogenation states, since abstraction will not yield a mass change. This could also be achieved by using a D beam and the deuterated coronene analogue, $C_{24}D_{12}$, which we have available. Experiments could also be done using perhydrocoronene ($C_{24}H_{36}$), the fully hydrogenated coronene analogue. Here only abstraction reactions with D will yield a change in mass, hence these can be investigated in greater detail. However, the molecules we have available are trans-perhydrocoronene meaning that the results might not be directly transferable to the TPD measurements presented in this thesis, since the results presented in section 4.4 suggest the formation of slightly cis-hydrogenated coronene. All of the above measurements could also be interesting to repeat at lower H/D temperatures applicable to the ISM.

All of the measurements mentioned above can be compared to the previously mentioned site specific kinetic simulation algorithm under development by one of our collaborators, Herma Cuppen from Nijmegen, Netherlands. This will hopefully allow extraction of reaction cross-sections with higher precision for the individual addition/abstraction sites.

Further STM measurements are also planned, where higher degrees of hydrogenation will be investigated and DFT calculations can hopefully be made to get a better understanding of the hydrogenation configurations. Further STM investigations will also probe the change to the hydrogenated graphite after exposure to coronene. This is analogous to the TPD measurements presented in section 4.5. Better submolecular resolution might also be acquired by using other types of scanning probe microscopy, including functionalized tip STM or AFM. In functionalized tip STM/AFM a molecule, typically CO, is adsorbed on the tip. This can yield impressive submolecular resolution and has been shown to image individual atoms in the PAH pentacene on Cu(111) using noncontact-AFM with a CO functionalized tip [151].

In the more distant future it would also be interesting to investigate other PAHs than coronene to study the effects of PAH size and the composition of different addition sites. Coronene is generally too small a PAH for the ISM, where the average PAH is expected to contain 50 - 150 C-atoms. PAHs of

this size can, however, not be used in our present experimental setup, where molecular masses can only be detected up to 500 amu.

Investigating the interaction between the hydrogenated coronene and UV light would also be a natural step forward, to simulate the effects of the high UV flux in the ISM. This can be achieved by exposing hydrogenated coronene to UV laser light. By using a pulsed laser the photoassisted desorption of H₂ and/or PAH fragmentation might be directly detectable with a QMS and the effect of the UV field on the hydrogenation process can be investigated. These experiments would, however, require changes to the present experimental setup.

One of the motivations for the experiments presented in this thesis and for the experiments proposed in this outlook is to provide data for future models of the ISM. This will require knowledge of reaction cross-sections as a function of atomic H temperature, PAH size and UV field, as indicated by the suggested experiments. In order to provide proper models, better observational data is also needed to couple it to the right experimental data. One would need to know the gas phase temperature, the average PAH size, the average hydrogenation level of the PAHs, the UV field parameters and the densities of PAHs and atomic hydrogen. Hence there are also a lot of future observational study possibilities.

There is of course also the possibility of moving to different reactions. One could, for instance, investigate the interaction between atomic oxygen and PAHs, to probe the role of PAHs in the oxygen chemistry of the ISM. This could lead to the creation of H₂O and/or fragmentation of the carbon skeleton to produce CO/CO₂, as observed for graphite [152]. Since we already have an atomic oxygen beam source available, these experiments could essentially be initiated right away.

Chapter 7

Dansk resumé

Dette kapitel giver et kort resumé af denne afhandling på dansk. Formålet er at give personer uden særlig kendskab til fysik og kemi et indblik i det videnskabelige arbejde udført i denne afhandling. Det må derfor også forventes at visse aspekter af det præsenterede arbejde er væsentligt forsimplet.

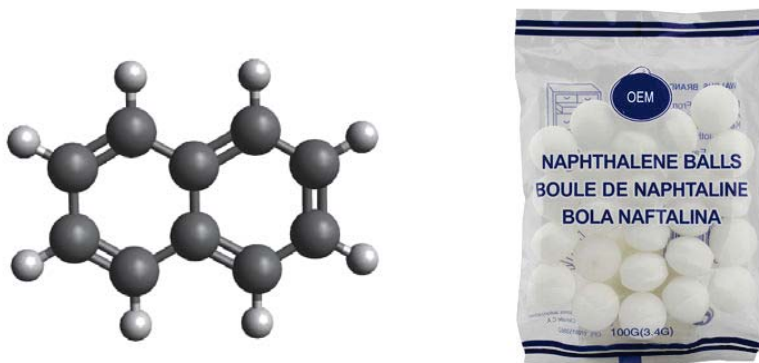


Figure 7.1: En illustration af naftalin, der består af 2 aromatiske ringe. Kulstofatomerne er vist i gråt og brintatomerne er vist i hvidt. I venstre side af billedet ses en pose mølkkugler indeholdende naftalin.

7.1 Polyaromatiske kulbrinter

Det arbejde der er præsenteret i denne afhandling, er fokuseret omkring en gruppe af molekyler kaldet polyaromatiske kulbrinter eller PAH'er. Disse molekyler består af sammenkædede aromatiske ringe, dvs. flade ringe bestående af kulstofatomer med brintatomer bundet til kanterne. PAH'er dannes blandt andet i ufuldstændige forbrændinger og findes derfor i sod, udstødning, tjære, osv. PAH'er er også med til at give den karakteristiske smag til grillede fødevarer. Mange PAH'er er dog giftige og/eller kræftfremkaldende og man forsøger derfor at begrænse dem i udstødning. Den mindste PAH, naftalin, består kun af 10 kulstofatomer og 8 brintatomer og er illustreret i figur 7.1. Naftalin har en meget stærk lugt og blev tidligere brugt i mølkkugler. I eksperimenterne præsenteret i denne afhandling blev PAH'en coronen, der består af 24 kulstofatomer og 12 brintatomer, brugt. Coronen er illustreret i figur 7.2.

PAH'er kan i vid udstrækning observeres i det interstellare medium, hvilket er området i rummet mellem alle stjernerne. PAH'er anslås at udgøre 5-20 % af alt kulstof i det interstellare medium. Man har observeret en sammenhæng mellem dannelsen af brintmolekyler og mængden af PAH'er i visse områder af det interstellare medium og det er derfor blevet foreslået, at PAH'er kan katalysere dannelsen af brintmolekyler. Mængden af observerede brintmolekyler i rummet er nemlig højere, end man kan forklare ud fra nuværende viden og man leder derfor efter katalysatorer, der kan forklare dette. Det er med denne baggrund, at mit PhD-projekt har fokuseret på

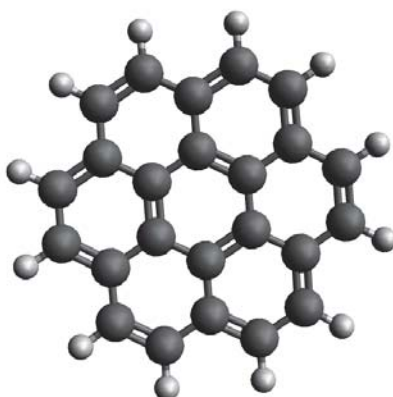


Figure 7.2: En illustration af coronen der er brugt til alle eksperimenterne i denne afhandling. Coronen består af 7 aromatiske ringe. Kulstofatomerne er vist i gråt og brintatomerne er vist i hvidt.

sammenspillet mellem brintatomer og PAH'er.

7.2 Eksperimentelle teknikker

I de eksperimenter der ligger til grund for denne afhandling, har jeg primært brugt to eksperimentelle teknikker: Temperatur programmeret desorption (TPD) og skanning tunnel mikroskopi (STM).

I TPD doserer man først atomer eller molekyler på en overflade, så disse binder sig til overfladen. Derefter opvarmes overfladen gradvist, indtil atomerne/molekylerne forlader overfladen eller desorberer. Ved at undersøge ved hvilken temperatur dette sker, kan man få information omkring, hvor stærkt atomerne/molekylerne er bundet til overfladen. I den forsøgsopstilling der er brugt i denne afhandling, blev masserne af molekylerne, der forlader overfladen også målt. Derved kan vi undersøge, om molekylerne har ændret sig på overfladen.

I STM bruger man en meget spids metaltip til at afbillede overfladen af et materiale med en så høj opløsning, at man ofte kan se de enkelte atomer. Dette gøres ved at måle den elektriske strøm der løber mellem tippen og overfladen, når disse kommer tæt på hinanden. Tippen og overfladen må ikke røre hinanden, hvilket betyder, at der ud fra klassisk fysik ikke burde løbe en strøm. Dette sker dog alligevel på grund af et fænomen kaldet tunnelering,

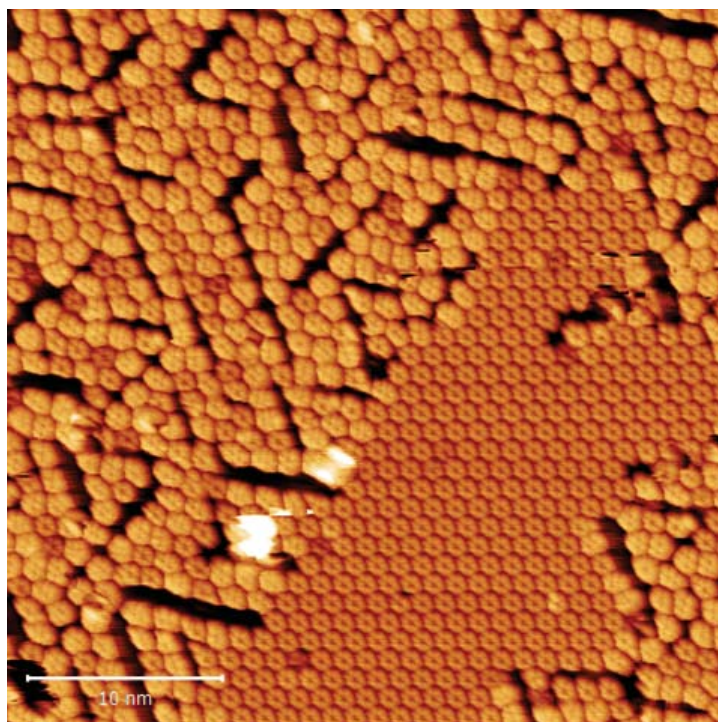


Figure 7.3: Et STM-billede af coronenmolekyler på en grafitoverflade. Coronenmolekylerne danner to forskellige mønstre. I midten ses molekyler i et sekskantet ordnet mønster, mens der på resten af billedet ses et mere uordnet mønster, hvor molekylerne ligger i linjer, der følger grafitoverfladen nedenunder.

der kommer fra kvantemekanikken. Tunneleringsstrømmen afhænger meget kraftigt af afstanden mellem tip og overflade, hvilket betyder, at man kan måle forskel på, om spidsen er lige over et atom eller mellem to atomer. Det er ud fra denne tunnelringsstrøm, at man danner et billede af overfladen.

7.3 Resultater

I forsøgene præsenteret i denne afhandling blev coronenmolekyler deponeret på overfladen af et stykke grafit. STM- og TPD-målingerne viste at molekylerne lægger sig fladt på overfladen. Ved små doser lægger molekylerne sig i linjer der følger grafitten, mens de ved højere doser følger et sekskantet mønster. Dette kan ses i STM-billedet i figur 7.3, hvor begge mønstre er til stede. Hvis flere molekyler deponeres, lægger de sig ovenpå hinanden og danner en lagkagestruktur.

Coronenfilmene blev også beskydt med brintatomer. TPD målingerne

viste at det medførte at coronenmolekylerne blev tungere, da brintatomerne bandt sig til molekylerne. Faktisk blev der målt molekyler med op til 24 ekstra brintatomer, hvilket er det maksimale antal ekstra brintatomer det fysisk kan lade sig gøre at sætte på molekylerne. Dette skyldes at der kun kan sættes et ekstra brintatom på hvert kulstofatom. Desuden observerede vi, at de indkomne brintatomer kunne reagere med de brintatomer, der allerede sad på coronenmolekylet og derved dannede brintmolekyler. Det tyder derfor på at PAH'er kan fungere som katalysatorer for dannelsen af molekylært brint. Der blev desuden bestemt såkaldte reaktionstværsnit, der fortæller, hvor sandsynligt det er at brintatomerne reagerer med coronenmolekylerne. Disse kan i fremtiden bruges i modeller til at beskrive det interstellare medium.

STM- og TPD-målinger på coronenfilmene efter beskydning med brintatomer indikerede også, at brintatomerne først sætter sig på kulstofatomerne på kanten af coronenmolekylet og først derefter kan sætte sig på de midterste kulstofatomer. Dette og mange andre observationer skulle gerne i fremtiden hjælpe os med at få en bedre forståelse af hele sammenspillet mellem PAH'er og brintatomer.

Bibliography

- [1] A. G. G. M. Tielens. *The Physics and Chemistry of the Interstellar Medium*. Cambridge University Press, 2005.
- [2] A. G. G. M. Tielens. The molecular universe. *Reviews of Modern Physics*, 85(3):1021–1081, 2013.
- [3] L. Hornekær, A. Baurichter, V. V. Petrunin, D. Field, and A. C. Luntz. Importance of Surface Morphology in Interstellar H₂ Formation. *Science*, 302(5652):1943–1946, 2003.
- [4] L. Hornekær, Ž. Šljivančanin, W. Xu, R. Otero, E. Rauls, I. Stensgaard, E. Lægsgaard, B. Hammer, and F. Besenbacher. Metastable Structures and Recombination Pathways for Atomic Hydrogen on the Graphite (0001) Surface. *Physical Review Letters*, 96(15):156104, 2006.
- [5] E. Habart, F. Boulanger, L. Verstraete, G. P. des Fortes, E. Falgarone, and A. Abergel. H(2) infrared line emission across the bright side of the rho Ophiuchi main cloud. *Astronomy & Astrophysics*, 397(2):623–634, 2003.
- [6] F. Boulanger, P. Boissel, D. Cesarsky, and C. Rytter. The shape of the unidentified infra-red bands: analytical fit to ISOCAM spectra. *Astronomy & Astrophysics*, 339:194–200, 1998.
- [7] G. C. Clayton, K. D. Gordon, F. Salama, L. J. Allamandola, P. G. Martin, T. P. Snow, D. C. B. Whittet, A. N. Witt, and M. J. Wolff. The Role of Polycyclic Aromatic Hydrocarbons in Ultraviolet Extinction. I. Probing Small Molecular Polycyclic Aromatic Hydrocarbons. *The Astrophysical Journal*, 592(2):947–952, 2003.
- [8] H. Richter and J. Howard. Formation of polycyclic aromatic hydrocarbons and their growth to soot - a review of chemical reaction pathways. *Progress in Energy and Combustion Science*, 26(4-6):565–608, 2000.

- [9] M. Pöhlmann, A. Hitzel, F. Schwägele, K. Speer, and W. Jira. Contents of polycyclic aromatic hydrocarbons (PAH) and phenolic substances in Frankfurter-type sausages depending on smoking conditions using glow smoke. *Meat Science*, 90(1):176–184, 2012.
- [10] C.-E. Boström, P. Gerde, A. Hanberg, B. Jernström, C. Johansson, T. Kyrklund, A. Rannug, M. Törnqvist, K. Victorin, and R. Westerholm. Cancer risk assessment, indicators, and guidelines for polycyclic aromatic hydrocarbons in the ambient air. *Environmental health perspectives*, 110:451–488, 2002.
- [11] M. P. Bernstein, S. A. Sandford, and L. J. Allamandola. Hydrogenated polycyclic aromatic hydrocarbons and the 2940 and 2850 wavenumber (3.40 and 3.51 micron) infrared emission features. *Astrophysical Journal*, 472(2):L127–L130, 1996.
- [12] S. A. Sandford, M. P. Bernstein, and C. K. Materese. The infrared spectra of polycyclic aromatic hydrocarbons with excess peripheral H atoms (Hn-PAHs) and their relation to the 3.4 and 6.9 μm PAH emission features. *The Astrophysical Journal Supplement Series*, 205(1):8, 2013.
- [13] J. A. Venables. *Introduction to Surface and Thin Film Processes*. Cambridge University Press, 2000.
- [14] B. Jørgensen. *Hydrogen interaction with carbonaceous materials*. PhD thesis, Aarhus University, 2011.
- [15] H. Lüth. *Solid Surfaces, Interfaces and Thin Films*. Springer, 2010.
- [16] R. Zacharia. *Desorption of gases from graphitic and porous carbon surfaces*. PhD thesis, Freien Universität Berlin, 2004.
- [17] A. J. Slavin. A new kinetic theory for thermal desorption of two-dimensional islands. *Journal of Vacuum Science & Technology A: Vacuum, Surfaces, and Films*, 8(3):2463, 1990.
- [18] R. Zacharia, H. Ulbricht, and T. Hertel. Interlayer cohesive energy of graphite from thermal desorption of polyaromatic hydrocarbons. *Physical Review B - Condensed Matter and Materials Physics*, 69(15):1–7, 2004.
- [19] K. J. Laidler, S. Glasstone, and H. Eyring. Application of the Theory of Absolute Reaction Rates to Heterogeneous Processes I. The Adsorption and Desorption of Gases. *Journal of Chemical Physics*, 8(1940):659–667, 1940.

- [20] J. De Boer. *Adsorption Phenomena*. Springer, 1956.
- [21] D. A. King. Thermal desorption from metal surfaces: A review. *Surface Science*, 47(1):384–402, 1975.
- [22] A. M. de Jong and J. W. Niemantsverdriet. Thermal desorption analysis: Comparative test of ten commonly applied procedures. *Surface Science*, 233(3):355–365, 1990.
- [23] P. A. Redhead. Thermal desorption of gases. *Vacuum*, 12(4):203–211, 1962.
- [24] J. L. Falconer and R. J. Madix. Desorption rate isotherms in flash desorption analysis. *Journal of Catalysis*, 48(1-3):262–268, 1977.
- [25] J. Miller, H. Siddiqui, S. Gates, J. Russell Jr, J. Yates Jr, J. Tully, and M. Cardillo. Extraction of kinetic parameters in temperature programmed desorption: A comparison of methods, 1987.
- [26] E. Habenschaden and J. Küppers. Evaluation of flash desorption spectra. *Surface Science*, 138(1):L147–L150, 1984.
- [27] K. G. Tschersich and V. von Bonin. Formation of an atomic hydrogen beam by a hot capillary. *Journal of Applied Physics*, 84(8):4065–4070, 1998.
- [28] K. G. Tschersich. Intensity of a source of atomic hydrogen based on a hot capillary. *Journal of Applied Physics*, 87(5):2565–2573, 2000.
- [29] K. G. Tschersich, J. P. Fleischhauer, and H. Schuler. Design and characterization of a thermal hydrogen atom source. *Journal of Applied Physics*, 104(3), 2008.
- [30] A. Dinger, C. Lutterloh, and J. Küppers. Kinetics of D abstraction with H atoms from the monodeuteride phase on Si(100) surfaces. *Chemical physics letters*, 311(3-4):202–208, 1999.
- [31] K. Oura, V. G. Lifshits, a. a. Saranin, a. V. Zotov, and M. Katayama. Hydrogen interaction with clean and modified silicon surfaces. *Surface Science Reports*, 35(1-2):1–69, 1999.
- [32] P. Feulner and D. Menzel. Simple ways to Improve "Flash desorption" Measurements from single crystal surfaces. *Journal of Vacuum Science and Technology*, 17(2):662–663, 1980.
- [33] G. Binnig, H. Rohrer, C. Gerber, and E. Weibel. Tunneling through a controllable vacuum gap. *Applied Physics Letters*, 40(2):178–180, 1982.

- [34] G. Binnig and H. Rohrer. Scanning Tunneling Microscopy. *Helvetica Physica Acta*, 55(6):726–735, 1982.
- [35] G. Binnig, H. Rohrer, C. Gerber, and E. Weibel. 7x7 Reconstruction on Si(111) Resolved in Real Space. *Physical Review Letters*, 50(2):120–123, 1983.
- [36] P. Hawkes and J. C. H. Spence. *Science of Microscopy*. Springer, 2008.
- [37] J. Tersoff and D. R. Hamann. Theory of the scanning tunneling microscope. *Physical Review B*, 31(2):805–813, 1985.
- [38] K. Besocke. An easily operable scanning tunneling microscope. *Surface Science*, 181(1-2):145–153, 1987.
- [39] P. Hohenberg and W. Kohn. Inhomogeneous Electron Gas. *Physical Review B*, 136(3B):B864, 1964.
- [40] W. Kohn and L. J. Sham. Self-Consistent Equations Including Exchange and Correlation Effects. *Physical Review*, 140(4A):A1133–A1138, 1965.
- [41] J. P. Perdew and Y. Wang. Accurate and simple analytic representation of the electron-gas correlation energy. *Physical Review B*, 45(23):13244–13249, 1992.
- [42] A. D. Becke. A new mixing of Hartree-Fock and local density-functional theories. *The Journal of Chemical Physics*, 98(2):1372, 1993.
- [43] J. Perdew, K. Burke, and Y. Wang. Generalized gradient approximation for the exchange-correlation hole of a many-electron system. *Physical Review B*, 54(23):16533–16539, 1996.
- [44] J. Klimes, D. R. Bowler, and A. Michaelides. Chemical accuracy for the van der Waals density functional. *Journal of Physics-Condensed Matter*, 22(2), 2010.
- [45] <http://cnx.org/contents/1mvvVMOa@2/Hybrid-Atomic-Orbitals> [accessed 26 July 2016].
- [46] F. Salama, E. L. O. Bakes, L. J. Allamandola, and A. G. G. M. Tielens. Assessment of the Polycyclic Aromatic Hydrocarbon - Diffuse Interstellar Band Proposal. *The Astrophysical Journal*, 458:621, 1996.
- [47] J. M. Robertson and J. G. White. The crystal structure of coronene: a quantitative X-ray investigation. *Journal of the Chemical Society (Resumed)*, 0:607, 1945.

- [48] J. Tabony, J. White, J. Delachaume, and M. Coulon. Nuclear magnetic resonance studies of the melting and orientation of benzene adsorbed upon graphite. *Surface Science*, 95(2-3):L282–L288, 1980.
- [49] J. D. Thrower, E. E. Friis, A. L. Skov, L. Nilsson, M. Andersen, L. Ferrighi, B. Jørgensen, S. Baouche, R. Balog, B. Hammer, and L. Hornekær. Interaction between Coronene and Graphite from Temperature-Programmed Desorption and DFT-vdW Calculations: Importance of Entropic Effects and Insights into Graphite Interlayer Binding. *The Journal of Physical Chemistry C*, 117(26):13520–13529, 2013.
- [50] U. Bardi, S. Magnanelli, and G. Rovida. LEED Study of Benzene and Naphthalene Monolayers Adsorbed on the Basal Plane of Graphite. *Langmuir*, 3(2):159–163, 1987.
- [51] I. Gameson and T. Payment. Confirmation of the $\sqrt{7} \times \sqrt{7}$ commensurate structure of a benzene monolayer adsorbed on graphite. *Chemical Physics Letters*, 123(3):150–153, 1986.
- [52] T. Yamada, Y. Takano, M. Isobe, K. Miyakubo, and T. Munakata. Growth and adsorption geometry of naphthalene overlayers on HOPG studied by low-temperature scanning tunneling microscopy. *Chemical Physics Letters*, 546:136–140, 2012.
- [53] U. Zimmermann and N. Karl. Epitaxial-Growth of Coronene and Hexa-Peri-Benzocoronene on Mos2(0001) and Graphite(0001) - a LEED Study of Molecular-Size Effects. *Surface Science*, 268(1-3):296–306, 1992.
- [54] K. Walzer, M. Sternberg, and M. Hietschold. Formation and characterization of coronene monolayers on HOPG(0001) and MoS2(0001): a combined STM/STS and tight-binding study. *Surface Science*, 415(3):376–384, 1998.
- [55] M. Lackinger, S. Griessl, W. M. Heckl, and M. Hietschold. STM and STS of coronene on HOPG(0001) in UHV - Adsorption of the smallest possible graphite flakes on graphite. *Analytical and Bioanalytical Chemistry*, 374(4):685–687, 2002.
- [56] Y. J. Dappe, M. Andersen, R. Balog, L. Hornekær, and X. Bouju. Adsorption and STM imaging of polycyclic aromatic hydrocarbons on graphene. *Physical Review B*, 91(4):045427, 2015.
- [57] M. Meissner, F. Sojka, L. Matthes, F. Bechstedt, X. Feng, K. Müllen, S. C. B. Mannsfeld, R. Forker, and T. Fritz. Flexible 2D Crystals of

- Polycyclic Aromatics Stabilized by Static Distortion Waves. *ACS Nano*, 10(7):6474–6483, 2016.
- [58] T. Huempfer, F. Sojka, R. Forker, and T. Fritz. Growth of coronene on (100)- and (111)-surfaces of fcc-crystals. *Surface Science*, 639:80–88, 2015.
- [59] M. Lackinger, S. Griessl, W. M. Heckl, and M. Hietschold. Coronene on Ag(111) investigated by LEED and STM in UHV. *Journal of Physical Chemistry B*, 106(17):4482–4485, 2002.
- [60] J. Martínez-Blanco, A. Mascaraque, Y. S. Dedkov, and K. Horn. Ge(001) As a Template for Long-Range Assembly of π -Stacked Coronene Rows. *Langmuir*, 28(8):3840–3844, 2012.
- [61] J. Martínez-Blanco, B. Walter, A. Mascaraque, and K. Horn. Long-Range Order in an Organic Overlayer Induced by Surface Reconstruction: Coronene on Ge(111). *The Journal of Physical Chemistry C*, 118(22):11699–11703, 2014.
- [62] J. Martínez-Blanco, M. Klingsporn, and K. Horn. Selective adsorption of coronene on Si(111)-(7x7). *Surface Science*, 604(5-6):523–528, 2010.
- [63] A. A. G. Pez, A. Scott, A. Cooper, H. Cheng, F. Wilhelm. Hydrogen storage by Reversible hydrogenation of pi-conjugated substrates. *United States Patent*, pages US 7,351,395 B1, 2008.
- [64] K. May, B. V. Unterreiner, S. Dapprich, and R. Ahlrichs. Structures and C-H bond energies of hydrogenated polycyclic aromatic hydrocarbons. *Physical Chemistry Chemical Physics*, 2(22):5089–5092, 2000.
- [65] E. Rauls and L. Hornekær. Catalyzed routes to molecular hydrogen formation and hydrogen addition reactions on neutral polycyclic aromatic hydrocarbons under interstellar conditions. *The Astrophysical Journal*, 679(1):531–536, 2008.
- [66] J. A. Rasmussen, G. Henkelman, and B. Hammer. Pyrene: Hydrogenation, hydrogen evolution, and π -band model. *Journal of Chemical Physics*, 134(16):1–11, 2011.
- [67] R. M. Ferullo, N. J. Castellani, and P. G. Belevi. Interaction of atomic hydrogen with anthracene and polyacene from density functional theory. *Chemical Physics Letters*, 648:25–30, 2016.
- [68] J. A. Rasmussen. Polycyclic aromatic hydrocarbons: Trends for bonding hydrogen. *Journal of Physical Chemistry A*, 117(20):4279–4285, 2013.

- [69] M. Bonfanti, S. Casolo, G. F. Tantardini, A. Ponti, and R. Martinazzo. A few simple rules governing hydrogenation of graphene dots. *The Journal of Chemical Physics*, 135(16):164701, 2011.
- [70] T. P. M. Goumans. Hydrogen chemisorption on polycyclic aromatic hydrocarbons via tunnelling. *Monthly Notices of the Royal Astronomical Society*, 415(4):3129–3134, 2011.
- [71] J. D. Thrower, B. Jørgensen, E. E. Friis, S. Baouche, V. Mennella, A. C. Luntz, M. Andersen, B. Hammer, and L. Hornekær. Experimental Evidence for the Formation of Highly Superhydrogenated Polycyclic Aromatic Hydrocarbons through H Atom Addition and Their Catalytic Role in H₂ Formation. *The Astrophysical Journal*, 752(1), 2012.
- [72] J. Thrower, L. Nilsson, B. Jørgensen, S. Baouche, R. Balog, A. Luntz, I. Stensgaard, E. Rauls, and L. Hornekær. Superhydrogenated PAHs: Catalytic formation of H₂. *EAS Publications Series*, 46:453–460, 2011.
- [73] V. Mennella. Interaction of atomic hydrogen with carbon grains. *EAS Publications Series*, 46:393–398, 2011.
- [74] V. Mennella, L. Hornekær, J. Thrower, and M. Accolla. The Catalytic Role of Coronene for Molecular Hydrogen Formation. *Astrophysical Journal Letters*, 745(1), 2012.
- [75] C. Lutterloh, J. Biener, A. Schenk, and J. Kuppers. Interaction of D(H) atoms with physisorbed benzene and (1,4)-dimethylcyclohexane: Hydrogenation and H abstraction. *Journal of Chemical Physics*, 104(6):2392–2400, 1996.
- [76] M. Xi and B. E. Bent. Evidence for an Eley-Rideal mechanism in the addition of hydrogen atoms to unsaturated hydrocarbons on Cu(111). *Journal of Vacuum Science Technology B: Microelectronics and Nanometer Structures*, 10(6):2440–2446, 1992.
- [77] M. Xi and B. E. Bent. Reaction of deuterium atoms with cyclohexane on copper (111): Hydrogen abstraction reactions by Eley-Rideal mechanisms. *The Journal of Physical Chemistry*, 97(16):4167–4172, 1993.
- [78] Y. Fu, J. Szczepanski, and N. C. Polfer. Photon-Induced Formation of Molecular Hydrogen From a Neutral Polycyclic Aromatic Hydrocarbon: 9,10-Dihydroanthracene. *The Astrophysical Journal*, 744(1):61, 2012.

- [79] N. Hiyoshi, M. Osada, C. V. Rode, O. Sato, and M. Shirai. Hydrogenation of benzothiophene-free naphthalene over charcoal-supported metal catalysts in supercritical carbon dioxide solvent. *Applied Catalysis A: General*, 331(1):1–7, 2007.
- [80] M. J. Jacinto, O. H. Santos, R. Landers, P. K. Kiyohara, and L. M. Rossi. On the catalytic hydrogenation of polycyclic aromatic hydrocarbons into less toxic compounds by a facile recoverable catalyst. *Applied Catalysis B: Environmental*, 90(3-4):688–692, 2009.
- [81] W. Liao, H. W. Liu, H. J. Chen, W. Y. Chang, K. H. Chiu, and C. M. Wai. Catalytic hydrogenation rate of polycyclic aromatic hydrocarbons in supercritical carbon dioxide containing polymer-stabilized palladium nanoparticles. *Chemosphere*, 82(4):573–580, 2011.
- [82] C. W. Bauschlicher. The Reaction of Polycyclic Aromatic Hydrocarbon Cations with Hydrogen Atoms: The Astrophysical Implications. *The Astrophysical Journal*, 509:L125–L127, 1998.
- [83] M. Hirama, T. Ishida, and J. I. Aihara. Possible molecular hydrogen formation mediated by the radical cations of anthracene and pyrene. *Journal of Computational Chemistry*, 24(12):1378–1382, 2003.
- [84] A. Ricca, E. L. O. Bakes, and C. W. Bauschlicher. The Energetics for Hydrogen Addition to Naphthalene Cations. *The Astrophysical Journal*, 659(1):858–861, 2007.
- [85] V. Le Page, Y. Keheyan, V. M. Bierbaum, and T. P. Snow. Chemical Constraints on Organic Cations in the Interstellar Medium. *Journal of the American Chemical Society*, 119(35):8373–8374, 1997.
- [86] T. P. Snow, V. Le Page, Y. Keheyan, and V. M. Bierbaum. The interstellar chemistry of PAH cations. *Nature*, 391(6664):259–260, 1998.
- [87] B. Klærke, Y. Toker, D. B. Rahbek, L. Hornekær, and L. H. Andersen. Formation and stability of hydrogenated PAHs in the gas phase. *Astronomy & Astrophysics*, 84:1–9, 2012.
- [88] L. Boschman, G. Reitsma, S. Cazaux, T. Schlatholter, R. Hoekstra, M. Spaans, and O. Gonzalez-Magana. Hydrogenation of Pah Cations: A First Step toward H₂ Formation. *Astrophysical Journal Letters*, 761(2):L33, 2012.

- [89] S. Cazaux, L. Boschman, N. Rougeau, G. Reitsma, R. Hoekstra, D. Teillet-Billy, S. Morisset, M. Spaans, and T. Schlathölter. The sequence to hydrogenate coronene cations: A journey guided by magic numbers. *Scientific Reports*, 6:19835, 2016.
- [90] M. Vala, J. Szczepanski, J. Oomens, and J. D. Steill. H₂ Ejection from Polycyclic Aromatic Hydrocarbons: Infrared Multiphoton Dissociation Study of Protonated 1,2-Dihydronaphthalene. *Journal of the American Chemical Society*, 131(16):5784–5791, 2009.
- [91] J. Szczepanski, J. Oomens, J. D. Steill, and M. T. Vala. H₂ ejection from polycyclic aromatic hydrocarbons: Infrared multiphoton dissociation study of protonated acenaphthene and 9,10-dihydrophenanthrene. *The Astrophysical Journal*, 727(1):12, 2011.
- [92] J. Zhen, S. R. Castillo, C. Joblin, G. Mulas, H. Sabbah, A. Giuliani, L. Nahon, S. Martin, J.-P. Champeaux, and P. M. Mayer. VUV Photo-Processing of PAH Cations: Quantitative Study on the Ionization Versus Fragmentation Processes. *The Astrophysical Journal*, 822(2):113, 2016.
- [93] J. Zhen, P. Castellanos, D. M. Paardekooper, N. Ligterink, H. Linnartz, L. Nahon, C. Joblin, and A. G. G. M. Tielens. Laboratory photo-chemistry of PAHs: Ionization versus fragmentation. *The Astrophysical Journal*, 804(1):L7, 2015.
- [94] M. Gatchell, M. H. Stockett, N. De Ruelle, T. Chen, L. Giacomozzi, R. F. Nascimento, M. Wolf, E. K. Anderson, R. Delaunay, V. Vizcaino, P. Rousseau, L. Adoui, B. A. Huber, H. T. Schmidt, H. Zettergren, and H. Cederquist. Failure of hydrogenation in protecting polycyclic aromatic hydrocarbons from fragmentation. *Physical Review A - Atomic, Molecular, and Optical Physics*, 92(5):4–8, 2015.
- [95] T. Chen, M. Gatchell, M. H. Stockett, R. Delaunay, A. Domaracka, E. R. Micelotta, A. G. G. M. Tielens, P. Rousseau, L. Adoui, B. A. Huber, H. T. Schmidt, H. Cederquist, and H. Zettergren. Formation of H₂ from internally heated polycyclic aromatic hydrocarbons: Excitation energy dependence. *Journal of Chemical Physics*, 142(14):1–8, 2015.
- [96] M. Wolf, L. Giacomozzi, M. Gatchell, N. De Ruelle, M. H. Stockett, H. T. Schmidt, H. Cederquist, and H. Zettergren. Hydrogenated pyrene: Statistical single-carbon loss below the knockout threshold. *European Physical Journal D*, 70(4), 2016.

- [97] K. M. Ferrière. The interstellar environment of our galaxy. *Reviews of Modern Physics*, 73(4):1031–1066, 2001.
- [98] M. J. Abplanalp, M. Förstel, and R. I. Kaiser. Exploiting single photon vacuum ultraviolet photoionization to unravel the synthesis of complex organic molecules in interstellar ices. *Chemical Physics Letters*, 644:79–98, 2016.
- [99] A. Tielens. Interstellar Polycyclic Aromatic Hydrocarbon Molecules*. *Annual Review of Astronomy and Astrophysics*, 46(1):289–337, 2008.
- [100] <http://imagine.gsfc.nasa.gov/science/objects/stars1.html> [accessed 26 July 2016].
- [101] J. M. Dickey and R. W. Garwood. The mass spectrum of interstellar clouds. *The Astrophysical Journal*, 341(1, 1):201–207, 1989.
- [102] E. A. Bergin and M. Tafalla. Cold Dark Clouds: The Initial Conditions for Star Formation. *Annual Review of Astronomy and Astrophysics*, 45(1):339–396, 2007.
- [103] T. P. Snow and A. N. Witt. Interstellar Depletions Updated: Where All the Atoms Went. *The Astrophysical Journal*, 468(1):L65–L68, 1996.
- [104] E. L. Gibb, D. C. B. Whittet, W. a. Schutte, a. C. a. Boogert, J. E. Chiar, P. Ehrenfreund, P. a. Gerakines, J. V. Keane, a. G. G. M. Tielens, E. F. van Dishoeck, and O. Kerkhof. An Inventory of Interstellar Ices toward the Embedded Protostar W33A. *The Astrophysical Journal*, 536(1):347–356, 2000.
- [105] A. Leger and J. L. Puget. Identification of the Unidentified Ir Emission Features of Interstellar Dust. *Astronomy and Astrophysics*, 137(1):L5–L8, 1984.
- [106] L. J. Allamandola, A. G. G. M. Tielens, and J. R. Barker. Polycyclic Aromatic-Hydrocarbons and the Unidentified Infrared-Emission Bands - Auto Exhaust Along the Milky-Way. *The Astrophysical Journal*, 290(1):L25–L28, 1985.
- [107] L. J. Allamandola, A. G. G. M. Tielens, and J. R. Barker. Interstellar polycyclic aromatic hydrocarbons - The infrared emission bands, the excitation/emission mechanism, and the astrophysical implications. *The Astrophysical Journal Supplement Series*, 71(4):733, 1989.

- [108] E. Peeters, S. Hony, C. Van Kerckhoven, A. G. G. M. Tielens, L. J. Allamandola, D. M. Hudgins, and C. W. Bauschlicher. The rich 6 to 9 μm spectrum of interstellar PAHs. *Astronomy & Astrophysics*, 390(3):1089–1113, 2002.
- [109] J. Szczepanski and M. Vala. Infrared frequencies and intensities for astrophysically important polycyclic aromatic hydrocarbon cations. *The Astrophysical Journal*, 414:646, 1993.
- [110] C. Moutou, A. Leger, and L. D’Hendecourt. Far-infrared emission of PAH molecules (14–40 μm): a preparation for ISO spectroscopy. *Astronomy and Astrophysics*, 310:297–308, 1996.
- [111] H.-S. Kim and R. J. Saykally. Single Photon Infrared Emission Spectroscopy of Gaseous Polycyclic Aromatic Hydrocarbon Cations: A Direct Test for Proposed Carriers of the Unidentified Infrared Emission Bands. *The Astrophysical Journal Supplement Series*, 143(2):455–467, 2002.
- [112] S. R. Langhoff. Theoretical Infrared Spectra for Polycyclic Aromatic Hydrocarbon Neutrals, Cations, and Anions. *The Journal of Physical Chemistry*, 100(8):2819–2841, 1996.
- [113] C. W. Bauschlicher. The Infrared Spectra of C₉₆H₂₄, C₉₆H₂₄⁺ and C₉₆H₂₅⁺. *The Astrophysical Journal*, 564(2):782–786, 2002.
- [114] D. M. Hudgins and L. J. Allamandola. The Spacing of the Interstellar 6.2 and 7.7 Micron Emission Features as an Indicator of Polycyclic Aromatic Hydrocarbon Size. *The Astrophysical Journal*, 513(1):L69–L73, 1999.
- [115] D. M. Hudgins and L. J. Allamandola. Interstellar PAH Emission in the 11–14 Micron Region: New Insights from Laboratory Data and a Tracer of Ionized PAHs. *The Astrophysical Journal*, 516(1):L41–L44, 1999.
- [116] M. Rapacioli, C. Joblin, and P. Boissel. Spectroscopy of polycyclic aromatic hydrocarbons and very small grains in photodissociation regions. *Astronomy and Astrophysics*, 429(1):193–204, 2005.
- [117] M. Rapacioli, F. Calvo, C. Joblin, P. Parneix, D. Toubblanc, and F. Spiegelman. Formation and destruction of polycyclic aromatic hydrocarbon clusters in the interstellar medium. *Astronomy and Astrophysics*, 460(2):519–531, 2006.
- [118] I. Cherchneff. The formation of polycyclic aromatic hydrocarbons in evolved circumstellar environments. *EAS Publications Series*, 46:13, 2010.

- [119] J. A. Miller and C. F. Melius. Kinetic and thermodynamic issues in the formation of aromatic compounds in flames of aliphatic fuels. *Combustion and Flame*, 91(1):21–39, 1992.
- [120] M. Frenklach and E. D. Feigelson. Formation of polycyclic aromatic hydrocarbons in circumstellar envelopes. *The Astrophysical Journal*, 341:372, 1989.
- [121] J. A. Cole, J. D. Bittner, J. P. Longwell, and J. B. Howard. Formation mechanisms of aromatic compounds in aliphatic flames. *Combustion and Flame*, 56(1):51–70, 1984.
- [122] D. S. N. Parker, F. Zhang, Y. S. Kim, R. I. Kaiser, A. Landera, V. V. Kislov, A. M. Mebel, and A. G. G. M. Tielens. Low temperature formation of naphthalene and its role in the synthesis of PAHs (Polycyclic Aromatic Hydrocarbons) in the interstellar medium. *Proceedings of the National Academy of Sciences*, 109(1):53–58, 2012.
- [123] T. Q. Zhao, Q. Li, B. S. Liu, R. K. E. Gover, P. J. Sarre, and A. S.-C. Cheung. Laboratory astrochemistry: catalytic conversion of acetylene to polycyclic aromatic hydrocarbons over SiC grains. *Physical Chemistry Chemical Physics*, 18(5):3489–3496, 2016.
- [124] A. P. Jones, A. G. G. M. Tielens, and D. J. Hollenbach. Grain Shattering in Shocks: The Interstellar Grain Size Distribution. *The Astrophysical Journal*, 469:740, 1996.
- [125] C. Gall, J. Hjorth, D. Watson, E. Dwek, J. R. Maund, O. Fox, G. Leloudas, D. Malesani, and A. C. Day-Jones. Rapid formation of large dust grains in the luminous supernova 2010jl. *Nature*, 511(7509):326–329, 2014.
- [126] P. Merino, M. Švec, J. Martinez, P. Jelinek, P. Lacovig, M. Dalmiglio, S. Lizzit, P. Soukiassian, J. Cernicharo, and J. Martin-Gago. Graphene etching on SiC grains as a path to interstellar polycyclic aromatic hydrocarbons formation. *Nature Communications*, 5:1–9, 2014.
- [127] V. Pirronello, O. Biham, C. Liu, L. Shen, and G. Vidali. Efficiency of Molecular Hydrogen Formation on Silicates. *The Astrophysical Journal*, 483(2):L131–L134, 1997.
- [128] V. Pirronello, C. Liu, L. Shen, and G. Vidali. Laboratory Synthesis of Molecular Hydrogen on Surfaces of Astrophysical Interest. *The Astrophysical Journal*, 475(1):L69–L72, 1997.

- [129] H. B. Perets, A. Lederhendler, O. Biham, G. Vidali, L. Li, S. Swords, E. Congiu, J. Roser, G. Manicó, J. R. Brucato, and V. Pirronello. Molecular Hydrogen Formation on Amorphous Silicates under Interstellar Conditions. *The Astrophysical Journal*, 661(2):L163–L166, 2007.
- [130] G. Vidali, L. Li, J. E. Roser, and R. Badman. Catalytic activity of interstellar grains: Formation of molecular hydrogen on amorphous silicates. *Advances in Space Research*, 43(8):1291–1298, 2009.
- [131] E. R. Latimer, F. Islam, and S. D. Price. Studies of HD formed in excited vibrational states from atomic recombination on cold graphite surfaces. *Chemical Physics Letters*, 455(4-6):174–177, 2008.
- [132] J. Perry and S. Price. Detection of rovibrationally excited H₂ formed through the heterogeneous recombination of H atoms on a cold HOPG surface. *Astrophysics and Space Science*, 285(3/4):769–776, 2003.
- [133] V. Pirronello, C. Liu, J. E. Roser, and G. Vidali. Measurements of molecular hydrogen formation on carbonaceous grains. *Astronomy and Astrophysics*, 344(2):681–686, 1999.
- [134] L. Hornekær, A. Baurichter, V. V. Petrunin, A. C. Luntz, B. D. Kay, and A. Al-Halabi. Influence of surface morphology on D₂ desorption kinetics from amorphous solid water. *Journal of Chemical Physics*, 122(12):1–12, 2005.
- [135] G. Manicò, G. Ragnì, V. Pirronello, J. E. Roser, and G. Vidali. Laboratory Measurements of Molecular Hydrogen Formation on Amorphous Water Ice. *The Astrophysical Journal*, 548(2):L253–L256, 2001.
- [136] H. M. Cuppen and E. Herbst. Monte Carlo simulations of H₂ formation on grains of varying surface roughness. *Monthly Notices of the Royal Astronomical Society*, 361(2):565–576, 2005.
- [137] T. Zecho, A. Güttler, X. Sha, B. Jackson, and J. Kuppers. Adsorption of hydrogen and deuterium atoms on the (0001) graphite surface. *The Journal of Chemical Physics*, 117(18):8486, 2002.
- [138] X. Sha and B. Jackson. First-principles study of the structural and energetic properties of H atoms on a graphite (0001) surface. *Surface Science*, 496(3):318–330, 2002.
- [139] E. Habart, F. Boulanger, L. Verstraete, C. M. Walmsley, and G. P. des Forets. Some empirical estimates of the H(2) formation rate in photon-dominated regions. *Astronomy & Astrophysics*, 414(2):531–544, 2004.

- [140] H. Andrews, A. Candian, and A. G. G. M. Tielens. Hydrogenation and dehydrogenation of interstellar PAHs: Spectral characteristics and H₂ formation. *Astronomy & Astrophysics*, Forthcoming, 2016.
- [141] A. L. Skov, J. D. Thrower, and L. Hornekær. Polycyclic aromatic hydrocarbons - catalysts for molecular hydrogen formation. *Faraday Discussions*, 168:223, 2014.
- [142] J. D. Thrower, E. E. Friis, A. L. Skov, B. Jørgensen, and L. Hornekær. Hydrogenation of PAH molecules through interaction with hydrogenated carbonaceous grains. *Physical Chemistry Chemical Physics*, 16(8):3381–3387, 2014.
- [143] C. T. Campbell and J. R. V. Sellers. Correction to "The Entropies of Adsorbed Molecules". *Journal of the American Chemical Society*, 135(37):13998–13998, 2013.
- [144] R. A. Alberty, M. B. Chung, and A. K. Reif. Standard Chemical Thermodynamic Properties of Polycyclic Aromatic Hydrocarbons and Their Isomer Groups. II. Pyrene Series, Naphthopyrene Series, and Coronene Series. *Journal of Physical and Chemical Reference Data*, 18(1):77–109, 1989.
- [145] V. Oja and E. Suuberg. Vapor pressures and enthalpies of sublimation of polycyclic aromatic hydrocarbons and their derivatives. *Journal of Chemical & Engineering Data*, 9568(97):486–492, 1998.
- [146] H. M. Cuppen and L. Hornekær. Kinetic Monte Carlo studies of hydrogen abstraction from graphite. *The Journal of chemical physics*, 128(17):174707, 2008.
- [147] P. Sautet and C. Joachim. Electronic transmission coefficient for the single-impurity problem in the scattering-matrix approach. *Physical Review B*, 38(17):12238–12247, 1988.
- [148] P. Sautet and C. Joachim. Calculation of the benzene on rhodium STM images. *Chemical Physics Letters*, 185(1-2):23–30, 1991.
- [149] F. Besenbacher, E. Laegsgaard, K. Mortensen, U. Nielsen, and I. Stensgaard. Compact, high-stability, "thimble-size" scanning tunneling microscope. *Review of Scientific Instruments*, 59(7):1035–1038, 1988.
- [150] D. D. L. Chung. Review: Graphite. *Journal of Materials Science*, 37(8):1475–1489, 2002.

- [151] L. Gross, F. Mohn, N. Moll, P. Liljeroth, and G. Meyer. The Chemical Structure of a Molecule Resolved by Atomic Force Microscopy. *Science*, 325(5944):1110–1114, 2009.
- [152] R. Larciprete, P. Lacovig, S. Gardonio, A. Baraldi, and S. Lizzit. Atomic Oxygen on Graphite: Chemical Characterization and Thermal Reduction. *The Journal of Physical Chemistry C*, 116(18):9900–9908, 2012.